Constrained 4D Elastic Seismic Inversion: Assessing Workflows Efficiency on Real Data

João Nunes Jorge

Thesis to obtain the Master of Science Degree in

Petroleum Engineering

Supervisors

Prof. Dr. Leonardo Azevedo Guerra Raposo Pereira

Dr. Pierre Thore

Examination Committee

Chairperson: Profª. Dr. Maria João Correia Colunas Pereira

Supervisor: Dr. Pierre Thore

Member of the Committee: Dr. Hugo Manuel Vieira Caetano

December 2020

This page was intentionally left blank.

Acknowledgements

First, I want to express my thankfulness to my supervisors: Dr. Pierre Thore that provided me with the opportunity to do an internship at Total and integrated me in his team for six months, my gratitude for his support, trust and insightful discussions on challenging topics that made this thesis possible. To Professor Leonardo Azevedo for the suggestions and scientific revision of this thesis but also for all the motivation during the master’s in petroleum engineering and EVOLVE 2019 program that allowed me to expand my knowledge in different geoscience domains.

Many thanks to Antoine, Nicolas, João and Matheus for the real team building, encouragement and companionship during my stay in France. A special thanks to my colleagues during the first year of the master’s program that made me feel welcome.

I would like to acknowledge my friends who for the motivation, life lessons and positivity that also contributed for this accomplishment. My big thanks to Fred, Rafa, Diogo, David, Ana, Tiago, Raquel, Luís, Pedro, Bárbara, João and many other I shared memorable moments with.

Last but not least, my deepest gratitude goes to my family for the comprehension and all the guidance and support that made who I am today. My humble thank to everyone who was part of this journey and inspired me.

Abstract

Time-lapse seismic monitoring is nowadays a reliable tool to monitor fluid movements and to distinguish between drained and undrained portions of a reservoir. Using time-lapse seismic to monitor the changes in reservoir elastic properties can provide spatially resolved changes inside the reservoir, these changes become useful to improve the validity of fluid-flow models and consequently allow for better decision making and risk management. Its ultimate goal is to quantitatively improve reservoir models, particularly their predictive capability though time-lapse derived maps of the relative changes in reservoir elastic properties. These time-lapse elastic properties can be obtained through several 4D inversion techniques. The present work intends to experiment three different workflows to conduct elastic 4D seismic inversion as well as introducing geological information as an elegant constraint in the stochastic inversion process. The first workflow is a classical inversion of the realigned differences, the second is the independent elastic inversion and subsequent differentiation of baseline and monitor elastic parameters and the third is the inversion of the monitor vintage to provide the initial model for the inversion of the base, the resulting models are subtracted to obtain the respective 4D elastic models. The comparison between each workflow demonstrates the key parameters in which the quality of results relies the most as well as the inherent issues related to each methodology, proving an opportunity to improve when all the effecting impacting parameters are properly analyzed and managed. Nonetheless the assessment of the results inherent to each different workflow represents a powerful tool to obtain as much as possible information for 4D seismic data.

Key-words: Time-lapse Seismic, Stochastic Elastic Seismic Inversion, Reservoir Monitoring

Resumo

A informação sísmica 4D é utilizada hoje em dia na indústria como uma ferramenta fundamental para monitorizar o movimento de fluidos dentro do reservatório e para fazer a distinção entre regiões do reservatório drenadas e não drenadas. A utilização destes mesmos dados de sísmica 4D para monitorizar as propriedades elásticas do reservatório em produção fornece informação com uma resolução espacial considerável acerca de mudanças nas propriedades elásticas do reservatório. A caracterização dessas mudanças torna-se útil para melhorar a validade dos modelos dinâmicos e, consequentemente, permitir uma melhor gestão do reservatório. O objectivo final tem em conta melhorar quantitativamente os modelos do reservatório, particularmente a sua capacidade preditiva através de mapas derivados de atributos sísmicos 4D que podem ser obtidos por meio de varias técnicas de inversão sísmica 4D. O presente trabalho pretende experimentar e avaliar diferentes metodologias gerais para inversão elástica 4D, bem como introduzir informação geológica como uma restrição para guiar os processos de inversão estocástica a resultados compatível com os modelos petrofísica. Esta tese avalia três metodologias diferentes: uma inversão clássica das diferenças entre volumes de sísmica alinhados em tempo, a inversão independente de cada volume de sismica e subsequente diferenciação entre os modelos elásticos obtidos e por fim uma terceira metodologia que utiliza os modelos elásticos obtidos através da inversão independente do volume de sísmica mais recente como modelo inicial na inversão do volume de sísmica pré-produção, criando uma dependência entre os modelos resultantes. A comparação entre cada metodologia destaca os parâmetros mais importantes nos quais a qualidade dos modelos elásticos 4D dependem, bel como as problemáticas inerentes a cada uma das metodologias, constituindo uma oportunidade para a optimização quando todos os parâmetros importantes são propriamente analisados e geridos. No entanto, a avaliação dos diferentes resultados obtidos através de cada metodóloga representa uma ferramenta que permite maximizar a qualidade da informação obtida através de dados sísmicos 4D.

Palavras-chave: Sísmica 4D, Inversão Estocástica Elástica, Monitorização de Reservatórios

Declaration

I declare that this document is an original work of my own authorship and that it fulfills all the requirements of the Code of Conduct and Good Practices of the Universidade de Lisboa.

Table of contents

List of Figures

Chapters I - Introduction

Chapters II – Theoretical Concepts

Chapters III - Methodology

Chapters IV – Case Study: Results and Discussion

List of Acronyms and Symbols

μ: Shear Moduli

AVO: Amplitude Variation with Offset

HG: Hybrid Grid:

HSW: Hashin-Shtrikman Walpole Bounds
K: Bulk Moduli

LFM: Low Frequency Model

ms: Milliseconds

NCC: Normalized Correlation Coefficient

NRMS: Normalized Root Mean Square

PEM: Petroelastic Model

QC: Quality Control

RC: Reflection Coefficient

RMS: Root Mean Square

SGS: Sequential Gaussian Simulation

TWT: Two Way Travel Time

Vp: P-wave Propagation Velocity

Vs: S-wave Propagation Velocity

ρ: Density

ΔVp: Change in P-wave Propagation Velocity

ΔVs: Change in S-wave Propagation Velocity

Δρ: Change in Density

1. Introduction

1.1. Motivation

During recent years, time-lapse studies have proven that seismic monitoring is a crucial reservoir management tool. The information obtained through time-lapse seismic data (Figure 1.1), when properly combined with geology, petrophysics, and engineering disciplines, can be a valuable contribution to field development. One important use of 4D seismic is in the reservoir simulation model updating process. These models are built with static information derived from well-logs, 3D seismic data, and other information available. However, the dynamic information that is retrieved from production well data and 4D seismic provide a sophisticated way to validate and update these models during the field life cycle.

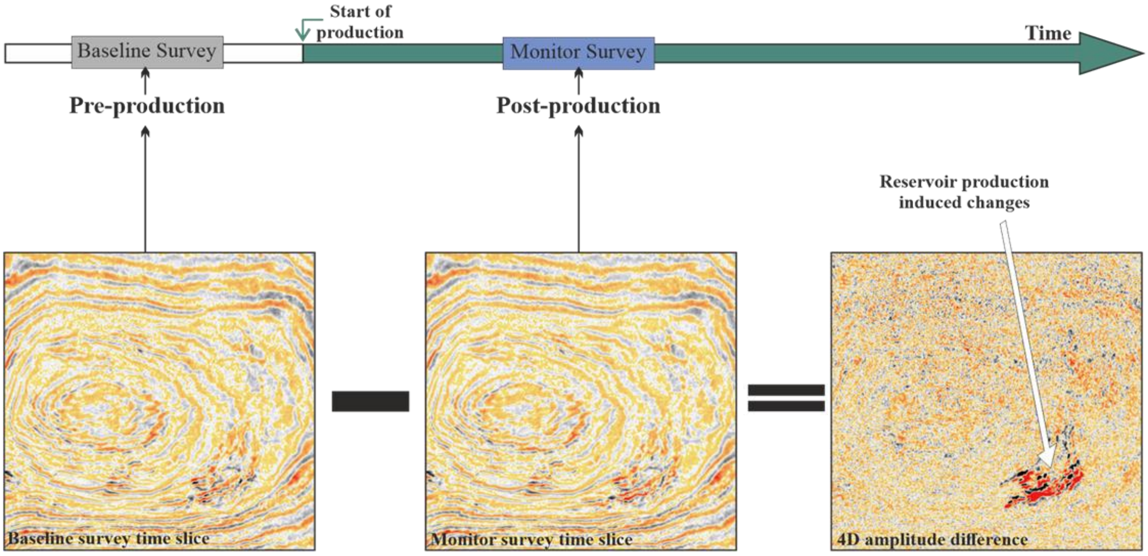

Figure 1.1 - The differences between a seismic survey acquired before production, and a monitor survey acquired after production; revealing changes is reservoir resulting from production. Providing information about the changes occurring in the inter-well regions.

Reservoir elasticity is affected by different factors including lithology, fluid content and changes in pore pressure. Conventionally, seismic inversion has been used to estimate static reservoir model properties such as porosity and lithology. Recently with the development of time-lapse seismic technology, seismic reflection data can be inverted for dynamic reservoir properties in seismic reservoir characterization workflows (Johnston 2013).

The integration of 4D seismic and reservoir simulation data has been primarily developed in a qualitative sense (Hatchell *et al*. 2002; Pannett *et al*. 2004), through simple visualization of the seismic signature compared to changes associated to production in the reservoir. Nonetheless, the progression from qualitative to quantitative interpretation methods is a crucial point that shall be established in order to increase the long-term value of time-lapse seismic data (Johnston 2013).

Production induced changes in the reservoir cause changes in reservoir parameters such as fluid saturation, pore pressure, temperature and in some cases layer thickness. These changes have a direct effect in seismic reservoir properties, such as P-and S-wave velocities, wave travel time and reflection amplitudes. Through comparison between differences in measurements of seismic properties and the understanding of the principles of rock physics, the changes in the elasticity of the subsurface can be monitored over space and time.

Using time-lapse seismic to monitor the elastic changes in reservoir properties can provide spatially resolved dynamic changes inside the reservoir, these changes become useful to improve the validity of fluid-flow models and consequently allow for better decision making and risk management. These time-lapse elastic properties can be obtained through several 4D inversion techniques (Sarkar *et al*. 2003). The purpose of this study is to assess three different workflows that ultimately deliver reliable information capitalizing on petroelastic model (PEM) constraints that ensure compatibility with prior geological and dynamical information.

1.2. Objectives

The present work intends to compare and evaluate different 4D seismic inversion procedures implemented to estimate time-lapse changes in elastic properties as well as to evaluate the impact of adding prior petrophysical knowledge through a petroelastic model that is implemented as a constraint in the seismic inversion. The study assesses three different workflows (Figure 1.2): a classical inversion of the realigned amplitude differences (workflow 1), the independent elastic inversion and subsequent differentiation of baseline and monitor elastic models (workflow 2) and the inversion of the monitor dataset to provide the initial model for the inversion of the baseline, the resulting models are subtracted to obtain the respective 4D elastic models (workflow 3).

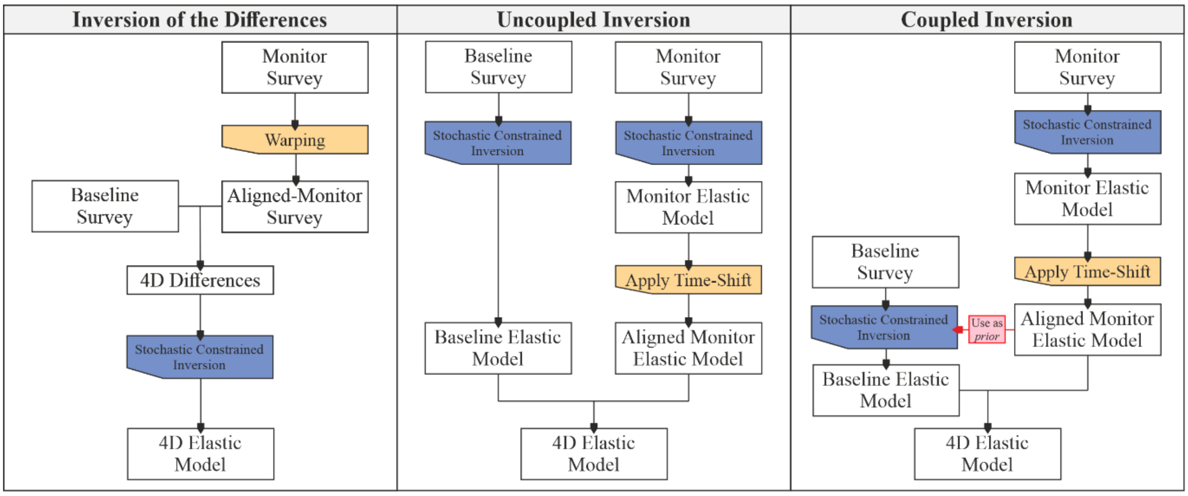

Figure 1.2 - Schematic representation of the three 4D inversion workflows assessed.

The comparison between each workflow demonstrates the key parameters in which the quality of results relies the most as well as the inherent issues related to each methodology, proving an opportunity to improve when all the effecting impacting parameters are properly analyzed and managed. Nonetheless the assessment of the results inherent to each different workflow represents a powerful tool to extract as much as information as possible from 4D seismic data.

1.3. Thesis Structure

This thesis is organized in five chapters, starting with and introduction to the problem, the scope of the project and the objectives set during the study.

Chapter II introduces the theoretical concepts behind the framework implement in this study, this chapter is divided in three parts covering the principal of seismic inversion theory, the concept of time-lapse seismic studies and the fundamental rock physics models used in reservoir characterization.

Chapter III outlines the methodology key steps that are fundamental for each workflow by describing the concepts behind each of the in-house tool used as part of this case study and separately describes each 4D inversion workflow step-by-step.

Chapter IV describes and discusses the results obtained through each step for each of the 4D inversion technique, highlighting crucial choices in parameterization and the impact on the resulting models, detailing the effect of implementing 3D and 4D PEM constraints in the stochastic inversions, emphasizing the advantages and drawbacks associated with each workflow and finishes with a detailed comparison between 4D elastic models obtained integrating them with the reservoir production mechanism in place.

The last chapter details the final considerations resulting from the work developed underlining the valuable information provided by the elastic 4D inversion, as well as some suggestions for future work based on the methodologies assessed during this project.

Part of the work presented in this thesis is also presented in the following publication (in Annex):

- Jorge, J., Thore, P., Lino, J and Lucas, A. (2020). Constrained 4D Elastic Inversion, Assessing Workflows Efficiency on Real Data. Extended Abstract presented at the 1st EAGE Conference on Seismic Inversion, Online Event, 26 – 29 October 2020.

2. Theoretical Concepts

2.1. Seismic Inverse Problem

Seismic reflection data represents an indirect measurement of the subsurface properties that provides a broad horizontal coverage along the entire reservoir extent. Conversely, well data represents a direct measurement of a range of subsurface properties providing a high vertical resolution, however, spatially sparse. The integration of these two types of data closes the loop, providing valuable insight into the reservoir petroelastic properties spatially conditioned by the seismic data and locally conditioned by the well data, representing a fundamental stage in reservoir characterization and monitoring (Doyen, 2007; Azevedo and Soares, 2017).

One of the inverse problems in geophysics is the seismic inverse problem, which has as objective the inference of the subsurface elastic properties. The observed data (d_{obs}) commonly associated with measurement errors (e) originating from different sources is the result of a set of model parameters (m). The observed data and the subsurface properties of interest are connected by a forward model (F). The relation between the observed data and the subsurface models is synthesized in Tarantola (2005) as the following (Equation 2.1):

$$d_{obs} = F(m) + e \qquad \text{(Equation 2.1)}$$

Regarding seismic reflection data, d_{obs} corresponds to the measured seismic data and F is commonly defined as the convolutional model. The spatial parameter m represents a set of N unknown subsurface model parameters that equally fit the observed seismic data. The convolutional model can be defined with the following (Equation 2.2):

$$A = RC * w \qquad \text{(Equation 2.2)}$$

where A corresponds to the observed seismic amplitudes that depend on the subsurface elastic properties (P- and S-wave velocity and density), RC corresponds to the subsurface reflection coefficient that is convoluted with a representative wavelet (w).

Seismic inversion is a technique used for creating subsurface models from recorded seismic data and can be considered as the opposite of the forward modeling (Russell, 1988) which involves creating a synthetic seismic section based on a model of the Earth (Figure 2.1). For both procedures, the use of wavelets is necessary, since they link the seismic data and the subsurface geology.

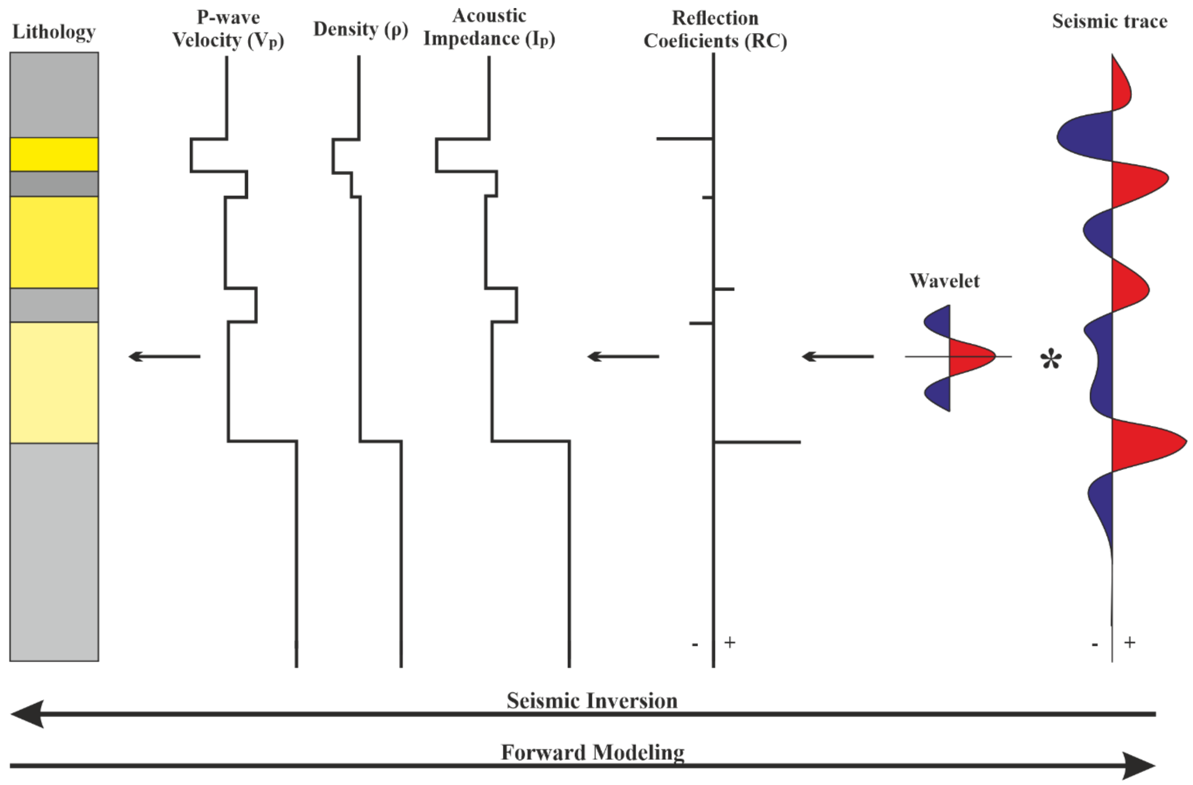

Figure 2.1 - Inverse and forward modelling schemes, showing the interdependence between difference types of data. Adapted from Simm and Bacon (2014).

Seismic inverse problems are non-linear, non-unique and ill-conditioned (Tarantola, 2005) due to limitations in the geophysical method such as measurement errors, limited bandwidth and resolution of the seismic reflection data and uncertainty in the model and observations. Consequently, there is not only one best inverse model solution that fit equally the observed data. In order to interpret the solutions to the seismic inverse problem, it is necessary to comprehend the assumptions posed behind each methodology used to solve the seismic inverse problem. These methods impact the exploration of the parameter space and assessment of the uncertainty (Azevedo *et al*. 2014).

Seismic inversion can be divided into two main types: deterministic inversion and stochastic inversion (Bosch *et al*. 2010). Deterministic inversion techniques are commonly used in the industry. Deterministic methodologies rely on regression models of optimization algorithms to minimize the error between synthetic traces resultant from the estimated impedance profile and the seismic amplitude at each trace location, resulting in a single best-estimate model (Francis 2006; Azevedo 2018). Consequently, these methodologies lack a reliable assessment of the uncertainty associated with the recovered subsurface model. According to Tarantola (2005), this inversion framework allows the assessment of the uncertainty only via a least square function, and therefore the uncertainty is solely represented by a local multivariate Gaussian. The subsurface models retrieved in this framework are a smooth representation of the subsurface properties with less spatial variability (Filippova *et al*. 2011). These techniques aim to iteratively improve a specific model by maximizing a probability density function while at the same time minimizing the difference between the improved model and the real model. At each iteration, the model is perturbated until a difference close to zero is obtained. Hampson and Russel (1991) divided the deterministic inversion in three categories: band-limited inversion, sparse spike inversion, and model-based inversion.

Briefly, band-limited inversion was the first type of post-stack inversion developed (Lindseth, 1979). In this inversion category, the result has the same frequency band as the seismic data, losing the low and high frequencies provided by the well-log data. The reflectivity trace is computed by deconvolving the seismic trace with the wavelet. This technique is based on the assumption that seismic traces represent an approximation to the subsurface reflectivity therefore it is feasible to invert to obtain an impedance trace.

Sparse-spike inversion estimates a set of sparse reflection coefficients from the seismic data and constrains them with an initial model to produce an impedance profile resulting of the inversion of these coefficients (Gavotti, 2014) considering also the missing low frequencies from well-log data or seismic velocities.

In model-based inversion techniques, the starting point is an initial subsurface model which is iteratively perturbated to minimize the error between the synthetic derived from the model in order to best fit the original seismic data. The initial model should be based on prior geological knowledge (Simm and Bacon, 2014).

As described in Gavotti (2014), this inversion method uses a generalized linear inversion algorithm, which assumes that the seismic trace (T) and the wavelet (W) are known, and the noise is random and uncorrelated with the signal. The initial model is iteratively modified until a close match between the synthetic data and the real seismic data is obtained. The solution is obtained by minimizing Equation 2.3:

$$J = weight_1(T - W * RC) + weight_2(M - H * RC) \qquad \text{(Equation 2.3)}$$

Where, RC is the final reflectivity, M is the initial impedance model, and H is the integration operator, which convolves the final reflectivity (RC) to produce the resulting impedance model. The first term of the equation models the seismic trace and the second term forces a solution that models the initial impedance model. The weights 1 and 2 are going to determine the contribution of the seismic data and the initial model for the inverse solution.

Hampson and Russell (1991) suggest that the band-limited approach is the most robust but tends to produce a smooth, frequency limited estimate of the impedances and fails when a very “sparse” model is used. The results obtained with sparse-spike and model-based methods are similar. Sparse-spike approach produces better results for a complete "sparse" model; however, has a lower resolution than model-based inversion when applied to real data. Model-based inversion techniques appear to be the most intuitively appealing within a deterministic framework but require the implementation of constraints to minimize the problem of non-uniqueness.

Unlike the deterministic methods, the stochastic methods retrieved a series of equally probable inverse models allowing for a detailed assessment of the uncertainty associated with the resulting petroelastic inverted models. The statistical approach defines the inverse solution as a probability density function on the model parameter space (Bosch *et al*. 2010). This distribution represents the uncertainty related to the experimental data and the physical process that is being modeled (Tarantola, 2005).

Briefly, one can describe stochastic seismic inversion methods as the generation of multiple realizations of the subsurface elastic properties, with the ultimate purpose of assessing the uncertainty associated to each of these properties. The importance of these inversion techniques has increased its importance in the oil and gas industry in the last past decades since it the assessment of the uncertainty in reservoir models ultimately leads to better and more reliable decisions.

There are two main categories within the geostatistical seismic inversion framework are: trace-by-trace methodologies introduced by Bortoli *et al*. (1992) and Haas and Dubrule (1994) and global inversion methodologies (Soares *et al*. 2007).

Trace-by-trace inversion techniques require that each seismic trace location is individually visited following a previously defined random path that goes through all the possible locations within the seismic survey. At each location, taking into consideration the existing well-log data and the previously visited trace locations, an ensemble of N, realizations of acoustic impedance are computed at each specific location, using a stochastic sequential simulation algorithm. By computing the reflection coefficients for one trace and convolving them with a known wavelet, it is possible to generate a synthetic seismic trace at each location, which is posteriorly compared with the real seismic trace in order to measure the correlation coefficients and residuals between real and synthetic seismic. If the correlation coefficient is above a defined threshold, the trace is considered as conditioning data for the next simulation at the next location along the random path (Haas and Dubrule 1991; Bortoli *et al*. 1992). The inversion finishes when all the trace locations defined in the random path are visited. The order in which each trace is visited is different for each realization; therefore, each run has a different set of conditioning data, producing an ensemble of inverted models that equally fit the observed seismic reflection data, despite the variability between each model.

The main limitation of this approach is that areas in the grid with low signal-to-noise ratio can be matched during the inversion procedure, introducing noisy traces as conditioning data that negatively affect the next trace simulation. Low signal-to-noise ratio areas should be interpreted as high uncertainty areas with lower influence throughout the inversion process. The more recent trace-by-trace model try to mitigate this drawback by avoiding noisy areas in the initial stages of the inversion and revisiting these locations later in the inversion procedure (Azevedo & Soares, 2017).

As an alternative to the trace-by-trace approach, Soares *et al*. (2007) proposes a geostatistical inversion methodology based on direct sequential simulation and co-simulation approaches (Almeida and Journel 1994; Soares 2001). This methodology uses a global approach during the stochastic sequential simulation stage in order for the areas with low signal-to-noise ratio to remain poorly matched throughout the inversion scheme. The final acoustic models tend to reproduce the main spatial patterns accurately, honoring the imposed variograms and the probability distributions that are retrieved from the well-log data. Using this methodology, areas within the seismic volume with low signal-to-noise ratio are poorly matched with the synthetic data, exposing areas of high uncertainty within the resulting subsurface model (Soares *et al*. 2007). This technique also allows the assessing of the spatial uncertainty that is associated with each elastic property (Soares *et al*. 2007; Azevedo & Soares, 2017).

2.1.1. Pre-stack Seismic Data

A fundamental development in geophysics were the Zoeppritz equations (Equations 2.4 and 2.5) (Zoeppritz, 1919). These equations describe the propagation of P-waves in the subsurface, that hit the interface between two rock layers with different elastic properties. This phenomenon implies that P-waves that hit the same location in the subsurface at different incidence angles cause a variations in the recorded seismic amplitudes, due to different amounts of energy being reflected and transmitted in form of S-waves or lost. The amount of energy that gets partialized depends on the angle at which the wave hits the interface and the rock properties in both sides of the boundary. The variation of seismic amplitudes is known as amplitude variation with offset (AVO), where offset is the distance between the source and the receiver, as schematically illustrated in Figure 2.2.

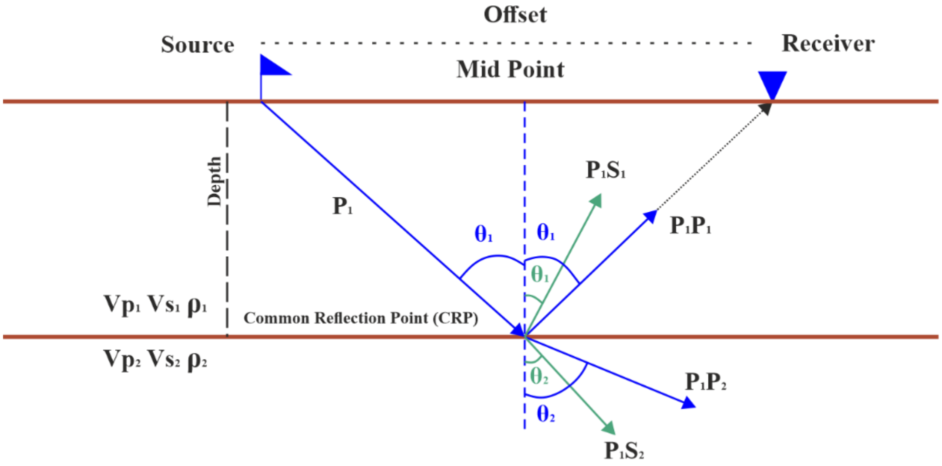

Figure 2.2 - Energy partitioning of seismic waves energy and the link with Zoeppritz equations. Adapted from Simm and Bacon (2014).

Conventional seismic acquisition surveys are designed so that the same point in the subsurface, common reflection point, is sampled several times by seismic waves propagated from different sources and registered in different receivers. From a processing point-of-view the main reason for this design is to enhance seismic imaging through stacking traces, which eliminates random noise and improves the coherent signal (Simm and Bacon 2004; Ylmaz 2011). Nonetheless, the greater availability of high-quality partially stacked seismic reflection data allows for more reliable and less uncertain reservoir models when compared to reservoir models derived exclusively from post-stack seismic reflection data (Azevedo & Soares, 2017).

The use of pre-stack seismic data allows the inference of density, P-wave and S-wave velocity models, contrarily to the traditional acoustic impedance models (Azevedo & Soares, 2017). The objective of an amplitude versus the offset analysis is to interpret the geological cause of the observed amplitude variations. The interpretation is based on the relationship between reflection coefficients and the change in elastic properties provided by the reflection models (Aki & Richard, 1980; Shuey 1985) combined with the relation between the elastic properties and rock physical properties provided with rock physics models (Mavko, 2009).

$$\begin{bmatrix} \sin(\theta_1) & \cos(\theta_1) & -\sin(\theta_2) & \cos(\theta_2) \\ -\cos(\theta_1) & \sin(\theta_1) & -\cos(\theta_2) & -\sin(\theta_2) \\ \sin(2\theta_1) & a\cos(2\theta_1) & c\sin(2\theta_2) & -e\cos(2\theta_2) \\ \cos(2\theta_1) & -b\sin(2\theta_1) & -d\cos(2\theta_2) & -f\cos(2\theta_2) \end{bmatrix} \begin{bmatrix} R_{pp} \\ R_{ps} \\ T_{pp} \\ T_{ps} \end{bmatrix} = \begin{bmatrix} -\sin(\theta_1) \\ -\cos(\theta_1) \\ \sin(2\theta_1) \\ -\cos(2\theta_1) \end{bmatrix} \qquad \text{(Equation 2.4)}$$

Where:

$$a = \frac{V_{p_1}}{V_{s_1}} \qquad b = \frac{V_{s_1}}{V_{p_1}} \qquad c = \frac{\rho_2 V_{s_2}^2 V_{p_1}}{\rho_1 V_{s_1}^2 V_{p_2}} \qquad d = \frac{\rho_2 V_{p_2}}{\rho_1 V_{p_1}} \qquad e = \frac{\rho_2 V_{p_2} V_{p_1}}{\rho_1 V_{s_1}} \qquad f = \frac{\rho_2 V_{s_2}}{\rho_1 V_{p_1}} \qquad \text{(Equation 2.5)}$$

In practice Zoeppritz equations remain difficult to parameterize and interpret, for this reason several authors suggested approximations to the full solution of the Zoeppritz equations, making it possible to implement them in seismic inversion methods and also contributing to the interpretation of the relation between reflection coefficients with elastic subsurface properties.

The Aki & Richards approximation describes the P-wave reflection coefficients as a function of the fractional changes of elastic properties across the reflection interface and the angle of incidence (θ) through Equations 2.6 and 2.7 (Aki and Richards, 1980):

$$R(\theta) = \gamma_1 \frac{\Delta V_p}{\overline{V_p}} + \gamma_2 \frac{\Delta V_s}{\overline{V_s}} + \gamma_3 \frac{\Delta \rho}{\bar{\rho}} \qquad \text{(Equation 2.6)}$$

Where:

$$\gamma_1 = \frac{1}{2}\sin^2(\theta) \qquad \gamma_2 = -4\sin^2(\theta)\left(\frac{\overline{V_s}}{\overline{V_p}}\right)^2 \qquad \gamma_3 = \frac{1}{2} - 2\left(\frac{\overline{V_s}}{\overline{V_p}}\right)^2 \sin^2(\theta) \qquad \text{(Equation 2.7)}$$

Here, $\Delta\rho$, ΔV_p, ΔV_s denote differences across the interface and $\bar{\rho}$, $\overline{V_p}$ and $\overline{V_s}$ are averages across the interface. The ratios $\Delta V_p/\overline{V_p}$, $\Delta V_s/\overline{V_s}$ and $\Delta\rho/\bar{\rho}$ are the P-wave, S-wave and density reflectivity.

2.1.2. Seismic Inversion Constraints

Independently of the type of seismic inversion scheme, most inversions require some form of regularization, damping, or secondary constraint to either stabilize, simplify, or focus the solution space (Claerbout, 1985; Gubbins, 2004). Thore and Blanchard (2015) introduced a new constraint-based on rock physics and reservoir production data to guide the inversion results to more realistic combinations of elastic parameters. This section describes how a petroelastic model constraint can be introduced in the inversion scheme.

Before imposing any constraint to the data, it is necessary to extract the a priori knowledge about the petrophysical properties of the considered field in which the constraint is based on. This information is derived either directly from well-log data or from a previous petroelastic models associated with petrophysical properties such as volume of clay, porosity, saturation of water, saturation of gas and burial depth to compute the expected subsurface elastic response. These PEM constraints provide a sophisticated way to make the relations between the known elastic properties appliable in an inversion scheme by projecting then into a sphere (Figure 2.3a).

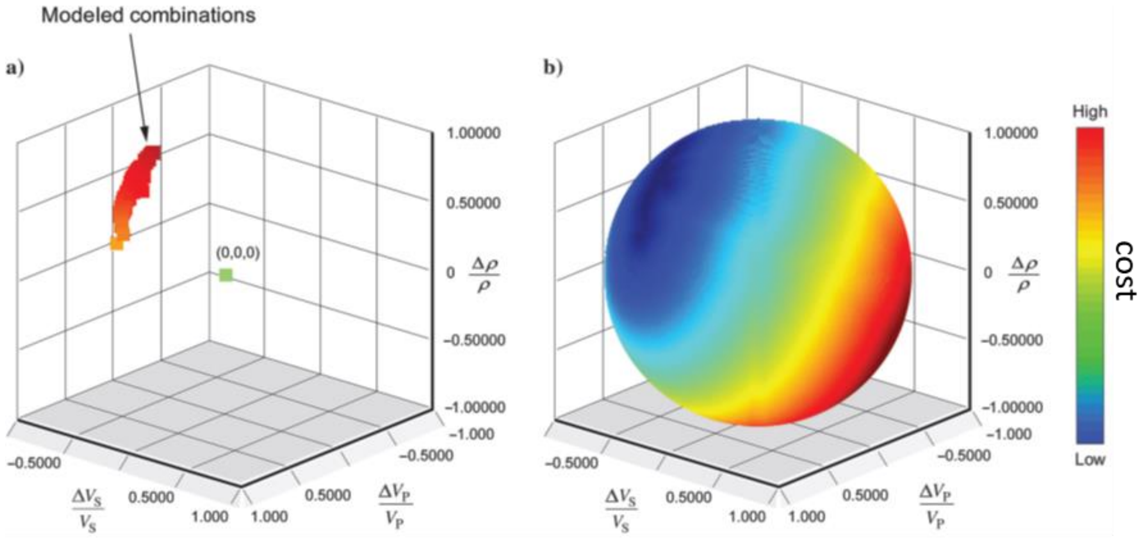

Figure 2.3 - 3D view of the PEM constraint in the 4D case. a) shows the sampled combinations from well-log data; b) shows the computed associated cost for a range of elastic properties combinations (red is high cost and blue is low cost). From Thore and Blanchard (2015).

The concept behind this projection is to constrain the combination of parameters, not the amplitude of the parameters themselves. The sphere is featured by a radius of 1, and it is divided in 360 cells on the azimuth axis, corresponding to the first elastic parameter, and 180 cells on the inclination axis, corresponding to the second elastic parameter. Each position on the sphere has an associated cost depending on whether the value corresponds to a value sampled in the PEM constraint or not (Figure 2.3b). These cost function will be integrated as a penalty term in the inversion algorithm, constraining the solution space. Therefore, the results will tend to reproduce combinations of parameters that exist according to the prior geological and production data.

These type of constrains can be implemented either on 3D or 4D seismic studies. In the time-lapse studies, the constraint is straight forward to implement since the origin point is always assigned to the no anomaly point ($\Delta Vp, \Delta Vs\ and\ \Delta\rho = 0$). In contrast, in the 3D case, the origin point must be assigned to a combination of absolute elastic parameters.

In time-lapse seismic studies, this type of constraint can be beneficial in areas in which several production mechanisms are superimposed, when layers are thin (with low impact in the time shifts) or when 4D signal is quite weak (Thore and Blanchard, 2015). However, as with all constraints, they should be used with care in appropriate scenarios, it is also advisable to compare inversion results that have been generated with and without constraint to check the level of data misfit with increased constraints. All the a priori information that is introduced in the inversion scheme enables it to solve more accurately the production-induced elastic changes but also constrains the solution to a region of model space.

2.2. Time-lapse Seismic

The concepts of time-lapse seismic or 4D seismic has been proved to be a useful tool in reservoir monitoring and management. Time-lapse seismic can be described as repeated 3D seismic surveys over the same area, in which the calendar time represents the 4th dimension added to the data. The changes in the reservoir properties due to production, such as fluid saturation and pressure but also temperature and layer thickness (in the presence of compacting reservoirs), will directly affect seismic properties, such as seismic wave travel-time, seismic velocities, reflection amplitude, and impedances. With the development of 4D seismic in combination with rock physics modelling the production induced changes in the reservoir elastic properties can be monitored over time. The combination of 4D seismic (spatially high coverage) and well production-based data (spatially sparse) closes the loop and provides meaningful insight into the reservoir conditions in the regions around wells and far away from wells, becoming an essential tool in reservoir monitoring.

The successful use of time-lapse seismic data analysis and interpretation relies on the 4D seismic repeatability. Firstly, the different seismic surveys should be acquired under the same conditions, i.e., from dataset to dataset, the experimental acquisition geometry, collection technology, and processing should not change. However, several years after a survey is acquired may be enough time for the technology to evolve, and the same acquisition technology or and processing workflow may not be strictly followed. As a reliable alternative option, the 4D seismic volumes may be re-processed from raw data at the time when the most recent monitor survey is acquired, enhancing the interpretative quality between the different seismic volumes.

In order to measure the repeatability, ensuring that the production induced changes are preserved and properly resolved, Kragh and Christie (2002) defined the normalized root-mean-square ($NRMS$) difference between two monitor (m_t) and baseline (b_t) traces within a certain time window ($t_1 - t_2$) as expressed in Equation 2.8:

$$NRMS = 200\frac{RMS(m_t - b_t)}{RMS(m_t) + RMS(b_c)}$$ (Equation 2.8)

where $NRMS$ corresponds to the percentage of normalized RMS difference of the two traces. The RMS operator for each trace is defined as (Equation 2.9):

$$RMS(m_t) = \sqrt{\frac{\sum_{t_2}^{t_1}(b_t)^2}{N}}$$ (Equation 2.9)

where N corresponds to the number of samples in the selected time interval ($t_1 - t_2$). The value of $NRMS$ of two traces varies between 0-200%, from a perfect correlation to an anti-correlation between both traces, as illustrated in Figure 2.4.

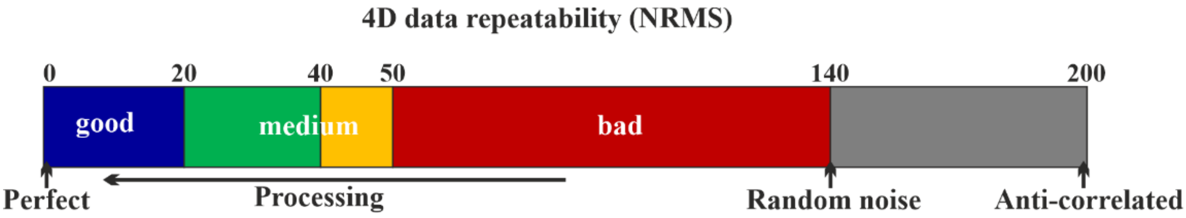

Figure 2.4 - Measure of 4D seismic data repeatability (NRMS) color chart, illustrating various levels of data quality.

In cases where the $NRMS$ is low, the subtraction process between the traces may display spurious residual energy, which is not related to the desired time-lapse signal, often limiting the resolution of the 4D signal (Vedanti *et al*. 2009). The typical value of $NRMS$ is between 60% to 80% for early time-lapse seismic with data which were not acquired with the purpose of 4D seismic studies, however, due to the continuing improvements in field seismic data acquisition and processing, the typical $NRMS$ values for 4D seismic range between 10 to 30% for offshore data (Vedanti *et al*. 2009; Johnson 2013).

2.2.1. Time-lapse Seismic Attributes

In 4D studies time-shifts correspond to temporal effects that come from changes in interval thickness and seismic velocities due to change in the reservoir that are caused by changes in pore pressure and fluid saturation. Time-shifts are common 4D seismic attributes that are mainly exposed as 4D amplitude anomalies resulting of changes in the subsurface properties over a time interval, as schematically represented in Figure 2.5. The time-shift attribute is a cumulative quantity, in which the measurement at a position corresponds to the addition of time-shifts for all layers located above.

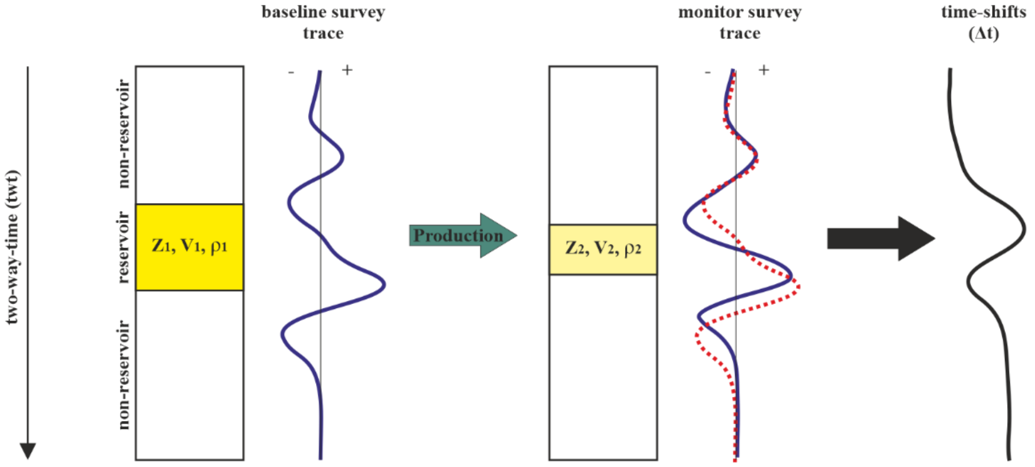

Figure 2.5 - Schematic representation of physical principles of 4D seismic and time-shifts between repeated surveys, illustrating the expected changes due to production in the elastic properties of the reservoir and the effect on wave propagation. Adapted from Hodgson (2009).

There are time-shifts observed throughout the whole subsurface in 4D seismic data. In the overburden it is possible to observe reflector movement due to expansion related to the compression caused by reservoir production, as described by (Hawkins *et al*. 2007; Landrø, 2011) for the Ekofisk chalk reservoir in the North Sea. Inside the reservoir, the time-shift nature becomes more complex due to the coexistence of geomechanical effects and fluid saturation effects. In the underburden, the effect of time-shifts becomes even harder to detect as result of the accumulation of all the phenomenon described previously that are captured due to the cumulative nature of these phenomena.

As mentioned, time-shifts are a measure of the time-lapse changes in the kinematic component of seismic data, depending on the changes in subsurface layer thickness and seismic velocity. Fluid saturation changes commonly dominate the velocity changes component, nevertheless, there is also contribution from structural deformation. The thickness changes are related to geomechanical effects, causing the reflector to move upward and downward. The time-shifts physical expression at zero-offset was derived by Landrø and Stammeijer (2004) as the following (Equation 2.10):

$$\frac{\Delta t}{t} \approx \frac{\Delta z}{d} - \frac{\Delta V}{V} \qquad \text{(Equation 2.10)}$$

in which t, V, z represents travel-time, velocity and thickness of baseline survey, respectively. ΔV and ΔZ represent the time-lapse velocity and thickness changes.

This category of cumulative attributes may be used interpretatively, but in general, have insufficient resolution and stability to be of interest as 4D reservoir characterization attributes. Time-shifts can, therefore, be derived into interval attributes such as the time-strain (Rickett *et al*. 2007), directly reflecting the changes in the reservoir related with well activity. The vertical derivation of time-shifts into time-strain allow for the decreases and increases in P-wave velocity to be distinguished with different polarities and for the value of travel-time fractional change to be obtained (Landrø and Janssen (2002).

During recent years, there has been a range of developments for the measurement of time-shifts, the most commonly used techniques are based on cross-correlation methods (Rickett *et al*. (2006); Kanu *et al*. (2016)). This type of approach measures the similarity between two datasets as a function of the associated lag. This function is often normalized and written as follows (Equation 2.11):

$$NCC_j = \frac{\sum_i a_i b_{i+j}}{\sqrt{\sum_i a_i^2 \sum_i b_i^2}} \qquad \text{(Equation 2.11)}$$

where NCC is the correlation coefficient, j is the lag, and a and b correspond to the baseline and monitor surveys, respectively.

It should be noted that $|NCC_j| \leq 1$, and that NCC_j only equals to 1 when two time series are perfectly identical (Gubbins, 2004). By finding the maximum correlation coefficient, the time-shift is returned in proportion to the lag. Standard warping algorithms estimate time-shifts by taking time windows of data from one trace and searching over several vertical displacements to maximize the correlation obtained. The cross-correlation of two seismic datasets is computed using a sliding window function to capture the spatial and vertical variation of time-shifts (Hodgson, 2009), a commonly used function is the boxcar window function.

Several cross-correlation based methods are available in the literature; however, in the scope of this thesis, only the 3D warping approach (Hall *et al*. 2002) is described.

Hall *et al*. (2002, 2005) proposes a 3D warping approach that provides a way to align two repeated seismic surveys as part of a full cross-correlation scheme. Before the 3D warping, the two seismic datasets are processed through a cross-equalization scheme that aims to account for variations in phase and amplitude between the two volumes. The 3D warping scheme is based on cross-correlation of small data volumes from the two surveys, at nodal points positioned on picked horizons that are evenly distributed in the horizontal direction. Afterward, for each point, a warp vector is assigned for each node (Hall *et al.* 2005). Through iterative testing of a range of possible values, it is possible to determine the best warping parameters in three directions (inline, xline, and TWT).

Time-shifts obtained using this warping approach are generally stable, as they are calculated along horizons (Hall *et al*. 2002). However, the way of finding the best 3D warping parameters through trial and error optimization is often time-consuming. Furthermore, it requires several stable reflectors to ensure the most accurate vertical warping calculation.

Cross-correlation algorithms generally do an excellent job in minimizing the most notorious artifacts, and the obtained time-shifts attributes may be employed directly for characterizing 4D changes in the subsurface (Hatchell *et al*. 2005). Nonetheless, there is generally a weight between attribute stability and resolution imposed by the selected correlation window-length, which, combined with the subsurface time-lapse changes, limits the value of this attribute to the interpreter (Williamson *et al*. (2007).

Therefore, other non-cross-correlation based methods were developed to try to minimize this drawback introducing a global solution which considers the entire trace in order to obtain more robust and reliable time-lapse attributes (Williamson *et al*. 2007; Hale, 2013).

Williamson *et al*. (2007) recast the warping as a non-linear inverse problem, aiming to determine the time-lapse change in seismic velocity for each trace, accounting concurrently for the observed time-shifts and changes in amplitude. This method is based on non-cross-correlation techniques, providing more stable and consistent results than the classical decoupled approaches (Williamson *et al*. 2007). The dependence of time-shifts on velocity changes $(\Delta V_p/V_p)$ is expressed as (Equation 2.12):

$$m(t_i) = b\left(t_i + \sum_{k=1}^{i} -\frac{\Delta V_p}{V_p}\right) + \Delta A \qquad \text{(Equation 2.12)}$$

where i is the index of sample number, b stands for the monitor trace, k is the current index and ΔA stands for the change in amplitude expressed as a function of $\Delta V_p/V_p$.

The warping problem is then set as matching the shifted monitor trace to the amplitude adjusted baseline. Appling a least-square optimization algorithm to Equation 2.12, allows to minimize the difference between the left and right terms of the equation and recover the time-lapse velocity perturbation, the time-shift is used as an optimization parameter and the change in thickness $\Delta Z/Z$ is assumed to be negligible when substituting the change in velocity quantity into the shifted monitor trace (Williamson *et al*. (2007). Posteriorly Grandi *et al*. (2009) implemented Williamson's method by modifying the algorithm in a new approach that allows to invert for time-strain $(\Delta t/t)$ instead of only velocity changes, excluding the amplitude changes term.

Two seismic parameters can measure the changes between baseline and monitor seismic volumes: a change in travel time (low-frequency component) and a change in amplitude (high-frequency component) due to production effects (Figure 2.6).

The 4D warping inverts for the local relative change of velocity change $(\Delta V_p/V_p)$ and time-strain $(\Delta t/t)$ that accounts simultaneously for the time shift and the change in amplitude between base and monitor and aligns the monitor survey to the baseline reference survey by iteratively matching both the measured time-shifts and the amplitude changes between the two repeated surveys. This technique benefits from being data-driven and does not need a prior geological and dynamical information at the time where the monitor has been acquired.

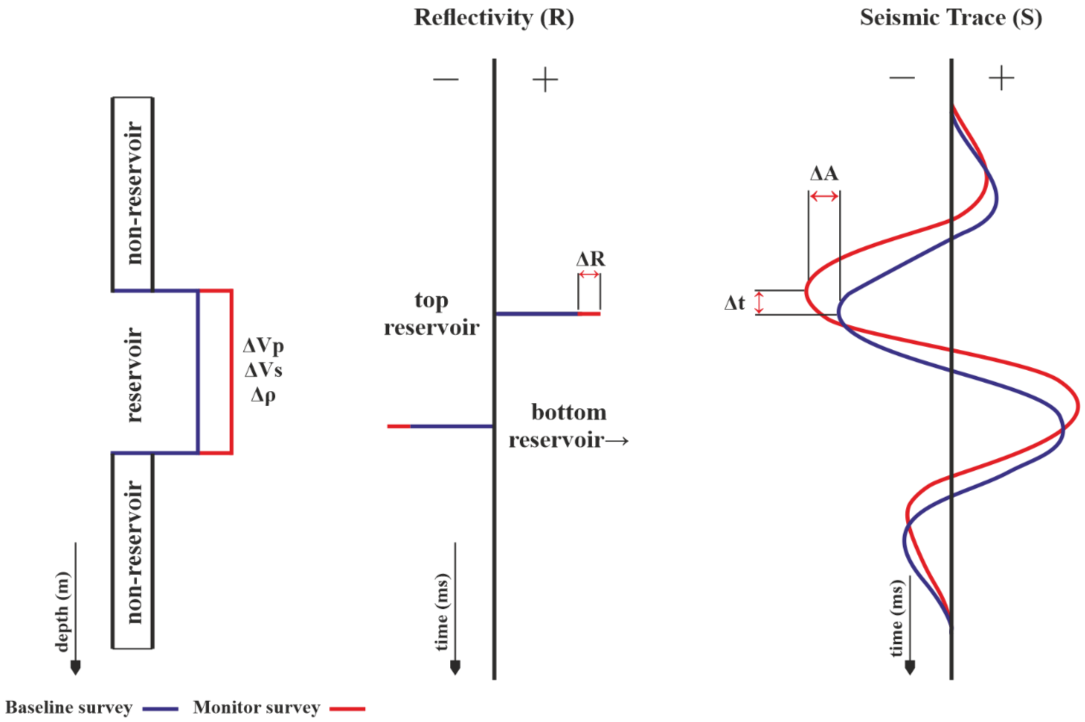

Figure 2.6 - Schematic diagram linking the reflectivity changes (ΔR) and changes in the seismic trace. The changes in amplitude (ΔA) are a function of elastic change in the reservoir and vertical time-shifts (Δt). Adapted from Omofoma (2017).

The interest in warping techniques is then twofold (Williamson *et al*. 2007): first, to improve the interpretability of the different signals, and secondly, to generate attributes which may enhance the interpretation of imprinted production and injection effects in the reservoir.

As opposed to the time-shift attribute, which is a cumulative property, time-lapse velocity change is an interval attribute. Thus, it is sensitive to changes in fluid saturation and pore pressure inside the reservoir, reflecting changes at specific locations. Furthermore, the constant development of new sophisticated techniques allows for ΔVp/Vp attribute to start becoming a standard quantity in time-lapse seismic studies, contributing to a better seismic processing, analysis, and interpretation of 4D seismic.

2.2.2. 4D seismic Interpretation

Qualitative time-lapse seismic interpretation is primarily based on the visual detection of time-lapse seismic changes, or the absence of change, and understanding how these changes relate to the reservoir behavior and production mechanisms. It is also crucial to differentiate the changes that are likely related to problems in acquisition and processing from the ones driven by production. The integration of 4D data into reservoir simulation models began on a qualitative basis to reduce uncertainties (Lumley and Behrens, 1999; Elde *et al*. 2000; Pannett *et al*. 2004), mainly by identifying pathways of injected water, sealing faults/compartments, bypassed oil and to monitor saturation fronts, which resulted in improved reservoir characterization and consequently improved history matching.

Qualitative inferences are based on the assumption that one production-related effect completely dominates the others; however, two or more production-related effects can influence the reservoir seismic properties, which leads to ambiguities in the interpretation. Fluid saturation and pressure effects often overlap to different extents in the reservoir. In order to better explore the uncertainties that arise from competing effects production-related data combined with 4D seismic data provide insightful information related to the reservoir dynamics.

For reservoir management purposes, quantitative estimates of reservoir changes are often desired. To get the most value from 4D seismic technology, time-lapse data is inverted to obtain estimates of saturation and pressure changes, in order to integrate 4D seismic data into dynamic simulation models. The decisive point in quantitative interpretation is the separation of pressure and saturation effects, which requires the accurate knowledge of their contributions in the time-lapse response (Landrø, 2001).

The ability of time-lapse seismic data to distinguish pressure and saturation changes is believed to be dependent on 4D seismic data non-repeatability that is related to the presence of non-production related artifacts (noise) but also with 4D seismic signal (the magnitude of the change in reservoir elastic properties due to production) that depends primarily on seismic properties of the reservoir and on how significant the effect is production (Johnston, 2013).

Despite significant improvements in acquisition and processing over the past decades, accurate quantitative estimation of changes in reservoir using time-lapse data attributes, mainly of pressure, remains a challenge (Roeste *et al*. 2015) for a wide variety of accepted reasons (Alvarez and Macbeth, 2014). The limitation for pressure includes most significantly the uncertainty in obtaining an accurate description of rock stress sensitivity and geomechanical response (Omofoma and MacBeth 2016). Fluid saturation changes, on the other hand, are calculated with better accuracy in general, although the impact of pressure uncertainty on saturation remains unclear. Due to the sensitivity of these estimates, the quantitative interpretation studies should be preceded after a broad qualitative assessment (Johnston, 2013).

2.3. Rock Physics Models

The petrophysics discipline studies the physical and chemical properties that describes the behavior of rocks and soil, based on the analysis of logs and cores obtained from the wells. This discipline mainly intends to describe the reservoir properties and seeks to measure two types of properties:

i) Conventional rock physics properties such as the fluid saturation, corresponding to the fraction of pore space occupied by the fluid; the volume of clay, corresponding to the percentage of clay on a complete rock volume; porosity, corresponding to the percentage of the porous space occupied by a fluid in the rock. These various properties, once reconstituted, allow to assess the volume of oil and gas in place;

ii) Petrophysical properties deduced from rock mechanics, being the measurements made directly on rocks to calculate mechanical properties such as the different elastic moduli (incompressibility, shear moduli, Young's moduli, and Poisson's ratio). These properties are then calibrated and used to interpret the seismic data.

Where petrophysics seeks to contribute to the description of a reservoir, rock physics seeks to establish the link between the properties of the rock and the seismic response (Mavko *et al*. 2009). The two main elastic parameters that affect seismic velocities are the bulk and shear modulis. Rock physics models make it possible to study and link the properties that will affect the propagation of seismic waves through the subsurface.

The rock physics is also the link between static and dynamic properties of a reservoir rock therefore, it is a crucial aspect to understand the changes in the seismic response due to reservoir production. Although the primary concern in 4D studies is about the changes in the elastic properties, rather than their absolutes values, the rock-physics models are always essential for any time-lapse seismic study (Johnston 2013).

Compressional waves modify the shape and the volume of the rock matrix and the fluid-filled pore space, therefore P-wave velocity is sensitive to fluid changes depending on the magnitude of the fluid compressibility relative to the reservoir matrix compressibility. Consequently, the more compressible the rock matrix, the more sensitive P-wave will be to changes in pore-fluid compressibility; therefore, the same behavior is expected in the change of acoustic impedance. On the contrary, shear wave propagation changes the rock matrix shape but not the volume. Thus, S-wave is relatively insensitive to fluid changes at seismic frequencies, changing only in response to changes in fluid density (Johnston 2013).

2.3.1. Solid Phase

There are a multitude of rock physics models in the literature (Avseth *et al*. 2005). However, none gives a perfect vision of the relationships between the properties of rocks and fluids and measurable seismic parameters. In the literature, rock physics models are divided into three types (Avseth *et al*. 2005; Mavko *et al*. 2009): empirical models, inclusion models, and granular media models, however, there can also be a hybrid approach that combines different models.

Empirical models are based on calibrations made using *in situ* measurements. These models are established based on a simple principle of adjusting a regression curve to a set of real data (Simm and Bacon 2014), fixing if necessary, a particular hypothesis on the function of this curve (i.e., a given lithology or a particular depositional environment). The two most common empirical models are the Castagna-Batzle relationship (Castagna *et al*. 1985) between P- and S-wave velocities, and the Gardner relationship between Vp-Vs (Gardner *et al*. 1974).

Inclusion models are mostly used for carbonate rocks, assuming that the rock is as elastic solid containing pore spaces in terms of inclusions (cavities) with a defined aspect ratio that is a proportional relationship between the width and height of the fissures. According to Kuster and Toksöz (1974), most of the models that use this approach consider the rock pores and grains as being ellipsoidal or penny shaped inclusion. Nonetheless, it is still impractical to compare the actual rock pore micro-geometry with the pore geometry implied in the model (Avseth *et al*. 2010). These types of models assume no interaction between pores and are based on Kuster-Toksöz theory (Kuster and Toksöz 1974).

Granular media models describe the rock as an assemblage of separated grains in contact with each other with a determined stiffness. These models are mostly applied on sandstones (Simm and Bacon 2014) and are based on the Hertz-Mindlin contact theory (Mindlin 1949; Dvorkin *et al*. 1998). Such models are used to describe the effective bulk and shear modulis taking into consideration the effective stress sensitivity of the rock and assuming that the frame is a dense pack of random identical spherical grains subjected to an effective pressure with a given critical porosity and an average number of contacts per grain (Avseth *et al*. 2010).

The concept of critical porosity ($\emptyset_c$) was firstly introduced in Nur *et al*. (1998) as a fundamental conception to relate physical properties in rocks. Critical porosity detaches the acoustic and mechanical behavior of the rock into two separate domains. For porosities higher than the critical porosity, the rock becomes a suspension, in which the fluid phase is load-bearing, oppositely for porosities lower than the critical porosity the mineral phase become the load-bearing (Mavko *et al*. 2009) phase. In short, the critical porosity is the value that points the porosity limit between a fully saturated rock and a suspension. This transition is defined by the empirical relationship in Raymer velocity-porosity model (Raymer *et al*., 1980).

The coordination number of a grain pack is the average number of contacts that each grain has with the neighboring grains. Experimental results on rock samples (Bernal and Manson, 1960; Mavko *et al*. 2009) detail the coordination number for a perfect packing of identical spheres ranging from 6 for a simple cubic packing to 12 for hexagonal packing. The coordination number in granular media models should be determined from core analysis or estimated by comparing well-logs and rock physics models (Smith *et al*. (1929); Mavko *et al*. 2009). The results obtained in Smith *et al*. (1929) point to several key conclusions: the coordination number increases with decreasing porosity (resulting from tighter packing); the coordination number varies from ~6.9 for a loose packings to ~9.1 for tight packings; the coordination number varies extensively throughout each sample, from 4 to 12 meaning that the mean alone does not capture the variability.

The bulk and shear moduli of a rock can be described in various ways depending on the assumptions made and properties of the rock available, based on whether the information on geometric details of the grains and the matrix structure is included or not (Mavko *et al*. 2009). Otherwise, the effective elastic moduli are estimated from information of the volume fractions and the elastic properties of each constituent of the modelled geological material (Mavko *et al*. 2009). Such models are refereed in the literature as theoretical bound models. Moreover, models that include geometrical information about the rock are referred as contact models.

The Voigt-Reuss (Reuss, 1929; Voigt, 1907) and the Hashin-Shtrikman (Hashin and Shtrikman, 1963) models, are theoretical bound models that predict an upper and lower limit of the elastic bulk and shear moduli of a rock (Figure 2.7a and 2.7b).

The simplest estimate for an upper and lower bound for the bulk and shear moduli of a rock, can be computed using the Voigt-Reuss model (Mavko *et al*. 2009). Regardless of their simple form, this type of model is robust and avoids the usage of complicated idealizations and approximations of the subsurface (Avseth *et al*. 2005). The bounds are derived from an empirical basis assuming the most stiff and soft rock possible. The upper Voigt bound (Voigt, 1907) describes the most elastic stiff rock possible whereas the lower Reuss bound describes the most elastic soft rock possible (Reuss, 1929). Hill (1952) proposes an adaptation for the estimate of the effective moduli, using the arithmetic average of these two bounds, this modification gives origin to the Voigt-Reuss-Hill average (M_{VRH}), which allows to estimate the elastic moduli (K_{mat} and μ_{mat}) of the mineral mixture that lies halfway between the Voigt upper and Reuss lower bounds (Mavko *et al*. 2009), this average is useful when an estimate of the moduli is needed, not just the allowable range of values.

The Voigt upper bound (Equation 2.13), the Reuss lower bound (Equation 2.14) and the Voigt-Reuss-Hill average (Equation 2.15) used to compute the matrix elastic moduli of a mixture of N materials are expressed as follows (Avseth *et al*. 2005):

$$M_V = \sum_{i=1}^{N} f_i M_i \qquad \text{(Equation 2.13)}$$

$$\frac{1}{M_R} = \sum_{i=1}^{N} \frac{f_i}{M_i} \qquad \text{(Equation 2.14)}$$

$$M_{VRH} = \frac{M_V + M_R}{2} \qquad \text{(Equation 2.15)}$$

where f_i is, the volume fraction and M_i is the elastic moduli of each phase i. Most commonly, only two mineral phases are applied, sands and shales. Therefore, these equations can be conviniently expressed for a matrix composed of sand and clay materials using the Voigt-Reuss-Hill averages as follows (Equation 2.16 and Equation 2.17):

$$K_{mat} = \frac{1}{2}\left(V_{clay}K_{clay} + \left(1 - V_{clay}\right)K_{sand} + \frac{1}{\frac{V_{clay}}{K_{clay}} + \frac{K_{sand}}{\left(1 - V_{clay}\right)}} \right) \qquad \text{(Equation 2.16)}$$

$$\mu_{mat} = \frac{1}{2}\left(V_{clay}\mu_{clay} + \left(1 - V_{clay}\right)\mu_{sand} + \frac{1}{\frac{V_{clay}}{\mu_{clay}} + \frac{\mu_{sand}}{\left(1 - V_{clay}\right)}} \right) \qquad \text{(Equation 2.17)}$$

Where V_i, K_i and μ_i are the volume, the bulk and shear modulis of the mineral phases (sand and clay).

Another model used to compute the upper and lower bounds of the elastic moduli is the Hashin-Shtrikman model (Hashin and Shtrikman, 1963). These bounds are narrower than the Voigt-Reuss bounds (Mavko *et al*. 2009). The conceptual geological interpretation of the lower bound, for a two-phase composition, is a spherical material where the cement is deposited away from the grain contacts (Mavko *et al*. 2009). The upper bound can be visualized in the same manner; however, the sediment is deposited at the grain contacts.

The Hashin-Shtrikman bound model assumes that one of the mineral constituents has both the maximum bulk and shear moduli, while the other constituent has the minimum bulk and shear moduli, which is not always the case, for example in a mixture of calcite and quartz (Mavko *et al*. 2009). When this assumption is not valid the bounds are calculated by the Hashin-Shtrikman Walpole (HSW) bounds, also referred to as the modified Hashin-Shtrikman bounds (Equation 2.18 and 2.19):

$$K_{HSW} = K_1 + \frac{V_2}{(K_2 - K_1)^{-1} + V_1\left(K_1 + \frac{4}{3}\mu_m\right)^{-1}} \qquad \text{(Equation 2.18)}$$

$$\mu_{HSW} = \mu_1 + \frac{V_2}{(\mu_2 - \mu_1)^{-1} + V_1\left(\mu_1 + \frac{\mu_m}{6}\left(\frac{9K_m + 8\mu_m}{K_m + 2\mu_m}\right)\right)^{-1}} \qquad \text{(Equation 2.19)}$$

where the indices 1 and 2 refer to each component of the mineral mixture, which most commonly correspond to a sand and clay mixture. V, K, and μ are the volume fractions, bulk and shear moduli, respectively, for each component. In this model, the upper bounds are computed when K_m and μ_m are the maximum bulk and shear moduli of the two constituents, and the lower bounds are calculated when $K_m$and μ_m are the minimum bulk and shear moduli of the two mineral phases.

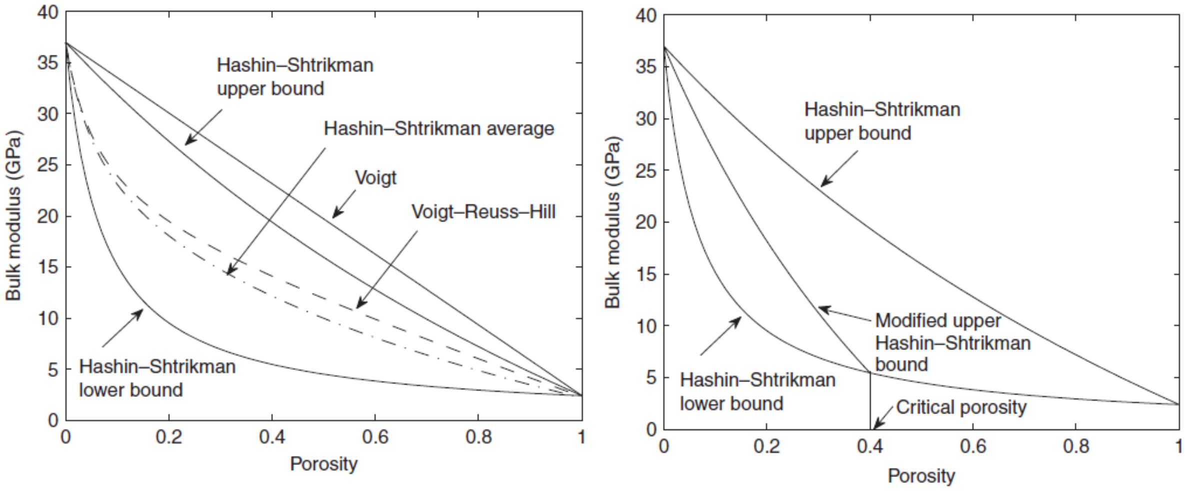

Figure 2.7 - a) Hashin-Shtrikman and Voigt-Reuss bounds for bulk moduli in a quartz-water mixture. The Voigt-Reuss-Hill curve is an average of the Voigt Upper and Reuss lower bounds; b) Hashin-Shtrikman and modified Hashin-Shtrikman bounds for bulk moduli in a quartz-water system. From Mavko *et al*. (2009).

Contrarily to the theoretical bound models, the contact models take the pore and grain geometry of the rock into account and model the grain interaction. The Hertz-Mindlin grain-contact model (Hertz, 1882; Mindlin, 1949) does not estimate the bounds of the rock elastic moduli, instead it models the dry bulk and shear moduli of a rock frame, assuming a dense and random pack of identical spherical grains subjected to a hydrostatic pressure (Mavko *et al*. 2009). The effective bulk and shear moduli are given by the Equation 2.20 and Equation 2.21, respectively.

$$K_{dry}^{HM} = \sqrt[3]{\frac{n^2(1-\emptyset_0)^2\mu_{mat}^2}{18\pi(1-v_s)^2}P_{eff}} \qquad \text{(Equation 2.20)}$$

$$\mu_{dry}^{HM} = \frac{5-4v_s}{5(2-v_s)}\sqrt[3]{\frac{3n^2(1-\emptyset_0)^2\mu_{mat}^2}{2\pi^2(1-v_s)^2}P_{eff}} \qquad \text{(Equation 2.21)}$$

where K_{dry}^{HM} and μ_{dry}^{HM} represent the dry-rock bulk and shear moduli, respectively. μ_{mat} represent the shear moduli and v_s represents the Poisson's ratio of the grains at initial porosity ($\emptyset_0$), effective pressure (P_{eff}) with a coordination number n.

2.3.2. Liquid Phase and Gassmann Fluid Substitution

The density and bulk moduli of the single-phase fluids are calculated using the empirical correlation derived by Batzle and Wang (1992), which considers the temperature, salinity, and pressure. For a mixture of various fluids, the effective fluid bulk moduli (K_{fl}) can be estimated using an appropriate mixing law, such as the harmonic averaging (Domenico, 1974) as follows (Equation 2.22):

$$K_{fl} = \left(\frac{\frac{V_w}{\emptyset}}{K_w} + \frac{\frac{V_{HC}}{\emptyset}}{K_{HC}} \right)^{-1} \qquad \text{(Equation 2.22)}$$

Where V_w and V_{HC} are the volume fractions of water and hydrocarbons respectively, K_w and K_{HC} are the bulk moduli of water and hydrocarbons and ∅ represents porosity.

When a particular fluid or a mixture of several fluids occupy the pore space, pore fluid effects are usually modeled using the Gassmann model (Gassmann 1951), this model allow the computation of the change in bulk moduli associate with a change in the fluid filling the pore space. For an accurate interpretation of seismic amplitudes, it is mandatory to understand how rocks are affected by changes in fluid saturation (Simm and Bacon 2014). Therefore, some assumptions for the successful use of Gassmann's fluid substitution model should be considered (Simm and Bacon 2014):

- The porous rock is homogeneous and isotropic, meaning that the rock frame must be formed of one mineral or if it is composed of more than one mineral, their stiffness should be similar;
- The pores are interconnected. The pore space is completely connected, the fluid should be moveable, and fluid pressure must be uniform;
- Relative motion between fluid and solid during elastic wave propagation is negligible (valid at low frequencies only);
- The pore fluid does not interact with the solid material, meaning that the matrix elastic moduli is unaffected by fluid saturation;
- Rock pore fluid is frictionless (low-viscosity fluid).

To compute the effective bulk moduli (Equation 2.23) and shear moduli (Equation 2.24) of a two-phase medium (fluid and mineral matrix), the Gassmann equations are formulated in the following form:

$$K_{sat} = K_{dry} + \frac{\left(1 - \frac{K_{dry}}{K_{mat}}\right)^2}{\frac{\emptyset}{K_{fl}} + \frac{1-\emptyset}{K_{mat}} + \frac{K_{dry}}{K_{mat}^2}} \qquad \text{(Equation 2.23)}$$

$$\mu_{sat} = \mu_{dry} \qquad \text{(Equation 2.24)}$$

Where K_{sat}, μ_{sat}, are the bulk and shear modulis of the fluid-saturated rock and K_{dry} and μ_{dry} represent the dry-rock bulk and shear modulis.

Regardless of the fluid saturating the rock (water, oil, or gas), the shear moduli is independent of the pore fluid, because all fluids are unable to resist changes in shape of the rock when stress is applied (Bacon *et al*. 2007) therefore, shear moduli is not sensitive to pore fluids (Equation 2.24).

The compressional and shear wave velocities on fluid saturated rocks in a homogeneous isotropic medium can be obtained with the following equations (Equation 2.25 and Equation 2.26 respectively):

$$V_p = \sqrt{\frac{K_{mat} + \frac{4}{3}\mu_{sat}}{\rho_{sat}}}$$ (Equation 2.25)

$$V_s = \sqrt{\frac{\mu_{sat}}{\rho_{sat}}}$$ (Equation 2.26)

Where ρ_{sat} represents the density of the fluid-saturated rock. The elastic moduli can now be estimated through a fluid substitution model; meanwhile, the bulk density (Equation 2.29) is calculated as the volume average of the solid (Equation 2.27) and liquid phase (Equation 2.28) as:

$$\rho_{matrix} = \rho_{sand}\left(1 - V_{clay}\right) + \rho_{clay}V_{clay}$$ (Equation 2.27)

$$\rho_{fluid} = \rho_{water}S_{water} + \rho_{oil}S_{oil} + \rho_{gas}S_{gas}$$ (Equation 2.28)

$$\rho_{sat} = \rho_{fluid}\emptyset + (1 - \emptyset)\rho_{matrix}$$ (Equation 2.29)

Where ρ_{matrix}, ρ_{sand}, ρ_{clay}, ρ_{fluid}, ρ_{water} and ρ_{gas} are densities of matrix, sand, clay, fluid, water and oil respectively and S_{water}, S_{oil} and S_{gas} denote the saturation of water, oil and gas.

2.3.3. Rock Physics of 4D seismic

During production, changes in fluid saturation and pore pressure are expected. The magnitude of these changes is controlled by the reservoir rock and fluid properties. Figure 2.8 illustrates the combined effects of changes in pore pressure and fluid saturation on P-wave velocity and S-wave velocity which are directly related with the dynamic changes in the reservoir due to production.

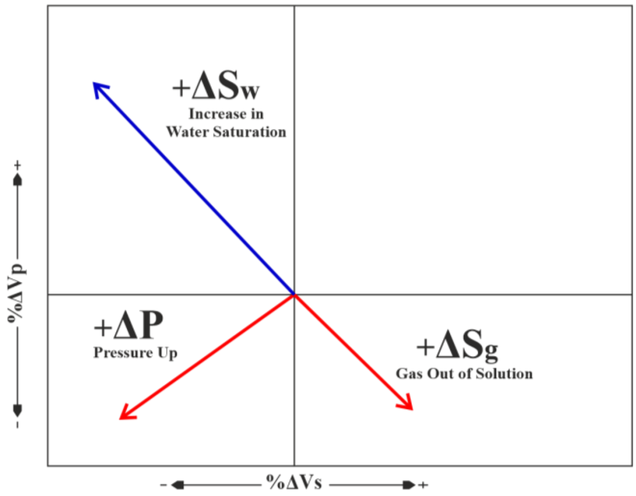

Figure 2.8 - Relations between the change in P-wave and S-wave velocity due to changes in the reservoir during production. Highlighting that two elastic parameters allow the differentiation between pressure and saturation dynamic effects. Adapted from Gervais *et al*. (2010).

The main elastic time-lapse changes observed during reservoir production may be summarized in the following points (Johnston 2013):

- P-wave velocity and density increase for water replacing oil and gas (the same behavior for acoustic impedance);
- P-wave velocity and density decrease for gas replacing oil or gas (the same behavior for acoustic impedance),
- S-wave velocity remains relatively constant under fluid substitution;
- P-and S-wave velocities and density increase in the reservoir due to pressure depletion or compaction (the same behavior for acoustic impedance);
- P- and S-wave velocities decrease during injection due to pressure increase (overpressure), the same elastic behavior happens to impedances;
- P- and S-wave velocities change in the overburden and underburden in response to compaction.

It is also important to note that due to heterogeneity of a reservoir formation, some of the elastic change described may co-occur during reservoir production, increasing the interpretation uncertainty of 4D results (Nasser *et al*. 2016), therefore it is essential to discriminate both effect of pressure and saturation that characterize the seismic signature.

During production, water replaces oil, and gas might become out of solution depending on the pressure reaching bubble point (Figure 2.9a); these phenomena lead to fluid saturation changes accompanied with fluid contact movement, which can be related with the change in seismic velocity and consequently the measured seismic response (Figure 2.9b). Gassmann's equation (Gassmann 1951) relates the dependence of seismic velocity as a function of the rock bulk moduli and density, taking into consideration the rock frame, the grain or mineral frame, and the effects of fluid saturation inside the rock pores.

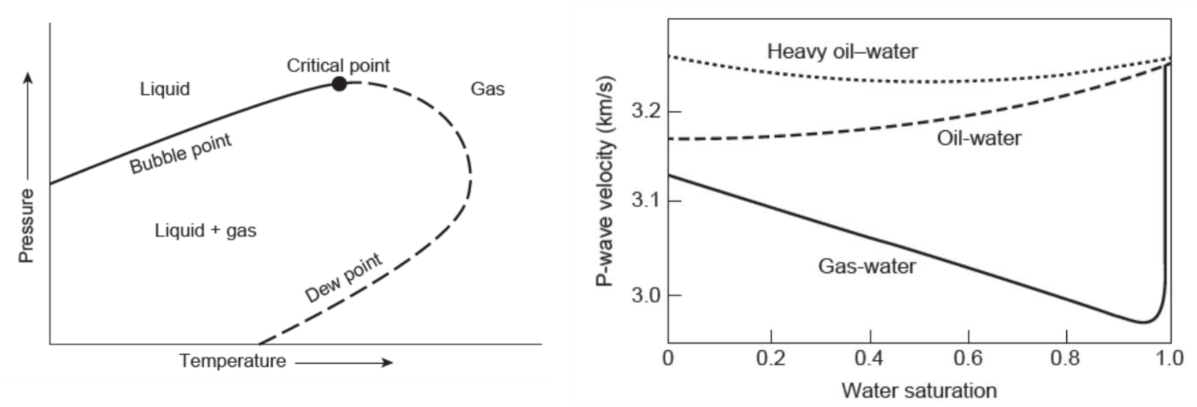

Figure 2.9 - The effects of changes in saturation and pressure during production. a) Gassmann predictions for changes in P-wave velocity for different homogeneous fluid mixtures; b) phase diagram for hydrocarbons allowing to distinguish between single phase or mixture of liquid and gas phases depending on temperature and pressure changes. From Johnston (2013).

Regarding pressure or stress variations, changes in pressure result in changes in rock and fluid bulk moduli, rock shear moduli, density, and porosity in the reservoir-rock framework. The relationship between seismic velocity and pressure can be obtained using theoretical or empirical physics models and ultrasonic measurements on several cores taken from various formations (Landrø *et al*. 2003). Johnston (2013) points out most predictions of velocity sensitivity to pressure have a high degree of uncertainty: core measurements are subject to formation damage and sampling biases; laboratory measurements are often made assuming hydrostatic conditions; velocity change in the reservoir also depends on the stress path during depletion and changes in non-hydrostatic stress can induce anisotropy.

A pertinent way to classify the 4D seismic response regarding reservoir production effects is to define simple two categories of effects, hardening effect, and softening effect. The hardening effect reflects a positive time-lapse response, and it represents the increase of changes in acoustic impedance and P-wave velocity that are related with the decrease in pore pressure and gas saturation and the increase in water saturation, on the other end, the softening effect reflects a negative time-lapse response and represents a negative change in acoustic impedances and P-wave velocity, that are related with the increase in pore pressure and gas saturation and the decrease in water saturation.

3. Methodology

This section comprises a description of the methodologies applied to the data in order to achieve the proposed objectives. The several steps that encompass the methodology applied were accomplished using an in-house geoscience and reservoir integrated platform. The methodology can be sub-divided in broader operations (sub-topics 3.1 to 3.5) which describe the tools and methods that are used in a transversal way through the workflows. These broader operations encompass the estimation of a set of wavelets used for the inversion, the definition of the inversion grid, the warping method that aims at aligning the monitor survey to the baseline reference survey, the 3D and 4D stochastic inversion method and generation of the PEM constraints based on *prior* reservoir knowledge.

3.1. Wavelet Estimation

To prepare the following steps, firstly, it is necessary to obtain a set of representative wavelets for each partial angle stack. These wavelets are going to be used in several stages during this study, therefore, it is crucial to ensure that they are representative of each sub-stack volume since it improves the convergence of all the methods going forward. The wavelet estimation is done using an in-house tool dedicated to global wavelet estimation in a multi-well and multi-angle stack environment that follows a specified workflow comprising the following five steps: statistical wavelet processing, trace selection, global optimization, variable phase optimization and optimized velocity laws at wells, however, not all the steps are mandatory. In this specific study, the wavelet estimation workflow finishes after the global optimization step (Figure 3.1).

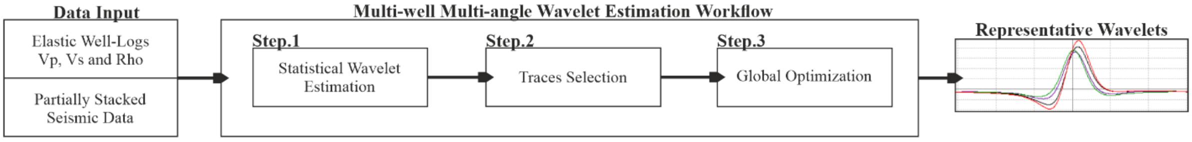

Figure 3.1 - General workflow conducted to estimate a set of representative wavelets for each partially stacked seismic volume.

In the first step, the wavelets are estimated using only seismic data. The purpose of the second step is to select the traces that will be used to compute the final wavelets, the trace selection is performed based on the correlation computed at each position around each well. The last step consists of a global optimization computed for all the wells and all the angle at once with a single phase, the best amplitude per angle stack and a single time-shift per well, which globally minimizes the residuals between real and synthetic seismic.

3.2. Definition of the Hybrid Grid

The generation of the grid to be used in the seismic inversion is one of the fundamental steps in this study. Generally, one of the main limitations in the link between both seismic and flow simulation is the grid scaling problem, where the upscaling and downscaling processes are required to allow the comparison between these two domains (Riazi *et al*. 2013).

The time-lapse signal is obtained with higher lateral resolution (12.5 or 25 meters) and poorer vertical resolution (10 to 20 meters); complementary, the reservoir grid corresponds to a set of layers with very high vertical resolution (1-5 meters) and a limited lateral resolution (50-100 meters) (Thore 2011). Therefore, the inversion grid used in this project aims to solve these scaling problems combining the spatial sampling of the seismic survey and the vertical sampling of the reservoir grid, in a hybrid grid (HG) that honors the overall reservoir stratigraphic structure and maintains the continuity throughout faults (Figure 3.2).

This hybrid grid has the advantage of preserving the relationship between the inversion layers and the reservoir grid layers throughout the inversion, from a trace to the next, without losing information with the ultimate purpose of honoring the connectivity between layers for reservoir simulation (Thore 2011).

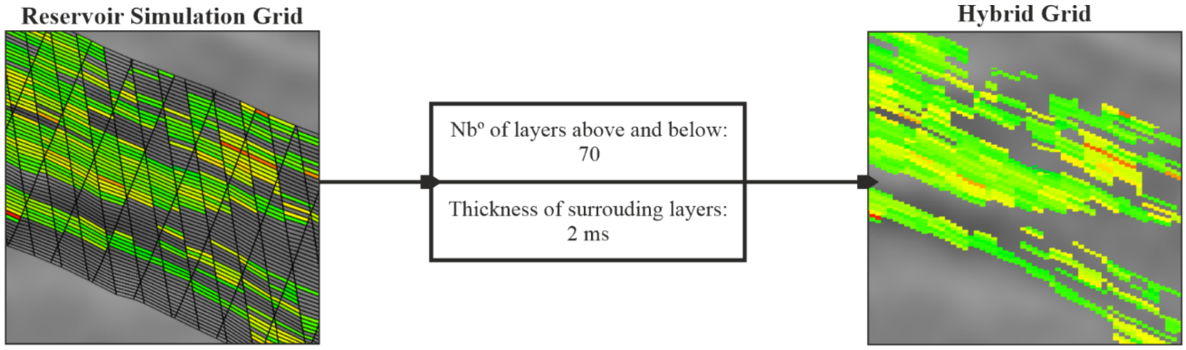

Figure 3.2 - Schematic illustration of the transition between the reservoir simulation grid to the seismic inversion grid as well as required parameterization, honoring the reservoir grid information.

The hybrid grid was created based on the reservoir grid geometry of 65 layers (in time-domain) with a thickness of around 2ms for each layer according to the reservoir grid scale and adding a layering of 70 layers above and below the reservoir, making a total of 205 layers, in order to cover the amplitude anomalies of seismic data.

3.3. Time-lapse Seismic Warping

The warping process is a data-based inversion which realigns base and monitor surveys and delivers both a time-shift and ΔVp/Vp attribute volume for each angle stack. Standard correlation-based methods and non-linear time-shift inversion, described previously in Section 2.2.1, are mainly used to align base and monitor surveys and generate time-shift models which are used interpretatively as 4D seismic attributes or to apply time-shift corrections to seismic volumes or elastic models.

Accordingly, this warping method can generate attributes of direct interest to enhance time-lapse interpretation and present a reliable way to align the traces of two seismic vintages. As described in Williamson *et al*. (2007) the inversion is posed as the match of the non-aligned monitor trace to the amplitude-adjusted base trace and is expressed as a least-spare optimization with respect to the velocity-change parameter expressed as follows (Equation 3.1):

$$C = \sum_{i=1}^{N}\left(b(t_i) - m\left(t_i - \sum_{1}^{i}\frac{\Delta V_k}{V_k}\right) - \omega * \frac{\partial}{\partial t}\left(\frac{\Delta V_k}{V_k}\right)\right)^2 \qquad \text{(Equation 3.1)}$$

Where N is the number of samples and the summation runs over all the samples, b and m are respectively the base and the monitor trace, $\Delta V_k/V_k$ is the relative 4D velocity change and ω is the representative seismic wavelet.

An iterative Gauss-Newton optimization is applied in order for the solution to converge to a global minimum through a maximum of 10 realizations, the convergence is achieved generally quickly when the initial solution is close to the actual time-shift (i.e., when an initial time-shift model is used as a constraint).

The main assumptions in this equation are (Gradi *et al*. 2005): the propagation is nearly vertical which enable the inversion trace-by-trace and implies the time-shifts are only integrated along the vertical direction; the velocity varies smoothly laterally and there is no compaction. The first two encompass simplifications that are commonly assumed in several warping techniques. The third assumption is generally valid assumption for sandstone reservoirs. Nonetheless even after alignment the difference volumes, while representative of changes in the reservoir, are difficult to interpret quantitively, due to the band-limited nature of seismic data.

This warping technique is important at different stages across the different workflows. In workflow 1 the warping is used to align each pair of seismic angle stacks separately and estimates the associated time-shifts. In workflows 2 & 3 the warping technique is used to estimate a single time-shift model between the two full-stack seismic vintages, which is used to apply a full-stack time-shift correction to align the elastic models obtained through the inversion of the non-aligned monitor dataset.

3.4. Pre-stack 3D and 4D Stochastic Inversion

The stochastic inversion methodology applied on the different workflows, either 3D or 4D inversion, is based on the seismic modelling of several partial-incidence angle stacks. The modelling is performed using a simplified form of an approximation to the Zoeppritz equations for the elastic isotropic medium. This formulation is used to retrieve the reflectivity coefficients as a function of the angle of incidence. The reflection coefficient series are then convolved with a representative wavelet to obtain a synthetic seismic cube which will be compared with the areal seismic data.

From this comparison requires the concept of a cost function (Equation 3.2). This function directly depends on the seismic residual which is the energy of the difference between the synthetic trace and the actual seismic trace. The goal of the inversion is then to solve for a set of elastic properties that minimize the most this objective function.

$$J = \left(\frac{S}{N}\right)^2 \sum_{\theta} \sum_{t} \left(s_{\vartheta,t} - \sigma_{\vartheta,t}\right)^2 + \sum_{c} \lambda_c^2 \sum_{e} \sum_{l} \left\| m_{e,l} \right\|_c^2 \qquad \text{(Equation 3.2)}$$

Where S/N is signal to noise ratio; θ the angle stack; t the time samples; $s_{\vartheta,t}$ the seismic sample at angle θ and sample t; $\sigma_{\vartheta,t}$ the synthetic sample at angle θ and sample t, c the c_{th} constraint and || || its associated norm; λc the weight associated with c_{th} constraint; e the eth elastic parameter (i.e., Vp, Vs, ρ); l the l_{th} layer; and mp,l the value of the reduced, normalized parameter p at layer l.

This inversion approach uses a low frequency model, lateral correlations and a set of constraints which sets the inverse problem to find the models that best matches the seismic data while honoring the imposed constrains. The inversion tool generates several realizations of the elastic properties by modifying the sequential Gaussian simulation path and exploring a range of possible parameters.

The inversion solves for the value of the elastic parameter of choice at each trace position an at each layer specified in the hybrid grid. In order to ensure consistency along layers, the inversion process applies a sequential Gaussian simulation (SGS) algorithm, based on a geostatistical approach.

The SGS algorithm can be summarized by the following steps as described in Soares (2001):

i. Estimation at point x_n, randomly located in area A to be simulated considering the mean and conditional variance of the conditioning data. Following a p value is generated from a uniform distribution between 0 and 1.

The Gaussian value $Y_s\,(x_n)$ is obtained from the inverse function of the local Gaussian cumulative distribution:

$$Y_s(x_n) = G^{-1}([Y(x_n)^*; var[Y(x_n)]^*; p)$$

$Y_s\,(x_n)$ becomes part of the conditioning values $\{n+1\} = \{n\} + \{Y_s\,(x_n)\}$

ii. The same process of i. and ii. is repeated for another point x_{n+1}, randomly chosen within area A, for which the mean and conditional variances are estimated based on the $(n+1)$ conditioning values $\{n+2\} = \{n+1\} \cup \{Y_s + 1\,(x_n + 1)\}$. This sequence is repeated until the last $Y_s(x_N)$ value of within area A is simulated based on the $(n+N-1)$ conditioning values.

iii. The simulated Gaussian map $Y_s(x)$ is subsequently transformed into $the\ Z_s(x)$ values by the inverse transform:

$$Z_s = \varphi^{-1}[Y_s(x)]$$

For all the inversions, except for the baseline inversion in workflow 3, the initial models and correspondent standard deviations are set to a constant value (i.e., it is assumed that the LFM is the same for the two surveys). Accordingly, each inversion (either 3D or 4D) is parameterized with 3 random seeds (i.e., number of starting traces) and a constant 10% noise to signal ratio which is used to define how much the seismic data should match the synthetic seismic.

3.5. Generating a PEM Constraint

A petroelastic model (PEM) is a set of parameters and equations which relates the reservoir properties, such as pore volume, pore fluid, fluid saturation, reservoir pressures and rock composition to seismic elastic properties, such as P-wave velocity, S-wave velocity and density (Figure 3.3). Thore and Blanchard (2015) developed these PEM constraints based on available rock-physics models to guide the elastic inversion results to more realistic combinations of elastic properties, providing only amplitude ratios between parameters and not the absolute amplitudes.

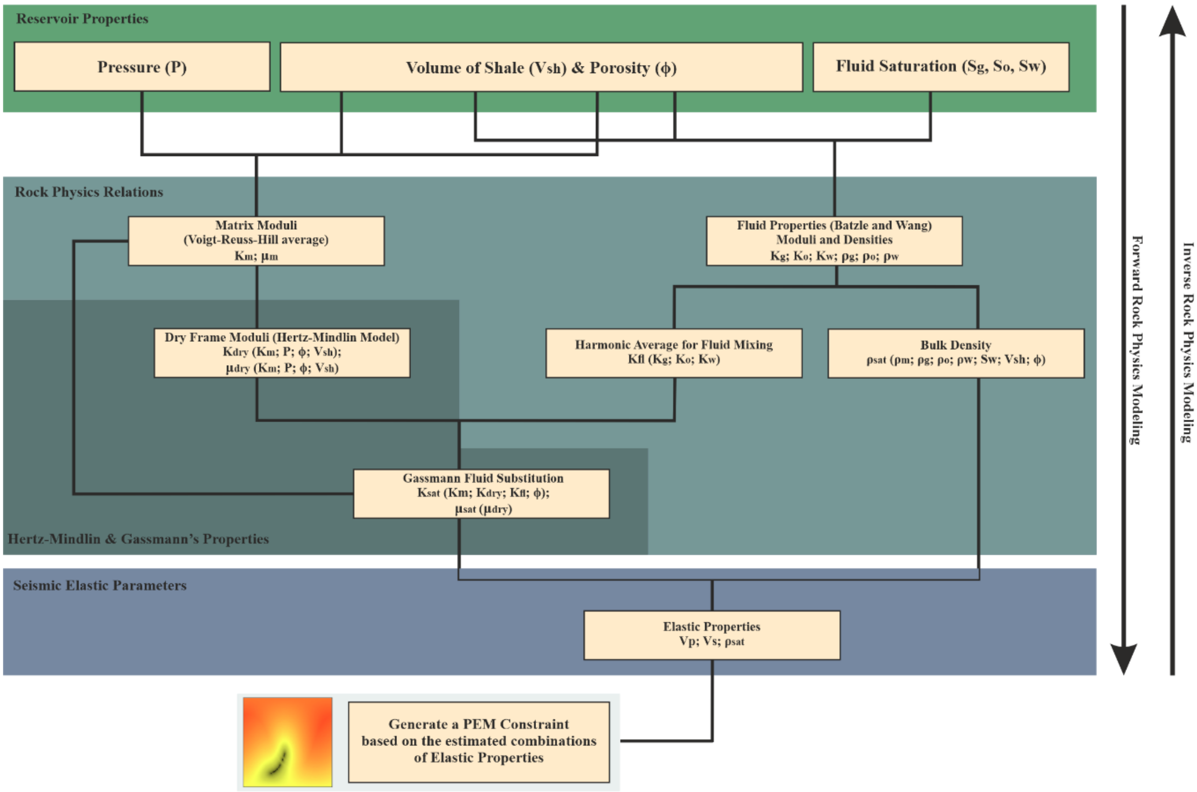

Figure 3.3 - Illustration of the relations of the rock physics models and seismic elastic properties (adapted from: Yanez, 2017). Generation of a petroelastic model constraint based on prior geological and production knowledge.

The 4D constraint is generated based on synthetic elastic responses in terms of change in P- and S-wave velocity and density for each possible value of porosity and shale content that are computed for a designated production scenario based on the reservoir production mechanism in place (water injection). The 3D constraint is generated based on the domain of possible synthetic combinations of P- and S-wave velocities and density that are computed by sampling the static well-log data available at the wells (volume of clay, porosity, fluid saturation, pore pressure and depth of burial).

The basic idea of implementing these constraints is to penalize results that are “far” from the prior synthetic data sampled by the petroelastic model (black dots on constraint maps). The resulting PEM constrained elastic models should be characterized by a higher compatibility with the prior geological information when compared with the models obtained without imposing any PEM constraint. These constraints are classified as being 4D constraints when based on modelled elastic responses expected in a water replacing oil scenario and 3D constraints that are based on known combination of P- and S-wave velocities and density (as schematically illustrated in Figure 3.4).

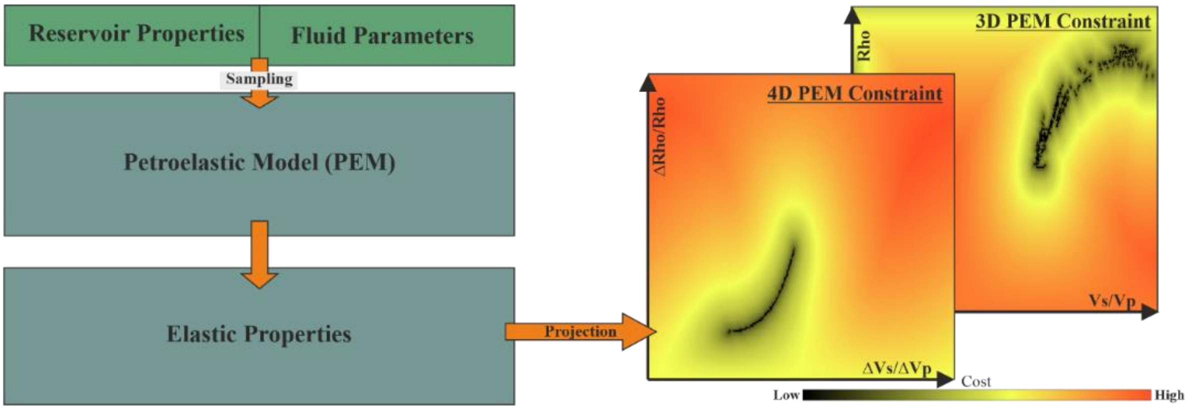

Figure 3.4 - Simplified representation of how PEM constraint is generated and visualized. These constraint maps represent the cost associated with the results (the black dots correspond to the predicted values by the PEM).

3.6. 4D Inversion Workflows

3.6.1. Workflow 1: Inversion of the Differences

The present workflow follows a classical approach in which the 4D amplitudes differences between repeated seismic surveys are inverted to obtain a set of elastic time-lapse models. This technique encompasses three main stages that are schematically illustrated in Figure 3.5.

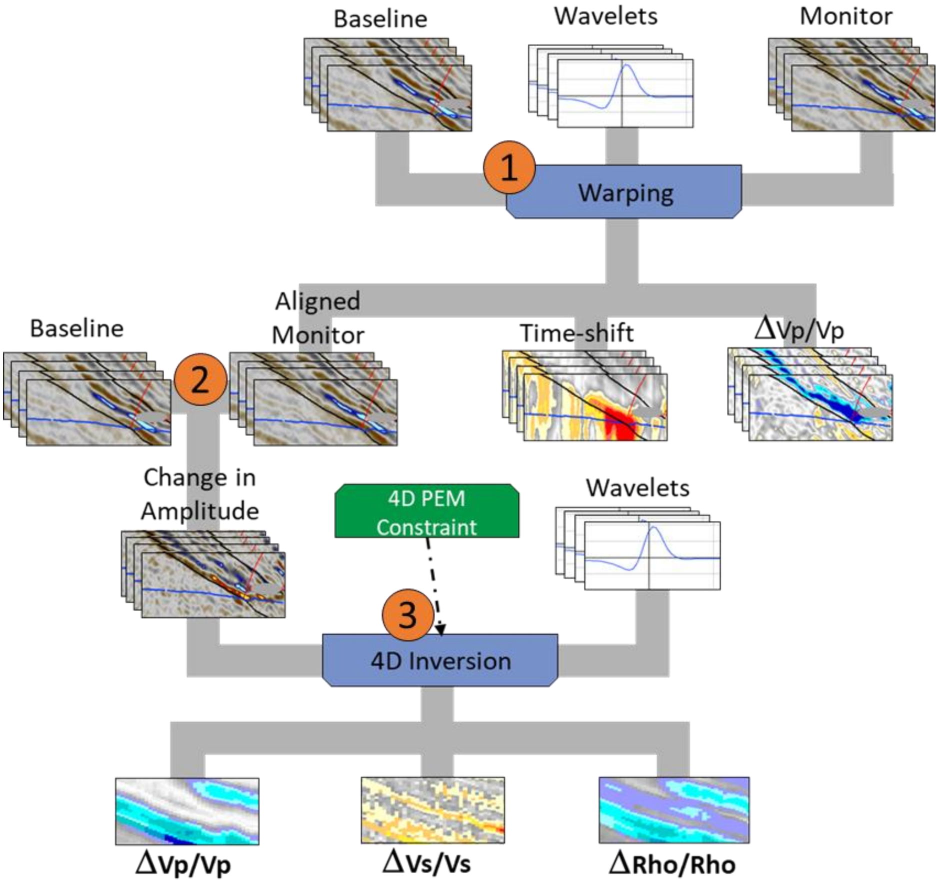

Figure 3.5 - Workflow 1: Detailed schematic representation step-by-step of the 4D inversion methodology proposed for the inversion of the amplitude differences.

This 4D inversion technique can be summarized by the following steps:

1. For each angle stack - Angle domain estimation of the time-shifts between vintages (separately for each stack) and application of a time-shift correction to the monitoring partial stacks which time-aligns them to the relative reference angle stack selected from the pre-production data.
2. Computing the differences between the vintages by subtracting of the baseline angle stacks from the aligned monitor angle stacks to acquire the corresponding relative change in amplitude.
3. Pre-stack inversion of the amplitude differences using a 4D stochastic inversion algorithm that includes a 4D PEM constraint to obtain a set of 4D elastic models ($\Delta Vp/Vp$, $\Delta Vs/Vs$ and $\Delta\rho/\rho$).

3.6.2. Workflow 2: Uncoupled Inversion

This 4D inversion technique is inherently different from the classical procedure, comprising the independent inversion of individual baseline and monitor vintages to elastic models which are then differentiated to obtain the time-lapse elastic models. This technique encompasses three main stages that are schematically illustrated in Figure 3.6.

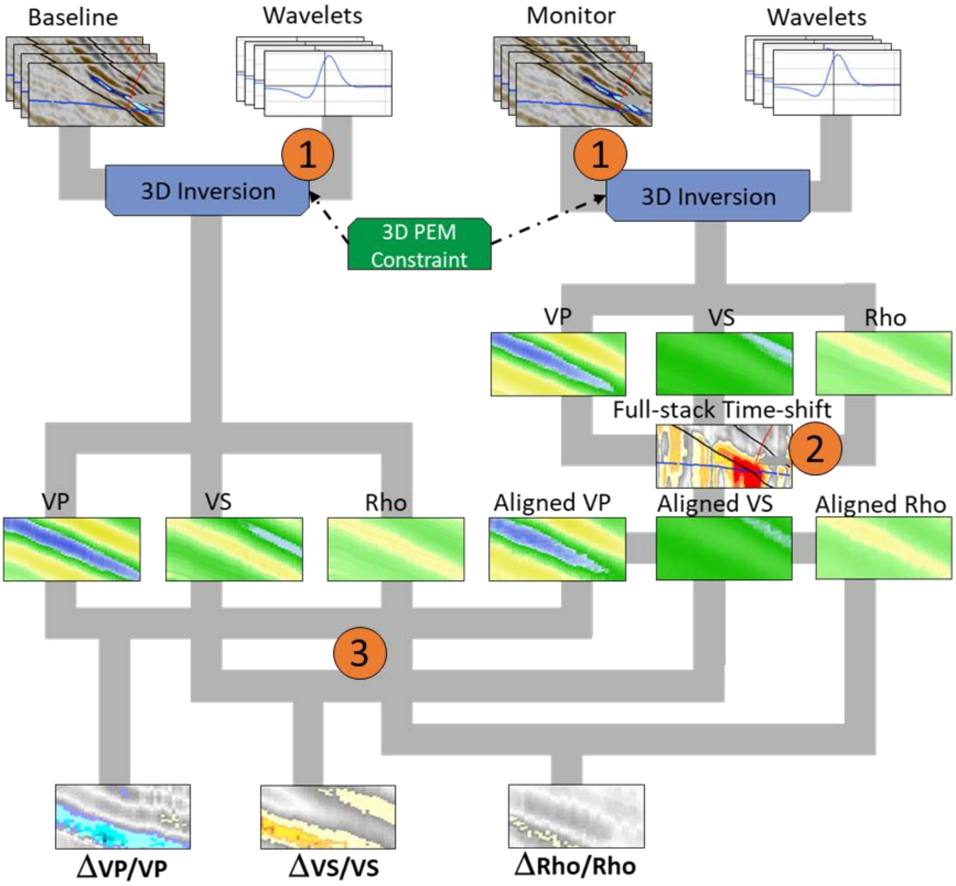

Figure 3.6 - Workflow 2: Detailed schematic representation step-by-step of the 4D inversion methodology proposed for the uncoupled inversion.

This 4D inversion technique can be summarized by the following steps:

1. A dedicated 3D prestack seismic inversion is conducted for each seismic vintage (baseline and monitor) using the pre-conditioned angle stacks and respective wavelets. Both stochastic inversions include a 3D PEM constraint and result in a set of absolute elastic models (Vp, Vs and ρ) for each dataset.
2. The monitor elastic models are then time aligned to the baseline reference using a full-stack time-shift model that was estimated between the full-stack seismic volumes.
3. The time-lapse elastic models (ΔVp/Vp, ΔVs/Vs and Δρ/ρ) are acquired by computing the differences between the baseline elastic models from the corresponding aligned monitor elastic models.

3.6.3. Workflow 3: Coupled Inversion

For this time-lapse inversion technique each seismic vintage is individually inverted, however not totally independently from one another given that the monitor dataset is inverted to obtain a set of elastic models, which are subsequently used as the initial models in the inversion of the baseline dataset. This technique follows a sequential arrangement that encompasses four main stages that are schematically illustrated in Figure 3.7.

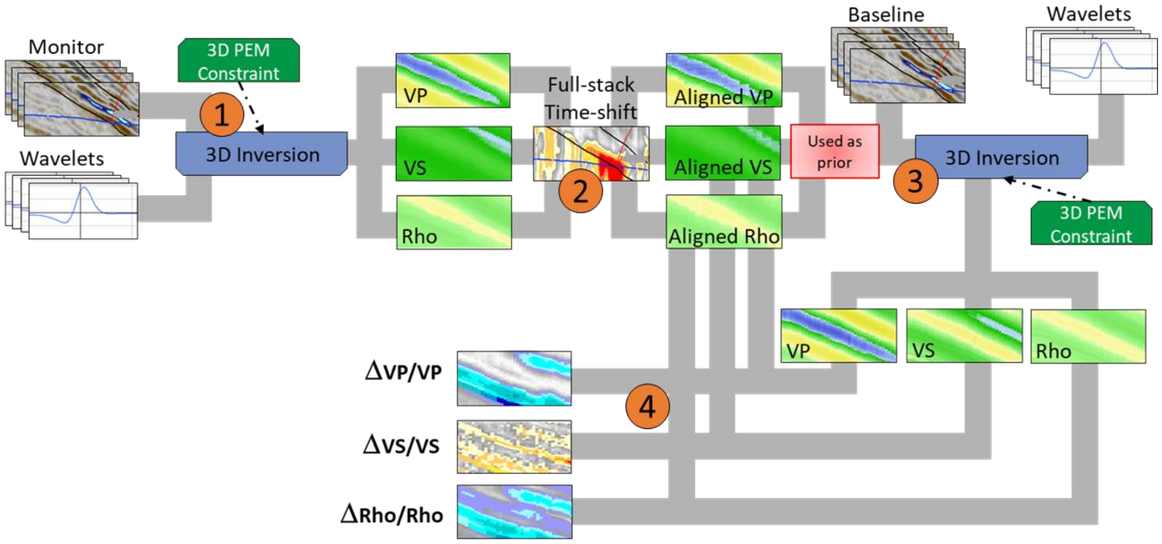

Figure 3.7 – Workflow 3: Detailed schematic representation step-by-step of the 4D inversion methodology proposed for the coupled inversion.

This 4D inversion technique can be summarized by the following steps:

1. Dedicated 3D prestack seismic inversion of the monitor seismic vintage, including a 3D PEM constraint and resulting in a set of absolute elastic models (Vp, Vs and ρ).
2. The monitor elastic models are then time aligned to the baseline reference using a full-stack time-shift model that was estimated between the full-stack seismic volumes.
3. Connecting both stochastic inversions by using the aligned monitor elastic models as prior models in the baseline dedicated 3D prestack seismic inversion constrained to a 3D PEM.
4. The time-lapse elastic models (ΔVp/Vp, ΔVs/Vs and Δρ/ρ) are acquired by computing the differences between the baseline elastic models (that are now dependent on the monitor) from the corresponding aligned monitor elastic models.

4. Case Study: Results and Discussion

4.1. Data Description

The available seismic data used in this study consist of two repeated seismic surveys: one acquired during a pre-production stage (baseline) and another acquired after 6 years of hydrocarbon production (monitor). Both surveys cover the same area (about 430 km^2) with a seismic sampling interval of 3 ms and were acquired and processed following a particular workflow to ensure the optimal repeatability of the 4D signal, with NRMS values between 15-20%.

Each seismic dataset is composed by a set of full-stack volumes and four angle sub-stacks, comprising the following partial stacks 4-12° (near stack), 12-20° (mid stack), 20-28° (far stack), and 28-37° (ultra-far stack), typical vertical sections of the seismic data are shown in Figure 4.1. The data and results shown further correspond only to a specific seismic section for all the data volumes and workflows.

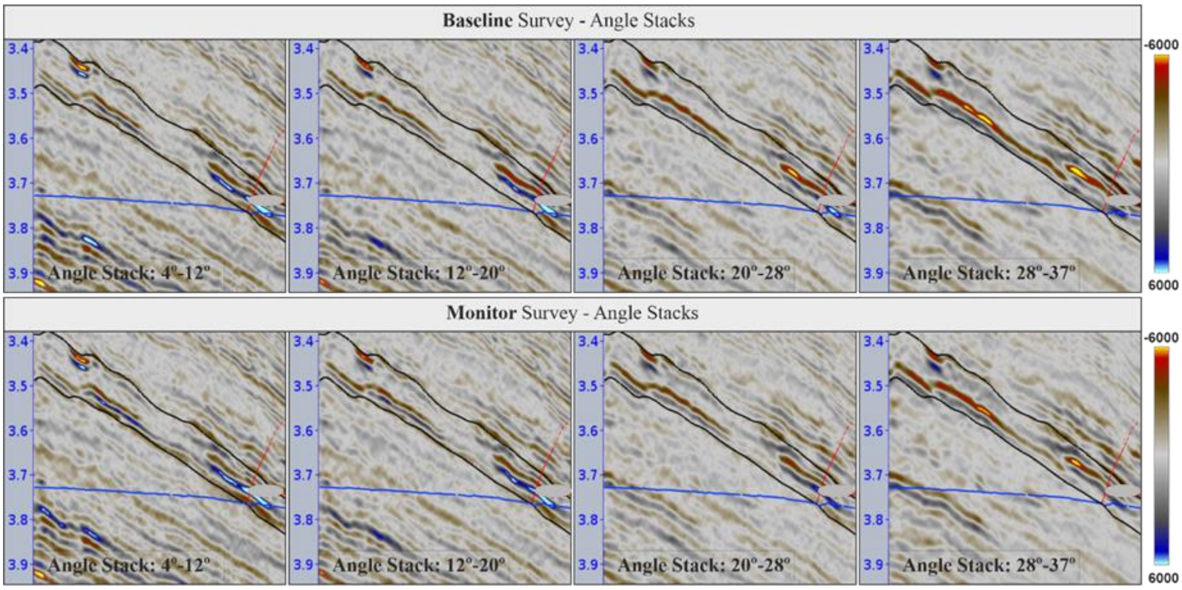

Figure 4.1 - The seismic data used for this study consists of four time-migrated angle stacks ([4°-12°], [12°-20°], [20°-28°] and [28°-37°]) and a set of full-stack volumes [0°-35°] acquired in 1998 (top row), before starting production, and in 2015 (bottom row), after 6 years of reservoir production.

The reservoir interval that this study focus on has a set of 10 wells, from which four are water injection wells (I1 – I4) and the remaining six are producer wells (P1 – P6), drilled during the field development stage. Most of these wells follow slightly deviated trajectories across the reservoir interval. Among the available range of wireline logs there is a set of petrophysical logs comprising the volume of clay, porosity and water saturation accessible for most of the wells and a set of petroelastic logs composed by P-wave and S-wave velocities and density logs available for only several wells. From all available wells in this study, herein are presented the well-logs for producer well 3 as illustrated in Figure 4.2.

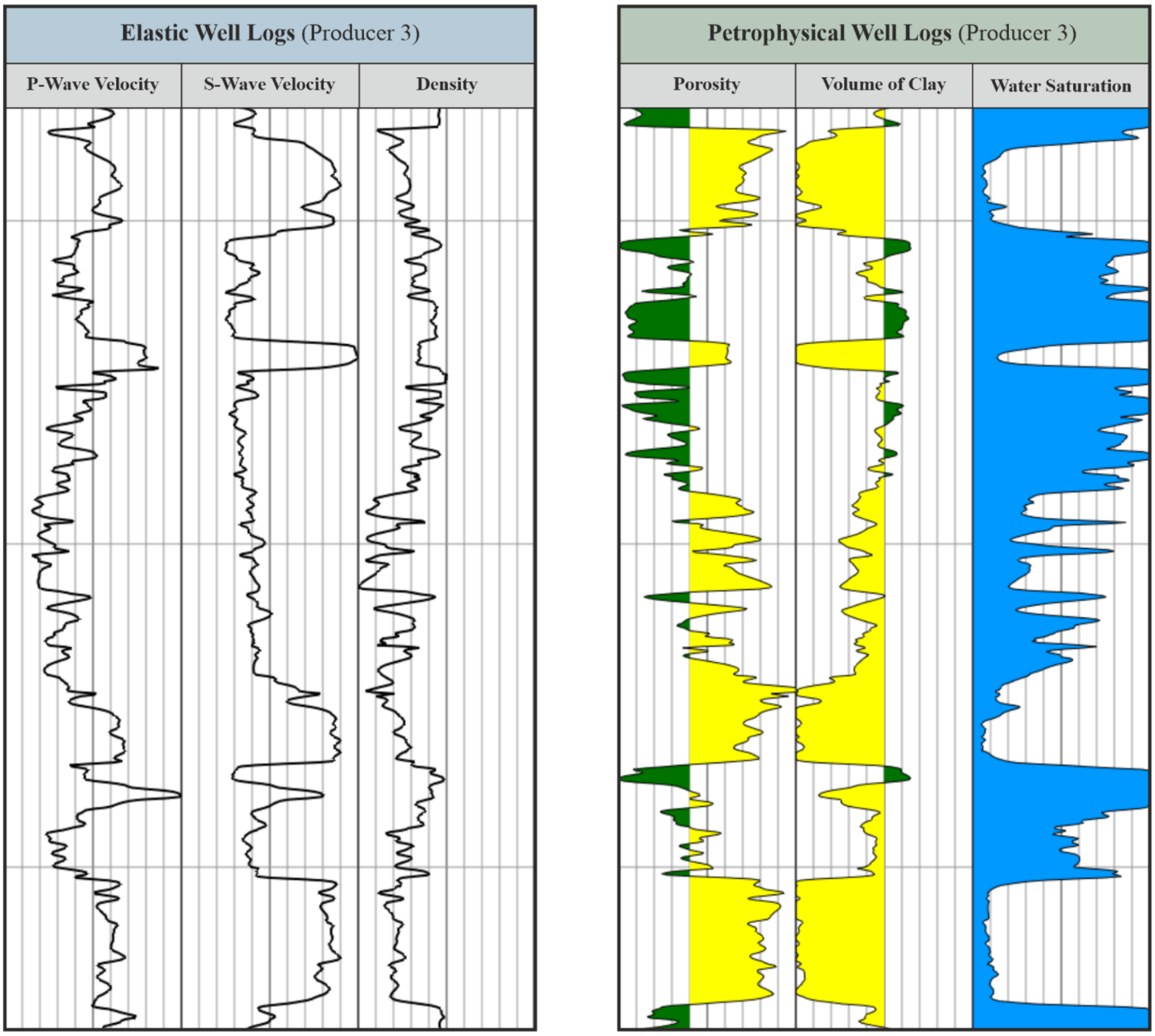

Figure 4.2 - Example of well-logs for a producer well, comprising a set of elastic logs (right track) for P-wave and S-wave velocity and density mainly used to estimated wavelets. The track on the left comprises the petrophysical logs for porosity, volume of clay and water saturation that sample the reservoir properties and are mainly used to generate PEM constraints.

These set of well-log data can be sub-divided in two groups with separate purposes within the scope of this project further from the inherent valuable information that can be used for qualitative and quantitative formation evaluation. The set of elastic logs (P-wave, S-wave and density) primary purpose is to provide a framework to estimate representative wavelets at each well location. The set of petrophysical logs are used to compute the expected elastic responses to provide a framework to generate PEM constraint used as a constraint in the seismic inversions.

For each sub-stack and seismic survey, a set of representative wavelets were estimated using seismic and well-log data. Due to the survey-to-survey matching, including frequency-dependent amplitude content, the same wavelet was used for each specific angle range across the all the surveys. The corresponding angle dependent wavelets and a summary of their principal characteristics is shown in Figure 4.3.

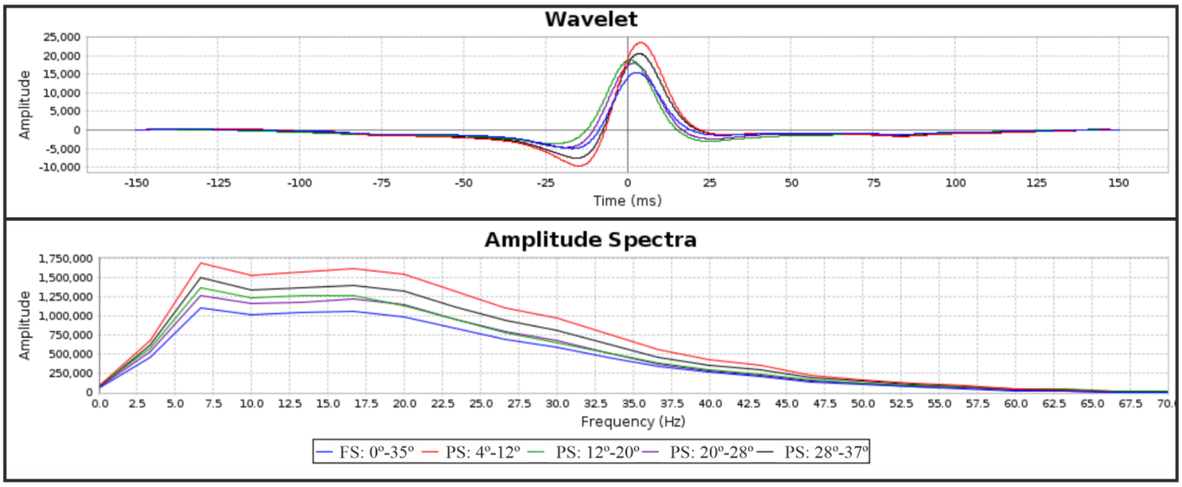

Figure 4.3 - Set of representative wavelets for the baseline dataset used for seismic warping and stochastic inversion ([4°-12°], [12°-20°], [20°-28°] and [28°-37°]) and full-stack volumes [0°-35°] and respective amplitude contents.

Starting from a flow simulation model with 254x246x65 cells in i, j and k directions constructed based on a global interpretation of horizons and faults and the position of the architectural elements identified on the seismic data. The simulation grid is used to generate a hybrid grid that is going to be used as the inversion grid and to store the results, as described in the methodology chapter 3.2. The hybrid grid (Figure 4.4) was created based on the reservoir grid geometry of 65 layers (in time-domain) adding a additional layering of 70 layers above and below the reservoir, making a total of 205 layers, in order to cover the amplitude anomalies of seismic data.

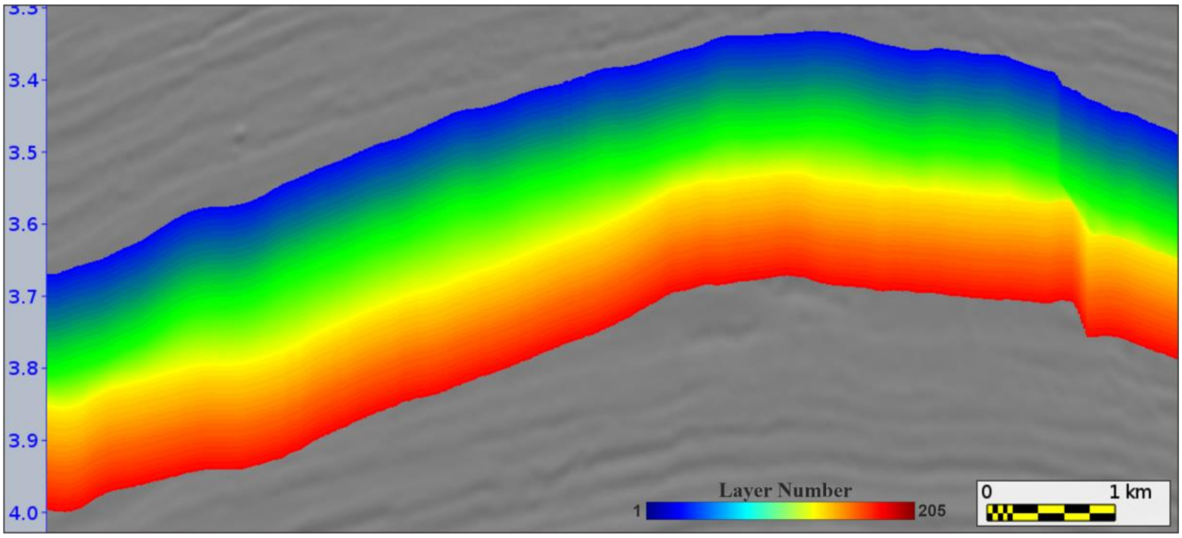

Figure 4.4 - Seismic inversion grid (HG) displayed by rainbow colors which represent the horizontal layering that honor the reservoir simulation grid layering.

4.2. Workflow 1: Inversion of the Differences

This workflow is the most traditional one, which uses 4D amplitude differences between repeated seismic datasets to invert for the relative change in the reservoir elastic properties due to production. This time-lapse inversion technique requires a comprehensive data preparation before obtaining the changes in amplitude used in the inversion. This sub-chapter aims at assessing and presenting the optimal choices in parameterization.

The first stage comprises the monitoring survey time-alignment to the baseline reference survey. This first step relies on the usage of an initial time-shift model, estimated separately using a set of full-stack seismic volumes as a key parameter to constraint the monitor alignment. In order to demonstrate the effect of this constraint, Figure 4.5 shows the comparison between the estimated time-shifts for each angle stack obtained when warping the vintages without using any constraint (top row) and using the initial time-shift model as a constraint (bottom row).

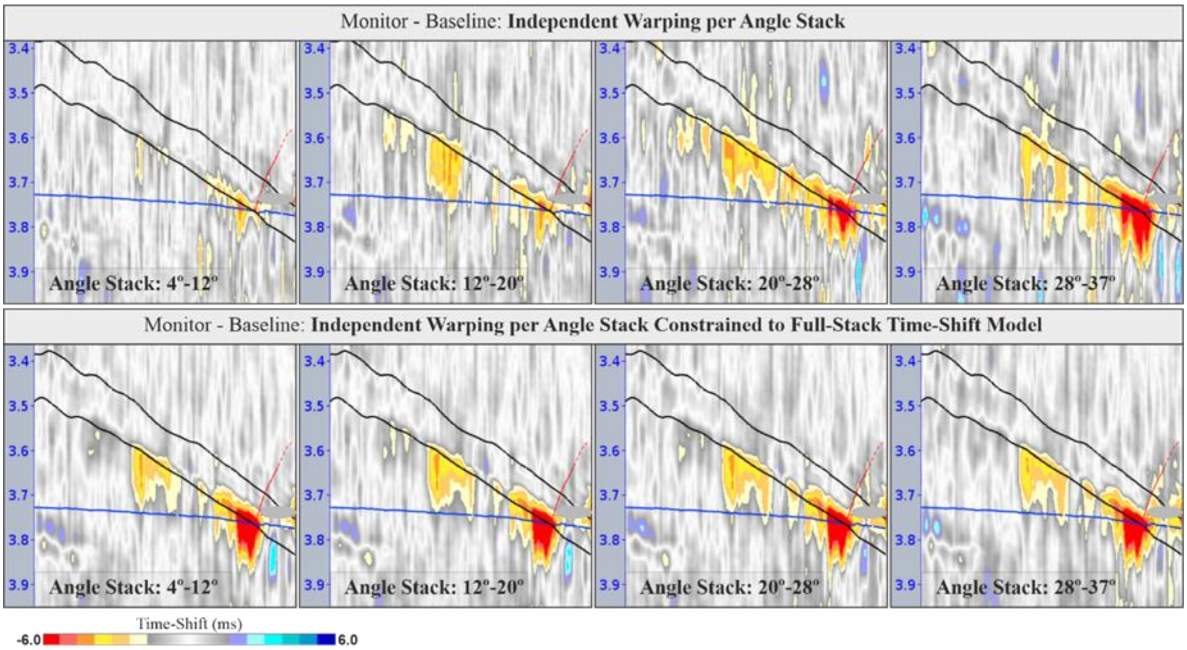

Figure 4.5 - Visual comparison between the time-shifts estimated for each angle stack without using an initial time-shift models as a constraint (top row) and using an initial time-shift model as a constraint (bottom row).

It is noticeable that without using an initial time-shift model as constraint, the resulting time-shifts estimated for each angle stack vary considerably, showing an overall increasing trend from the near to the far offsets and higher noise content. Oppositely using an initial time-shift model to constraint the warping causes the estimated time-shifts for each of partial stack to become more consistent across the different angle stacks showing small variability. This constraint provides a reliable way to reduce the misalignment between the near and far angle stacks which consequently improves the quality of the time-lapse elastic inversion.

The warping process uses these estimated time-shifts to align the monitor dataset to the reference baseline survey. After time-aligned the baseline seismic volumes can be subtracted from the aligned (warped) monitor seismic volumes resulting in the relative change in amplitude between the two repeated surveys as shown in Figure 4.6.

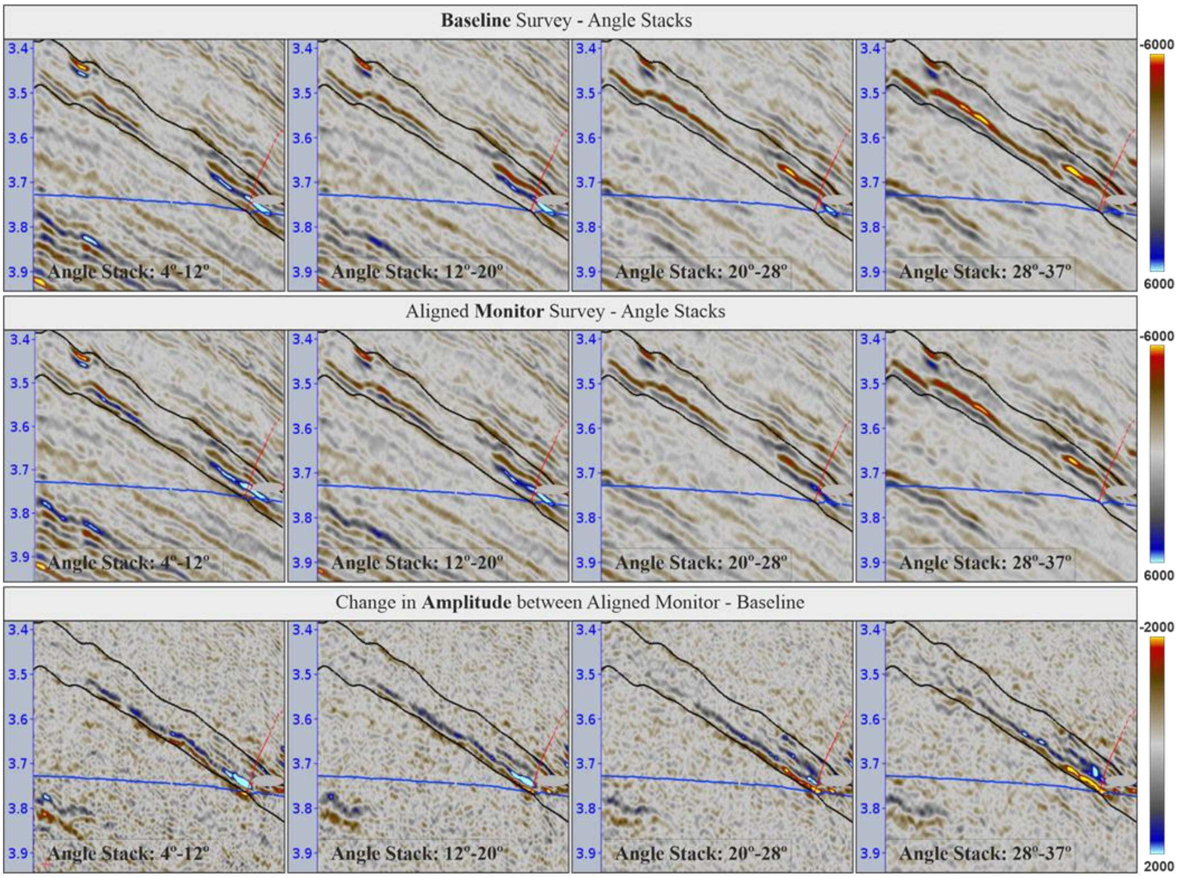

Figure 4.6 - Vertical seismic sections drawn across the baseline survey partial angle stack volumes (top row), the warped monitoring survey partial angle stack volumes (middle row). Amplitude differences between seismic vintages (bottom row).

The aligned monitor seismic sections seem to be correctly aligned since the main reflector appear to be slightly displaced upward in comparison with the baseline seismic sections. Visually the amplitude differences between the vintages are almost undetectable before subtracting the volumes. Even though the variability between the estimated time-shifts becomes smaller when using the initial time-shift model constraint, the results obtained for the relative change in amplitude still shows significant variability between the different angle stacks (i.e., the change in amplitude tends to decrease from the near to the far offsets), therefore preserving the angle dependency that one takes advantage of in pre-stack seismic inversion.

The next stage in this workflow uses the relative change in amplitude obtained previously as the input in the 4D elastic inversion scheme to estimate the relative change in the reservoir elastic properties (Vp, Vs and density). This inversion step capitalizes on the implementation of a 4D PEM constraint to highly improve the compatibility with the prior geological knowledge.

There is a further parameter that this workflow relies on, which is the minimum distance from the origin, being the origin point assigned to the "no anomaly point" where the change in elastic properties is null. This parameter defines a threshold on how significant a 4D anomaly must be in order for the 4D PEM constraint to be applied on it. Three different distances from the origin were tested to evaluate the effect when applying the 4D PEM constraint to significant anomalies higher than 1%, 2% and 3%. A brief comparison of the results obtained is shown in Figure 4.7 which intends to demonstrate the impact that this parameter has in the time-lapse inversion.

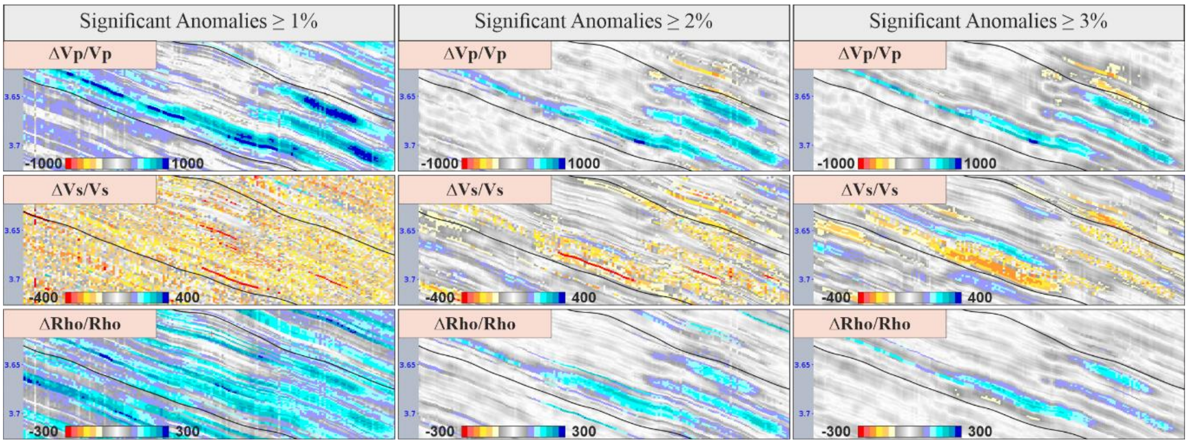

Figure 4.7 - Visual comparison between the effect of using different distances to origin thresholds in the 4D stochastic inversion highlighting the impact on the estimated change in elastic properties.

From the analysis of the results obtained across all the estimated elastic properties using different thresholds it is most noticeable that if the minimum distance from the origin is 1% (left column) the inversion is extended to locations where no 4D signal is expected. On the other end when the threshold used is 3% (right column) the 4D PEM constraint does now cover all points where time-lapse signal is expected, resulting in relatively smaller and less continuous anomalies. Therefore, to ensure one does not underestimate neither overestimate the extent of the signal the optimal threshold to be used should be 2% (center column).

Figure 4.8 intends to demonstrate and evaluate the implications of adding prior geological information and dynamic data through a 4D petroelastic model constraint by means of comparing coherency between the inverted elastic parameters without constraining the inversion (left column) and constraining the inversion to a 4D PEM (right column).

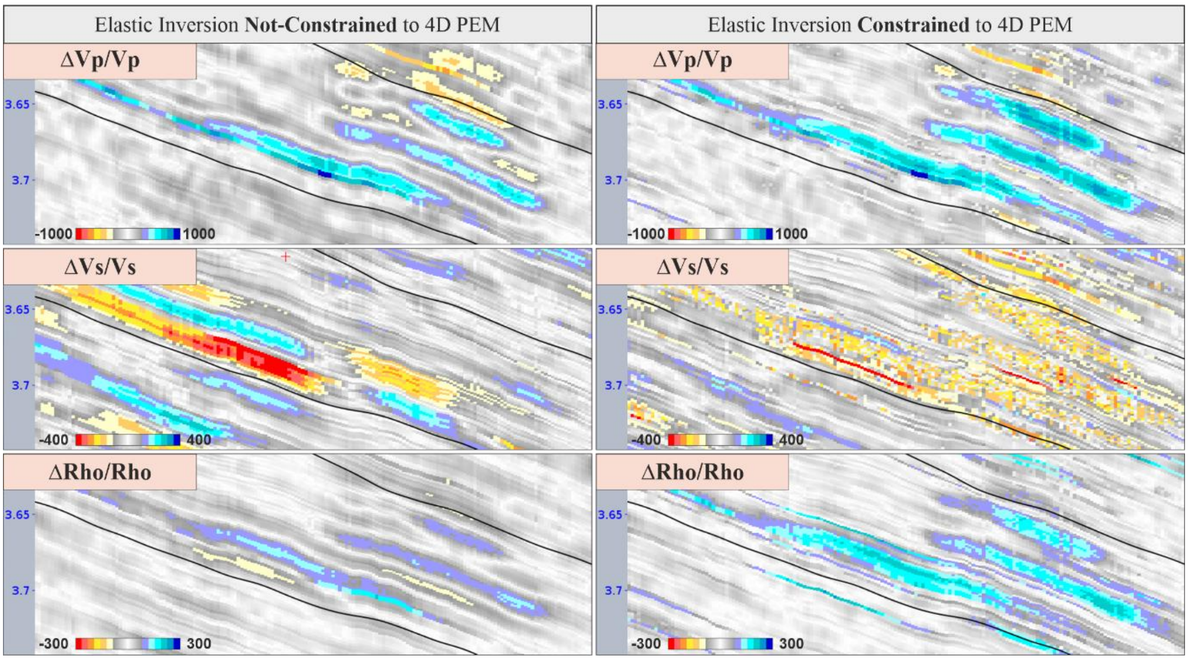

Figure 4.8 - Relative change in elastic properties obtained without using a 4D PEM constraint in the 4D stochastic inversion drawn across a one realization volume (left column). Relative change in elastic properties obtained using a 4D PEM constraint in the 4D stochastic inversion drawn across a one realization volume (right column).

The estimated elastic properties obtained without imposing a 4D PEM constraint show inconsistencies when mutually compared, for example, the regions with positive P-wave velocity changes should correspond to the regions with negative changes in S-wave velocity as well as there should be a high positive correlation between the changes in P-wave velocity and density. In contrast when the inversion is constrained to the 4D PEM it is immediately noticeable that there is a high inversion correlation between the changes in P- and S-wave velocities and a high positive correlation between the changes in P-wave velocity and density that honors the modelled 4D PEM predictions.

The concluding results regarding the variation of elastic parameters are shown in Figure 4.9 across an inline section which corresponds to water flooding from an injection well to a production well scenario. Corresponding to this dynamic mechanism, it is expected a positive variation in P-wave velocity and density and a negative variation for S-wave velocity (due to the increase in the density of the fluid). This workflow is able to resolve three 4D anomalies corresponding to separated water flooding fronts showing a good coherent correlation between the estimated parameters: the regions with positive changes in P-wave velocity match the regions with a negative changes in S-wave velocity and the regions with positive changes in density.

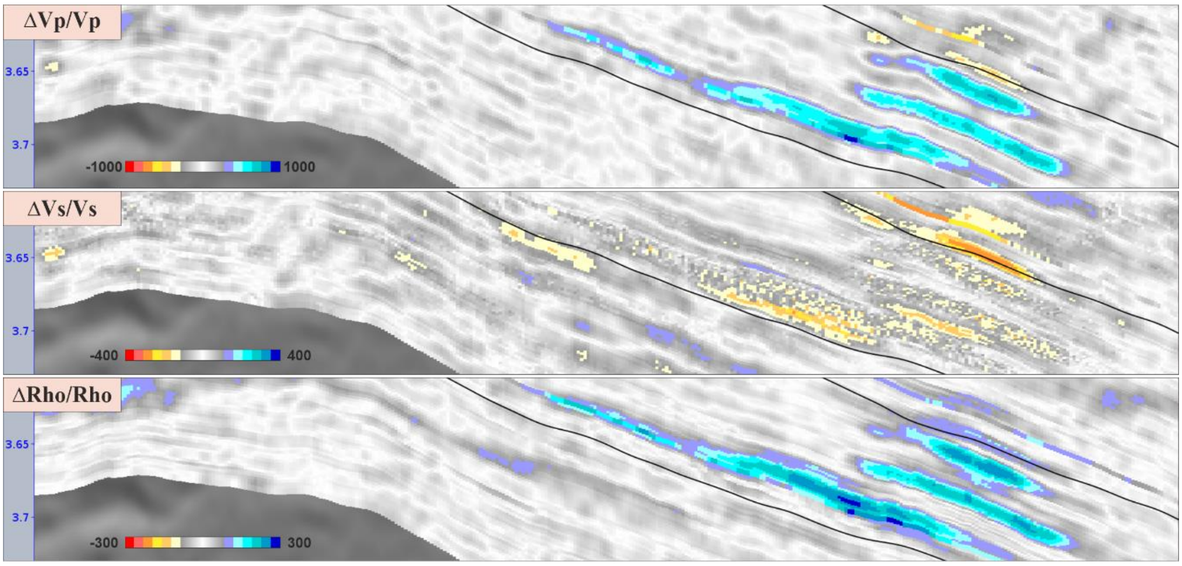

Figure 4.9 - Seismic sections drawn across the mean of 20 realization models, showing the change in elastic properties following workflow 1. Change in P-wave velocity (top section), S-wave velocity (middle section) and density (bottom section).

Furthermore, it is important to note that these sections are drawn across the 3D volume corresponding to the mean of 20 realizations which ultimately enhances the results through efficiently attenuating the random noise associated to each realization and generally improving the lateral continuity.

In a way to verify the compliance of the estimated elastic properties with the modelled 4D PEM response the time-lapse inversion results can be plotted in a 4D PEM constraint map, as shown in Figure 4.10. These maps represent the cost associated with the inversion results (black dots corresponding to the values modelled by the PEM). The inverted elastic properties are later transformed to the constrained space and plotted as a set of scatter points and colored according to their location in the two-way travel time.

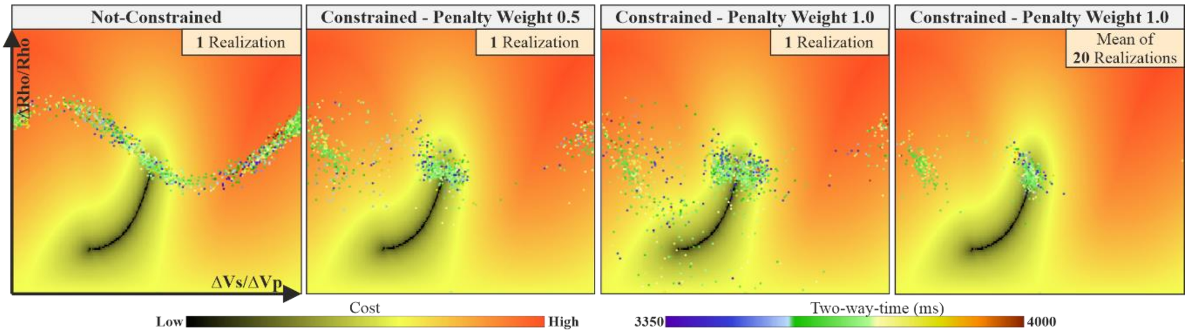

Figure 4.10 **-** 4D PEM constraint cost maps. Assessing workflow 1 elastic properties compatibility with the petroelastic model.

Initially, without imposing the 4D PEM constraint (map 1), it is perceivable a natural correlation between the elastic properties expressed high values of Δρ/ρ associated with low values of ΔVs/Vp and by low values of Δρ/ρ associated with high values of ΔVs/Vp. As the 4D PEM constraint penalty weight is increased (map 2) this natural correlation begins to disappear as the inverted points tend to move gradually to the regions of lower cost, ultimately leading to the distribution shown in map 3. The 4D PEM compliance is further improved (lowering the overall cost) by increasing the number of realizations reducing the attenuating random noise and producing more consistent results (map 4).

The visual analysis of the mean of 20 realizations 4D PEM map depicts two main clusters of point, one located mostly on the left (cluster 1) and another located in the middle (cluster 2). The cluster 1 represents the locations with a negative change in P- and S-wave velocities which is not compliant with the modelled response (Figure 4.11). The points in cluster 2 correspond to locations with a positive change in P-wave velocity and a negative change in S-wave velocity, which can be directly correlated with the reservoir production mechanism in place (Figure 4.12).

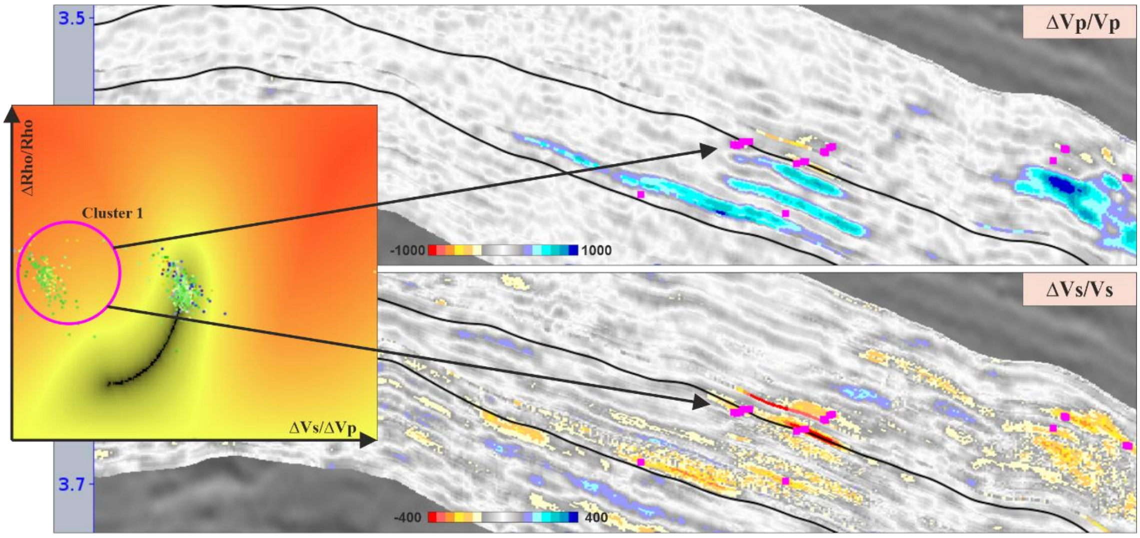

Figure 4.11 - 4D PEM constraint map highlighting the cluster of inverted points 1 and respective locations in the 4D elastic models. Representing the locations with a negative change in P-wave and S-wave velocity.

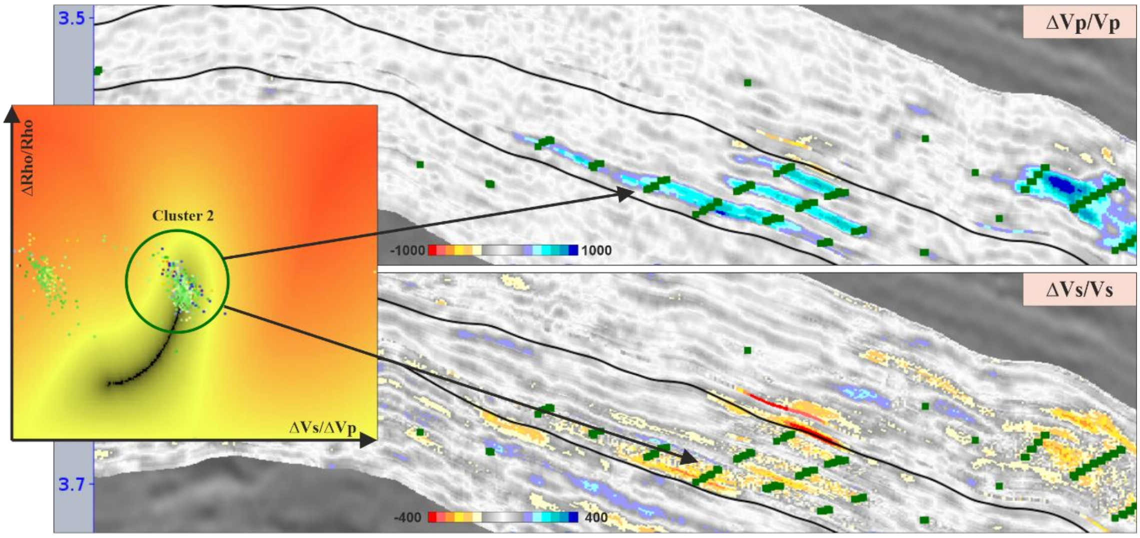

Figure 4.12 - 4D PEM constraint map highlighting the cluster of inverted points 2 and respective locations in the 4D elastic models. Representing the locations with a positive change in P-wave and a negative change in S-wave velocity.

4.3. Workflow 2: Uncoupled Inversion

The present workflow is inherently different from the previous one, basing itself on the independent inversion of each seismic vintage. The monitor elastic models are time-aligned after the inversion and before subtracting each vintage elastic models to acquire the models of relative change in elastic properties.

The early stage in this workflow comprises the separate inversion of each seismic dataset, each including a 3D PEM constraint that provides prior geological information to the elastic inversion. A brief comparison between the elastic properties (Vp, Vs and density) obtained without using any constraint (left column) and using 3D PEM constraint (right column) is shown in Figure 4.13, seeking to demonstrate the influence this constraint has in this stage in the workflow.

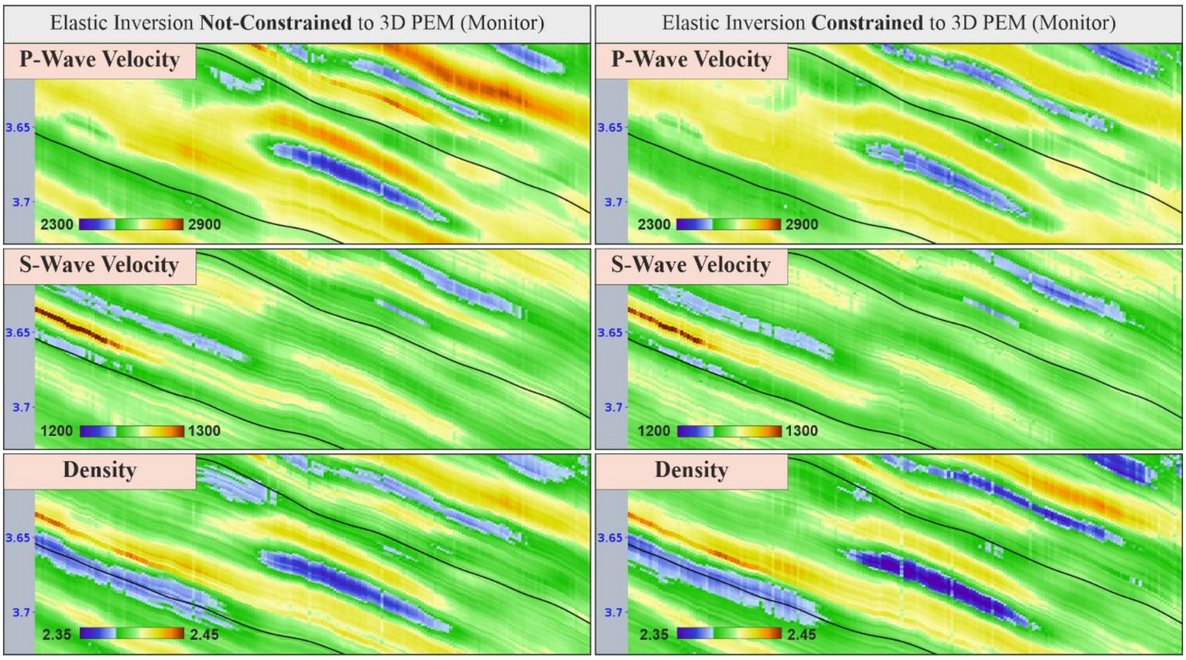

Figure 4.13 - Elastic models obtained without using a 3D PEM constraint in the 3D stochastic inversion drawn across a one realization volume (left column). Elastic models obtained using a 3D PEM constraint in the 3D stochastic inversion drawn across a one realization volume (right column).

The elastic properties obtained without imposing a petrophysical constraint lack in consistency with prior geological knowledge (extracted from well-log data). In order to overcome this challenge a 3D PEM constraint is introduced in the stochastic inversion process. This constraint aims at providing prior geological information to guide the inversion results into improving the overall consistency with the known relationships between elastic properties. Its effect is underlined in Figure 4.15 by the re-balance of the amplitude ratios between the three elastic properties (i.e., decrease in P-wave and S-wave velocity accompanied by an general increase in density).

Another way to evaluate the impact of this constraint in the inversion is to plot the elastic properties as a set of scatter points in the 3D PEM constraint map as shown in Figure 4.14. Both the baseline (top row) and the monitor (bottom row) elastic properties follow a consistent trend. The non-constrained results display an overall higher cost (plotted far from the PEM predicted trend) and as the constraint penalty weight increases the results are forced to become gradually more compliant with the 3D PEM, which is visually translated by a continuous displacement from the plotted points towards the regions with lower costs (mostly on the right cluster).

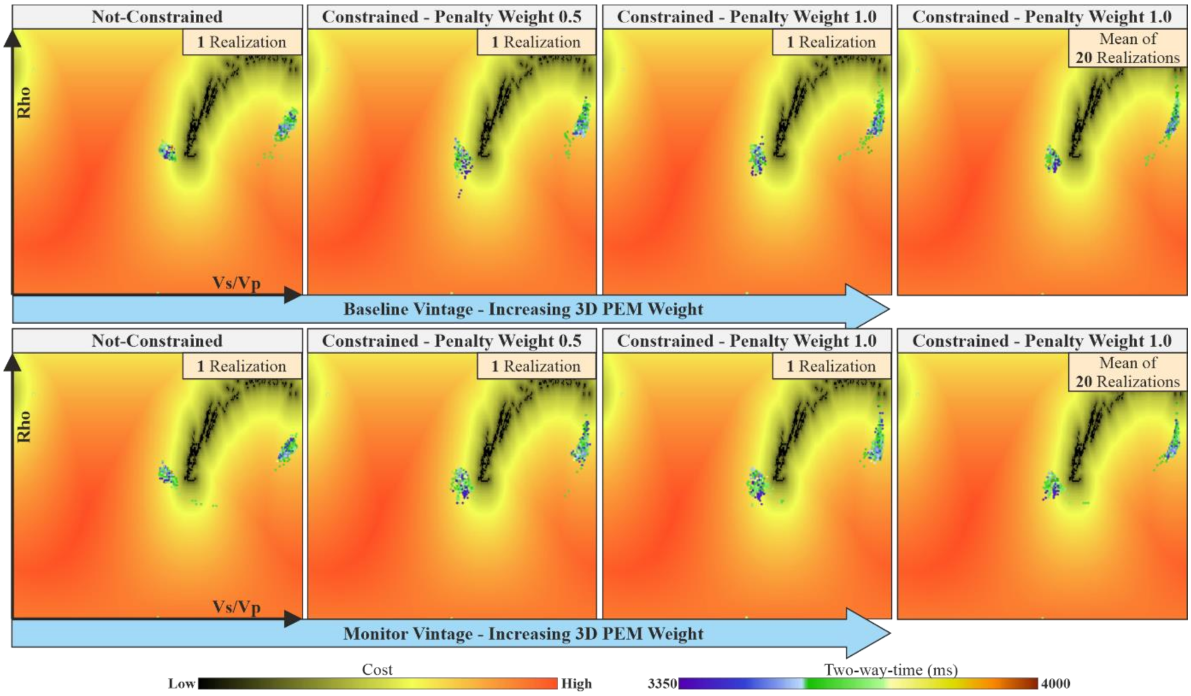

Figure 4.14 - 3D PEM constraint cost maps used in the baseline dataset (top row) and monitor dataset (bottom row) inversions. Assessing workflow 2 independently inverted elastic properties compatibility with the 3D petroelastic model.

By the end of the first stage each vintage in independently inverted generating a set of elastic models for each vintage which at this point in the workflow remain time misaligned due to change in two-way travel time between the repeated datasets. These elastic models are shown in Figure 4.15 across an inline section drawn from the mean of 20 realizations for each elastic property.

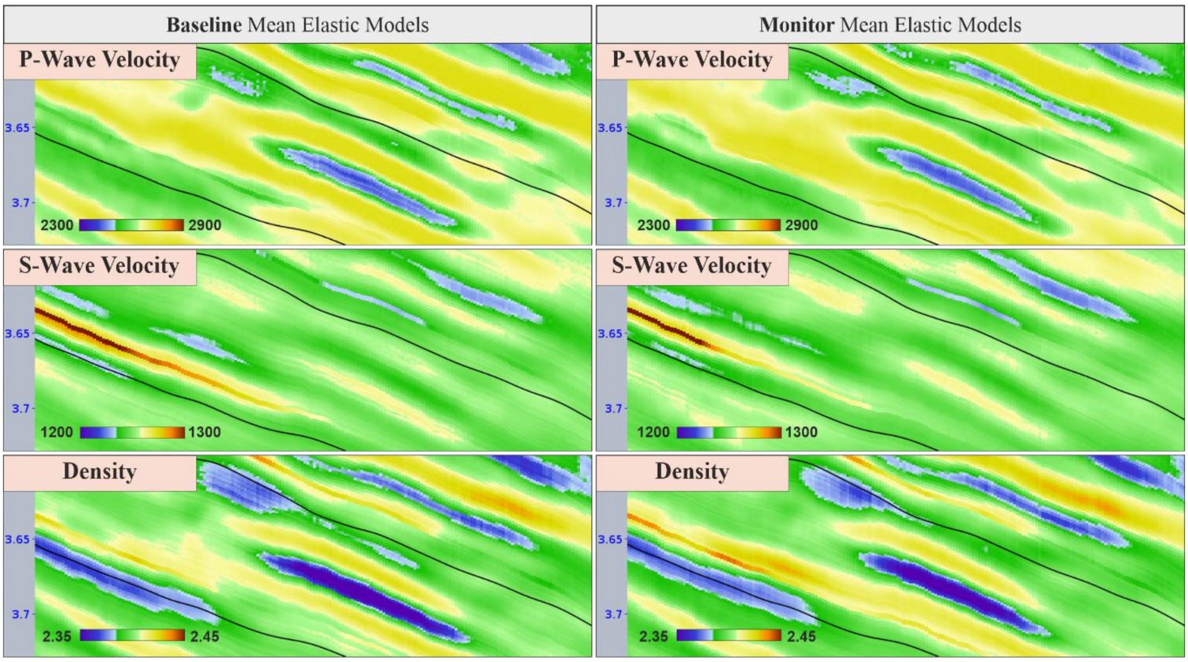

Figure 4.15 - Visual comparison between the baseline mean elastic models (left column) and the monitor mean elastic models (right row), both constrained to a 3D PEM.

These are optimized models that are obtained when the different parameters effects are properly managed, highlighting that averaging the results of 20 realizations greatly improves the lateral continuity and highly attenuates random noise. Furthermore while comparing the baseline elastic models (left column) with the monitor elastic models (right column) the most notable changes are the increase in P-wave velocity and density but also a slight decrease in S-wave velocity, these variations occur locally and are consistent with the PEM and the expected phenomena this reservoir production framework.

The following stage comprises the time alignment of the monitor elastic models to the baseline time reference. This correction is achieved by applying the time-shift model estimated between the full-stack seismic vintages to each of the monitor elastic models in order to remove the effect of the time-shifts from the data.

Figure 4.16 displays the effect of this operation has on the elastic models, exhibiting a slight coherent upward movement, in the regions with significant contrast in elastic amplitudes, ensuring the alignment correctly took place. Nonetheless this procedure introduces some level of distortion in the data (black arrow in Figure 4.16) which is evident when comparing the non-aligned (left column) with the aligned (right column) elastic models.

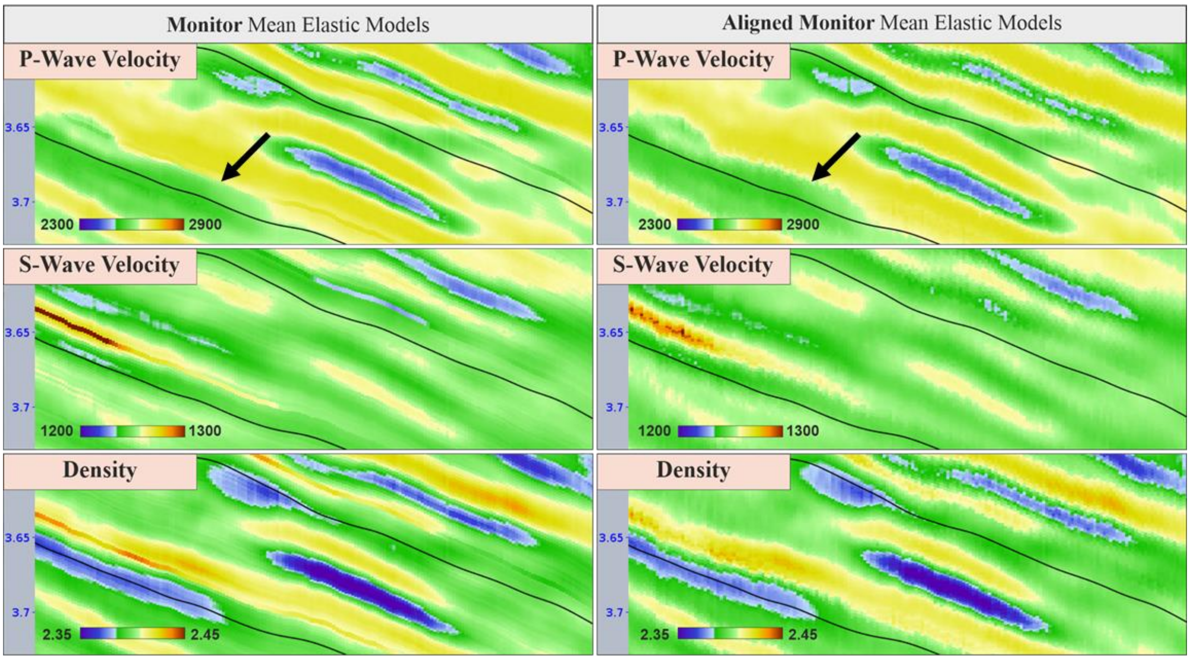

Figure 4.16 - Visual comparison between the baseline mean elastic models (left column) and the aligned monitor mean elastic models after applying a time-shift correction to remove the effect of the time-shifts from the models (right row).

Following the time-shift correction the models can be properly subtracted to retrieve the relative changes in elastic properties. In order to exhibit the benefit of properly constraint both independent inversion to a 3D PEM during the initial stage it is depicted in Figure 4.17 the comparison between the 4D elastic models obtained without imposing a 3D PEM constraint (left column) and imposing a 3D PEM constraint (right column). The main aspect that is underlined is the fact that the relation between the elastic properties becomes more coherent and there is an overall gain in continuity.

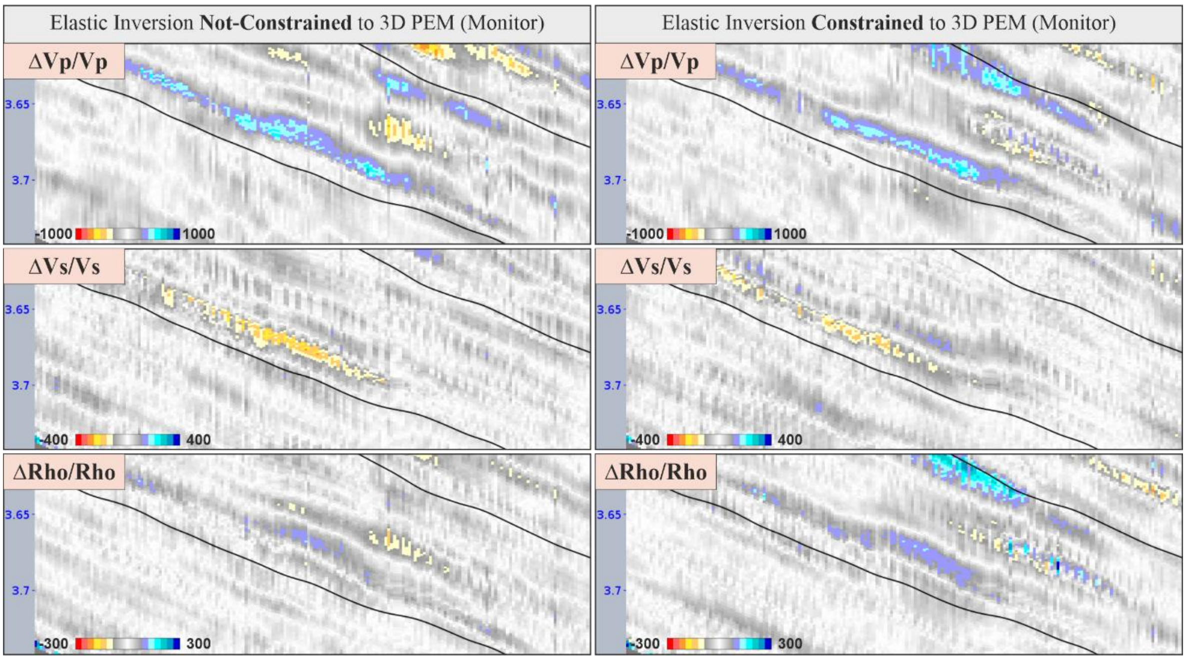

Figure 4.17 - Visual comparison between the relative change in elastic properties obtained following workflow 2 without using a 3D PEM constraint (left column) and using a 3D PEM constraint (right column).

The final results obtained by subtracting the baseline and the aligned monitor mean elastic models are shown in Figure 4.18 across an inline section which corresponds to water flooding from an injection well to a production well scenario. The estimated time-lapse elastic models obtained through this 4D inversion technique resolve fewer 4D anomalies that are generally less smooth and show fewer lateral continuity relatively to the previous workflow. Regarding the relations between the changes in elastic properties: in the relative change in P-wave velocity sections (top section) one can individualize two main positive anomalies, one of which has a clear high negative correlation with the change in S-wave velocity (middle section) and a high positive correlation with the change in density (bottom section).

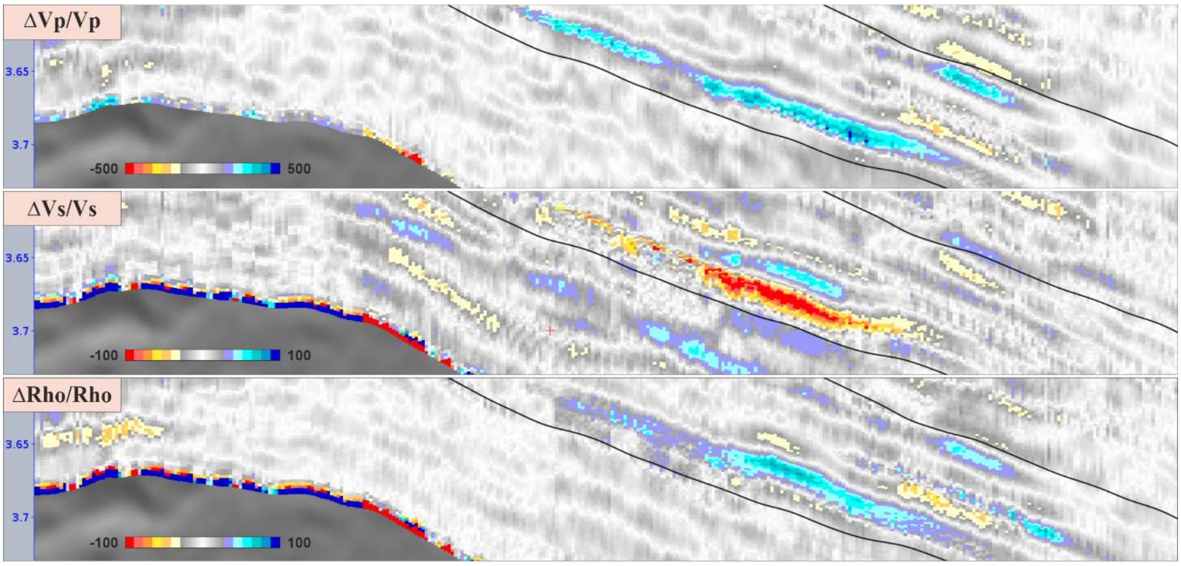

Figure 4. 18 - Seismic sections showing the change in elastic properties following workflow 2. Change in P-wave velocity (top section), S-wave velocity (middle section) and density (bottom section).

Furthermore, even though both the inversions are previously constrained to a 3D PEM the resulting time-lapse elastic models exhibit inconsistencies such as notorious positive changes in S-wave velocity and negative changes in density that are not expected within this reservoir production context. One inherent feature in this workflow is the generation of deformation artifacts at the top and base of the inversion grid that were generated during the time-shift correction step applied on the monitor elastic models and then subsequently propagated into the latter 4D models.

Despite the fact that the present workflow relies on 3D PEM constraints and not in a 4D PEM constraint the results obtained globally agree with the 4D PEM modelled response. Accordingly, in a way to verify how the 3D PEM constraints influence the compliance of the time-lapse elastic properties with modelled 4D PEM response, the uncoupled inversion results can be plotted in a 4D PEM constraint map as shown in Figure 4.19.

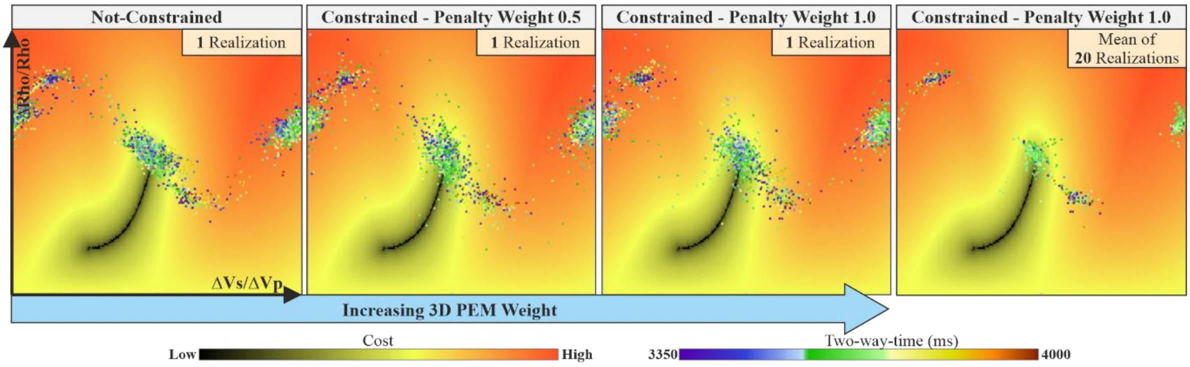

Figure 4.19 - 4D PEM constraint cost maps highlighting the workflow 2 results compatibility with the 4D modeled response. Assessing workflow 2 elastic properties compliance with the petroelastic model.

Once more, as in workflow 1, without using a PEM constraint there is a natural correlation between elastic properties expressed by high values of Δρ/ρ associated to low values of ΔVs/Vp and by low values of Δρ/ρ and high values of ΔVs/Vp (map 1). The elastic inversion results become progressively more compatible with the modelled 4D response as the 3D PEM constraint penalty weight increases (map 2 & 3), however significantly less effectively when compared with the direct effect of implementing a 4D PEM constraint right away as described in the previous workflow (inversion of the differences). Increasing the number of realizations when inverting the baseline and the monitor vintages highly attenuates the random noise and effectively increases the 4D models PEM compliance (map 4).

The visual analysis of the mean of 20 realizations 4D PEM map depicts three main clusters of point, one located mostly on the top left (cluster 1), another located in the middle (cluster 2) and last located in far right (cluster 3).

Cluster 1 highlighted in Figure 4.20 corresponds to the geometrical distortion at the top and bottom of the seismic inversion grid due to the time-shift correction. This cluster has no geological meaning and should be considered an artifact. The set of points correspondents to cluster 2 (Figure 4.21) represent the regions with a positive change in P-wave velocity and a negative change in S-wave velocity, these locations correspond to layer where injected water is replacing oil in the reservoir. The cluster 3 emphasised in Figure 4.22 corresponds to regions with a negative change in P-wave and S-wave velocity which is not compliant with the modelled response.

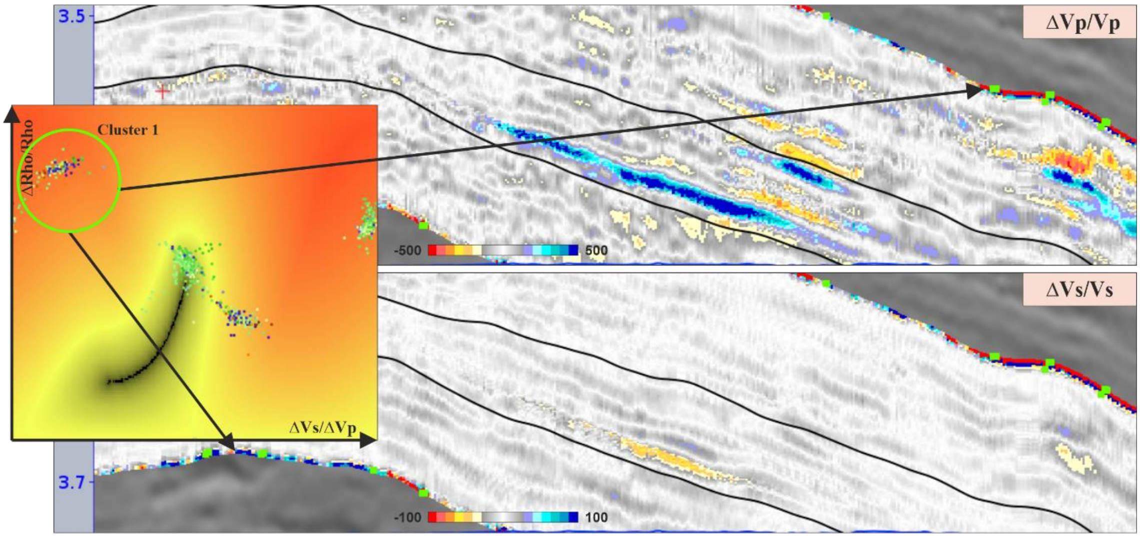

Figure 4.20 - 4D PEM constraint map highlighting the cluster of inverted points 1 and respective locations in the 4D elastic models. Representing the distortion at the top and base of the seismic inversion grid.

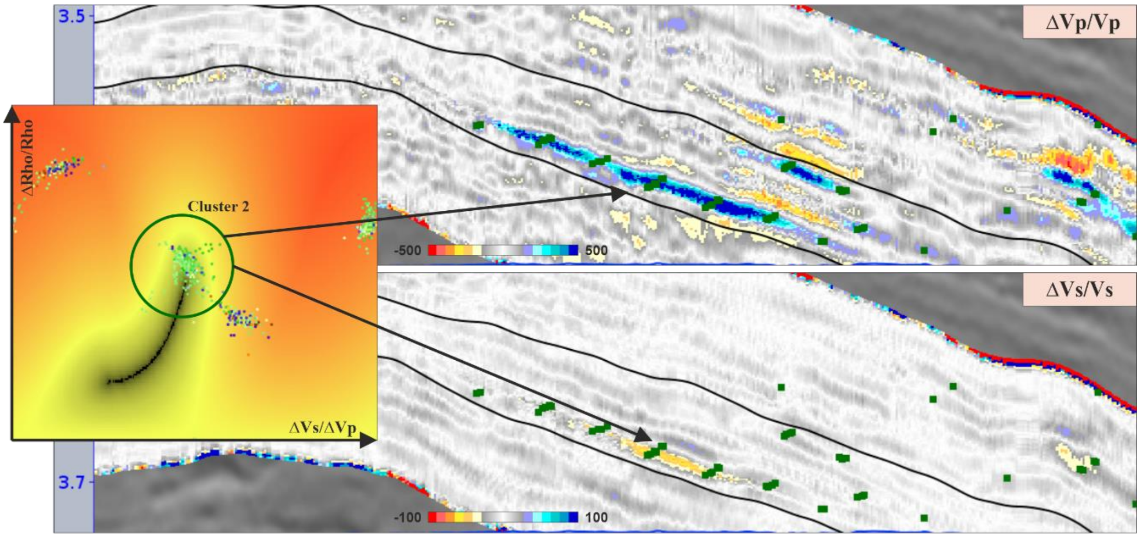

Figure 4.21 - 4D PEM constraint map highlighting the cluster of inverted points 2 and respective locations in the 4D elastic models. Representing the locations with a positive change in P-wave and a negative change in S-wave velocity.

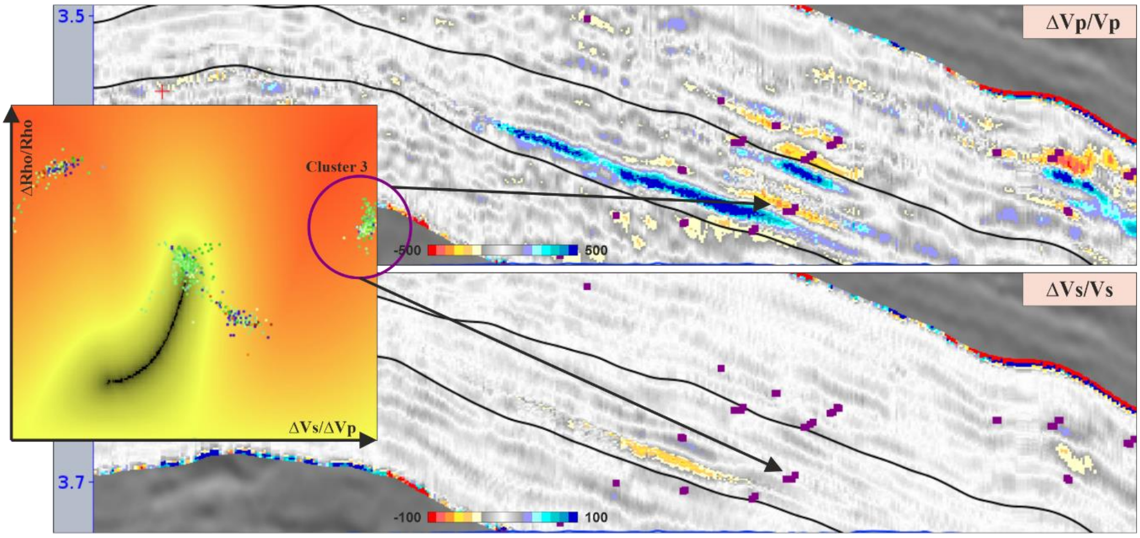

Figure 4.22 - 4D PEM constraint map highlighting the cluster of inverted points 3 and respective locations in the 4D elastic models. Representing the locations with a negative change in P-wave and S-wave velocity.

4.4. Workflow 3: Coupled Inversion

This workflow is similar to the previous one in the sense that each vintage is inverted separately, however the inversion of the baseline survey in this time-lapse inversion scheme is dependent on the elastic models obtained through the inversion of the monitoring survey, following a sequential approach, where the first stage comprises the inversion of the monitor survey to obtain the correspondent elastic models which are later used as the prior model for the baseline inversion. The key constraint in this 4D inversion technique is the constraint imposed in the baseline vintage inversion which prevents the inverted elastic properties from escaping from the prior model.

The initial step in the present workflow comprises the inversion of the monitor vintage and the time-shift correction using the time-shift model estimated from the full-stack seismic volume (Figure 4.23), capitalizing on the parameter management and optimization described previously, including 3D PEM constraint and estimating mean elastic models contemplating several realizations.

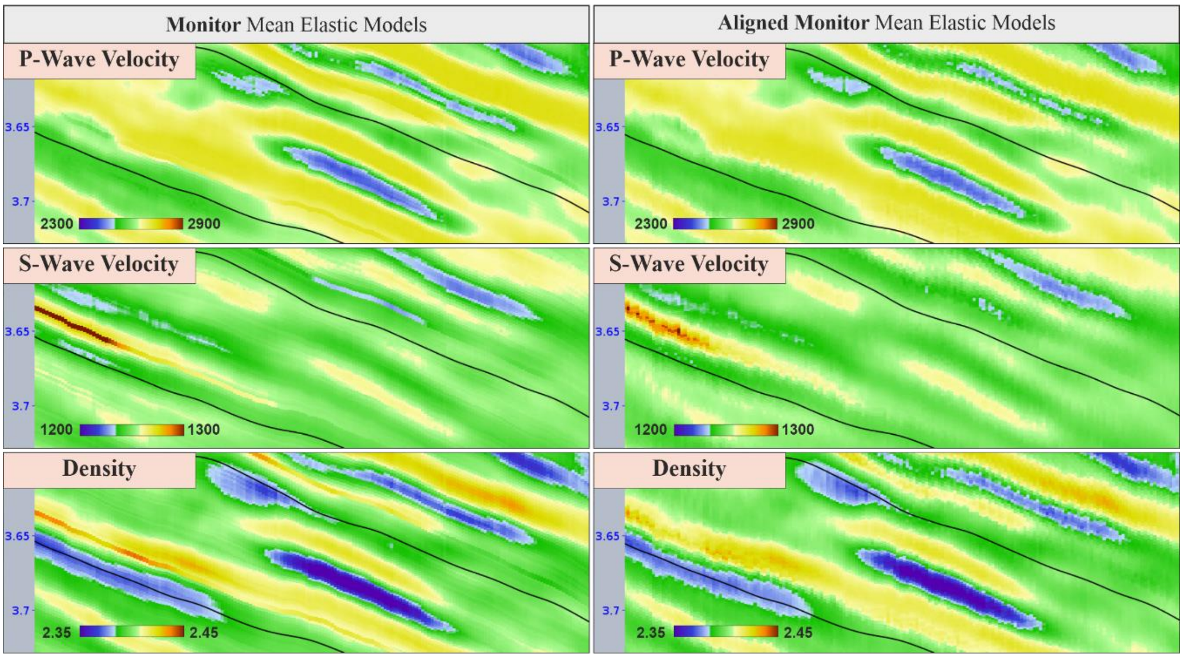

Figure 4.23 - Visual comparison between the baseline mean elastic models (left column) and the aligned monitor mean elastic models after applying a time-shift correction (right row). These aligned elastic models are going to serve as the prior model in the subsequent baseline inversion.

The following stage in this workflow corresponds to the inversion of the baseline vintage using the aligned elastic models obtained from the monitor vintage inversion as initial model (prior model). This is the step where the baseline inversion becomes dependent on the monitor inversion.

With the purpose of assessing the effect of imposing different drift constraints (that penalizes the inverted elastic parameters that are “far” from the a priori model), several baseline inversions were performed using various drift constraint and the results depicted in Figure 4.24 from which the following information were drawn: for a lower drift constraint (left column) the elastic models escape away significantly from the initial model, on the contrary, for high drift constraint (right column) the elastic models become broadly similar to the prior elastic model (monitor elastic models). Therefore, imposing a constraint penalty weight that preserves the original spatial features of the prior model and at the same time allowing for a realistic range of differences (center column).

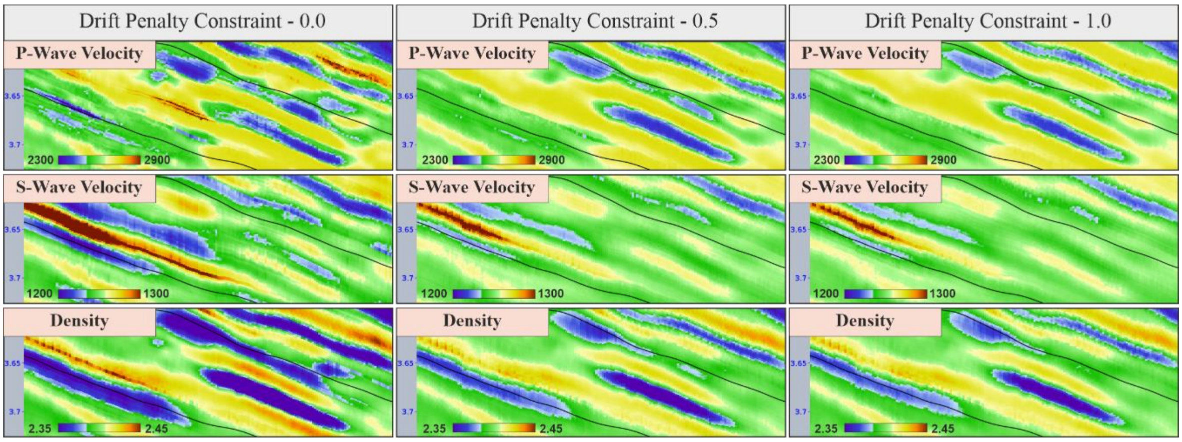

Figure 4.24 - Visual comparison between the effect of using different drift penalty constraint weights in the 3D stochastic inversion highlighting the impact on the estimated baseline elastic properties.

Furthermore, it is appropriate to note that choosing the correct drift penalty constraint also adds to the results compliance to the petroelastic model as portrayed in Figure 4.25, highlighting that the higher compatibility (translated by the overall lower cost) is achieved using a midway drift penalty constraint (middle map) while maintaining the 3D PEM constraint weight constant.

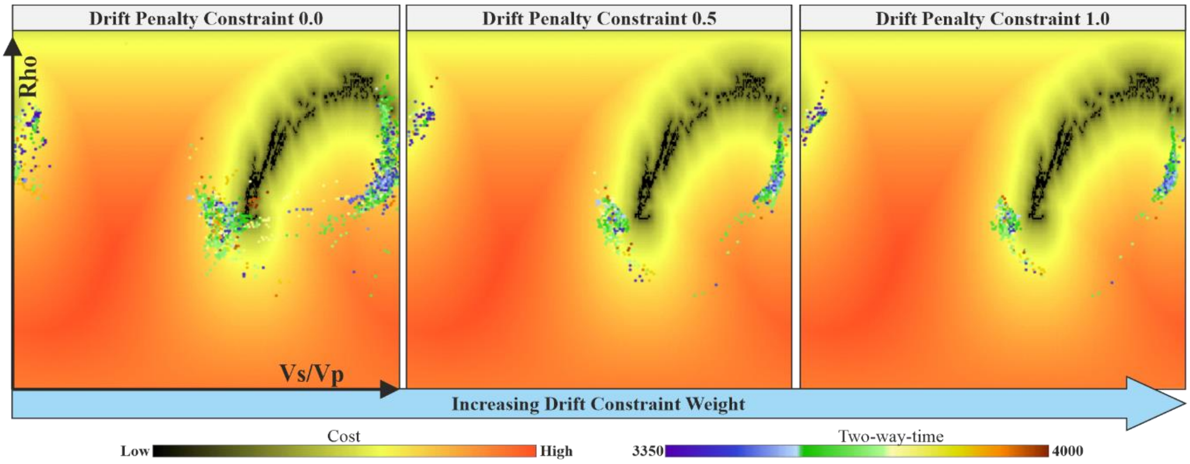

Figure 4.25 - 3D PEM constraint cost maps used in the monitor dataset (bottom row) inversion. Assessing workflow 3 baseline inverted elastic properties compatibility with the 3D petroelastic model by just modifying the drift penalty constraint weight.

The elastic models obtained in the baseline inversion using the optimal drift constraint are shown in Figure 4.26 alongside with the monitor vintage elastic models which serve as a term of comparison. These are optimized results that are obtained when the impacting parameters effects are properly analyzed and managed (compared to the elastic models obtained in the uncoupled inversion workflow), highlighting the improved spatial correlation between elastic properties, which will ultimately result in more consistent 4D elastic models.

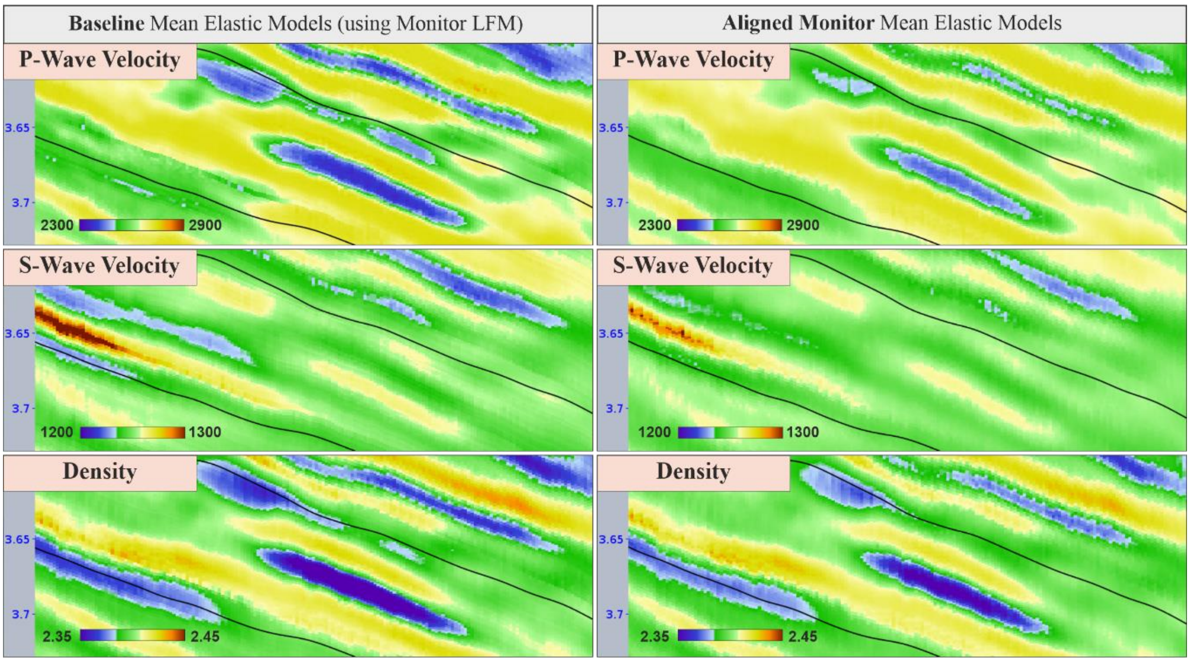

Figure 4.26 - Visual comparison between the baseline mean elastic models that are now dependent on the monitor inversion (left column) and the monitor mean elastic models (right row) both constrained to a 3D PEM.

Furthermore, when comparing the baseline elastic models (left column) with the equivalent monitor elastic models (right column) the most important changes are the significant increase in P-wave velocity and density but also a substantial decrease in S-wave velocity. These variations are consistent with the PEM and the expected phenomena according to the reservoir production context.

The ensemble of sections shown across Figure 4.27 intends again to demonstrate and evaluate the effect of imposing distinct drift penalty constraints but this time on the 4D models obtained through this workflow from which the following particularities were observed: for lower drift constraints (left column) the resulting time-lapse elastic models show inconstant spatial distributions and unrealistic 4D amplitudes. At the same time, for higher drift constraints (right column) the resulting time-lapse elastic models display poor and inconsistent 4D differences. Therefore, using an intermediate drift penalty constraint (center column) prevents the under and overestimation in the 4D elastic models.

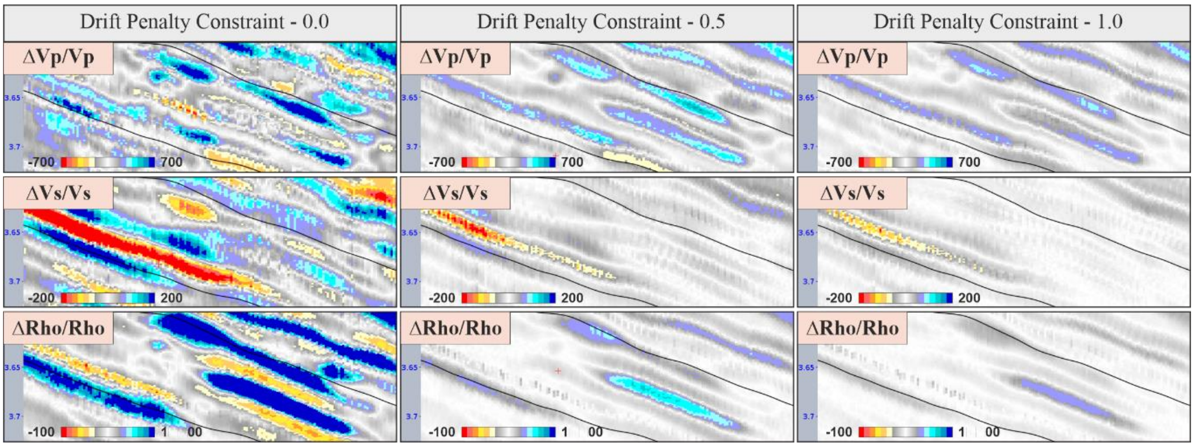

Figure 4.27 - Visual comparison between the effect of using different drift penalty constraint weights in the 4D stochastic inversion highlighting the impact on the estimated change in elastic properties.

The final results obtained by subtracting the baseline and the aligned monitor mean elastic models are shown in Figure 4.28 across an inline section which corresponds to water flooding from an injection well to a production well scenario. The time-lapse models obtained using this 4D inversion technique are smoother and show higher lateral continuity in comparison with the uncoupled inversion scheme. The present workflow can resolve three main 4D anomalies, relative to the relative change in P-wave velocity section (top section). Regarding the relation between elastic properties, there are overall fewer inconsistencies, emphasizing a high inverse correlation between P- and S-wave velocities with one of the anomalies and low inverse with the remaining two.

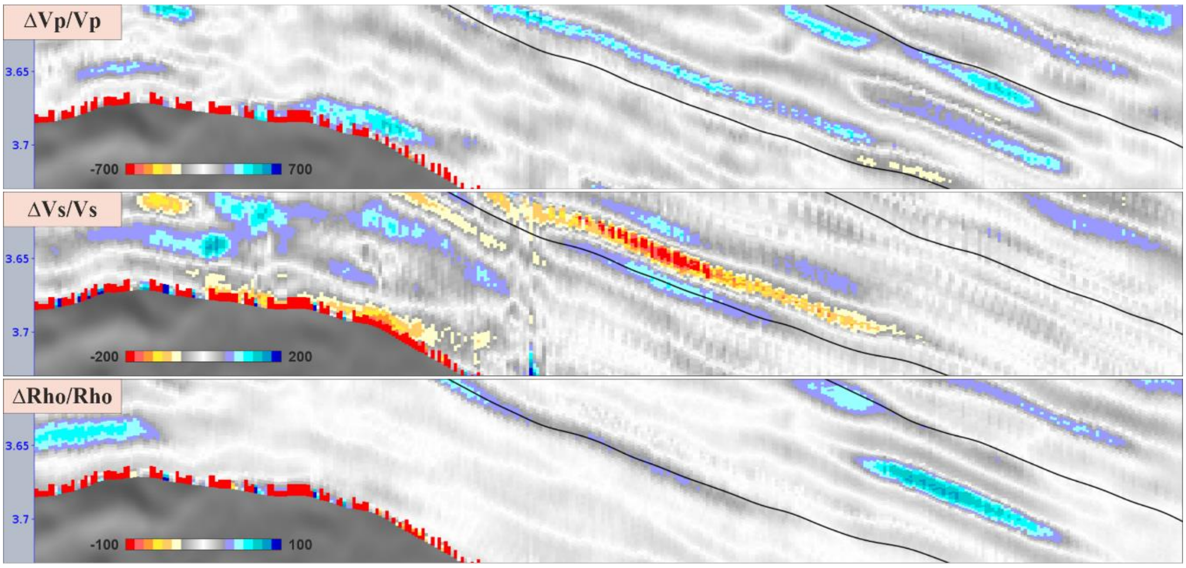

Figure 4.28 - Seismic sections showing the change in elastic properties following workflow 3. Change in P-wave velocity (top section), S-wave velocity (middle section) and density (bottom section).

There are still deformation artifacts at top and bottom of the inversion grid that are generated during the time-shift correction operation applied on the monitor elastic models. Nonetheless, these results are mostly in agreement with the expected elastic responses within the reservoir production scheme.

As in the previous workflow, even though this 4D inversion technique relies on 3D PEM constraints and not in a 4D PEM constraint the results obtained globally agree with the 4D PEM modelled response. Accordingly, in a way to verify how distinct drift penalty constraints improve the compliance of the time-lapse elastic properties with modelled 4D PEM response, the coupled inversion results can be plotted in a 4D PEM constraint map as depicted in Figure 4.29.

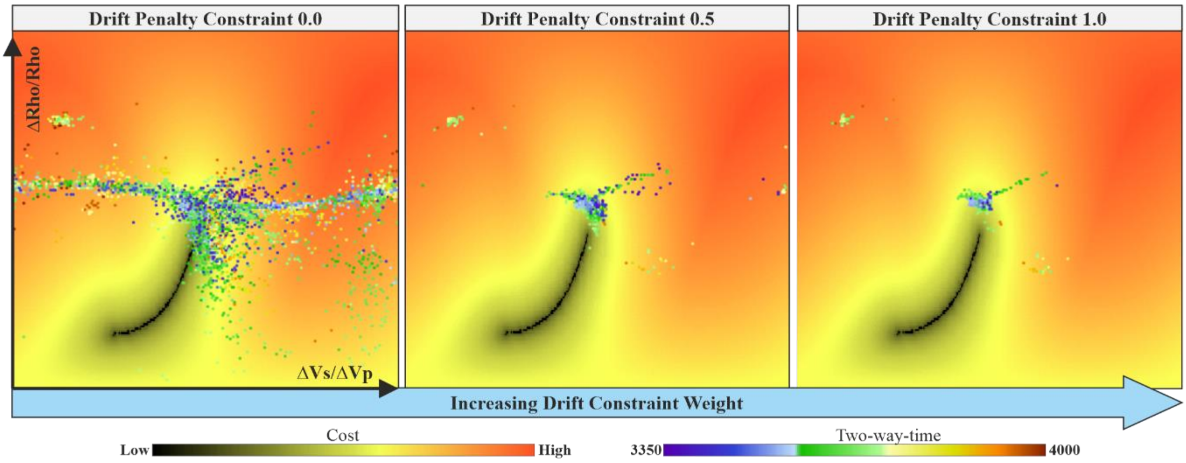

Figure 4.29 - 4D PEM constraint cost maps highlighting the workflow 2 results compatibility with the 4D modeled response. Assessing workflow 2 elastic properties compliance with the petroelastic model by just modifying the drift penalty constraint weight.

In the map view of the left one can observe that using a low drift penalty constraint weight for the baseline vintage inversion causes an overestimation of the 4D signal, which is translated by the large number of points plotted on the constraint map and their erratic distribution which shows that the time-lapse elastic properties do not comply with the modelled 4D PEM response. Oppositely if the drift penalty constraint is to high (right map) the differences between the inverted elastic models become reduced causing an underestimation of the 4D signal. Therefore, the usage of a midway drift penalty constraint weight provides a balance between both scenarios increasing the confidence on the resulting time-lapse elastic models. The constraint map view in the center exhibits the highest 4D PEM compliance (overall lower cost) that is obtained without modifying any PEM related constraints.

The visual analysis of the central 4D PEM map depicts one single main clusters of point mostly located in the middle (cluster 1), the remaining points that are plotted outside this location correspond to the distortion obtained in the top and bottom of the seismic inversion grid (Figure 4.30). The main cluster of points (Figure 4.31) corresponds to the regions with a positive change in P-wave velocity and a negative change in S-wave velocity this change in elastic properties can be directly correlated with the reservoir production mechanism in place.

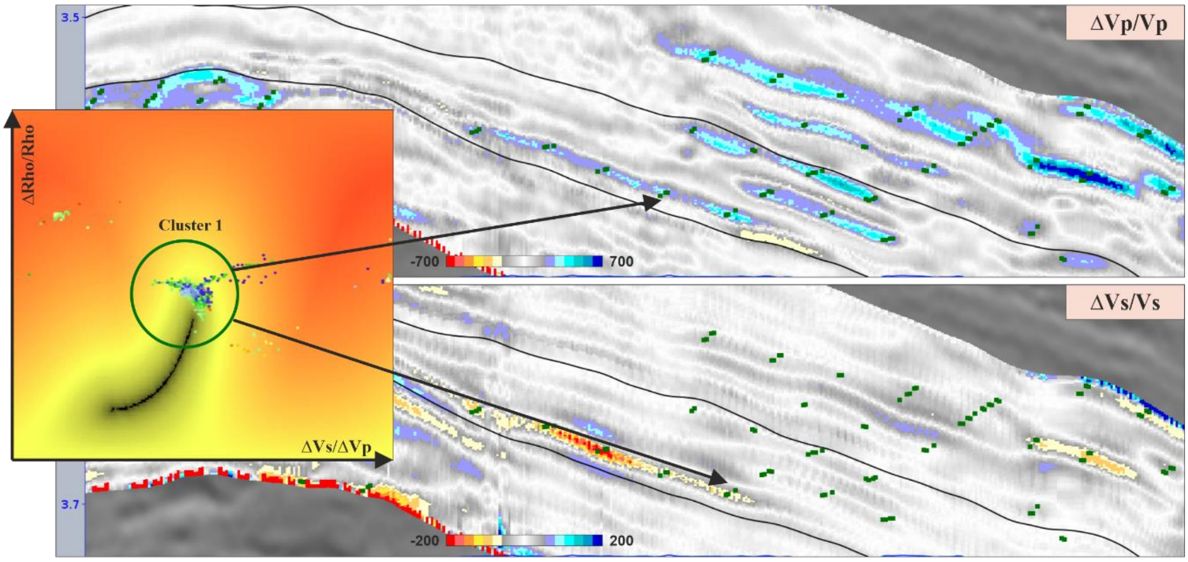

Figure 4.30 - 4D PEM constraint map highlighting the cluster of inverted points 1 and respective locations in the 4D elastic models. Representing the locations with a positive change in P-wave and a negative change in S-wave velocity.

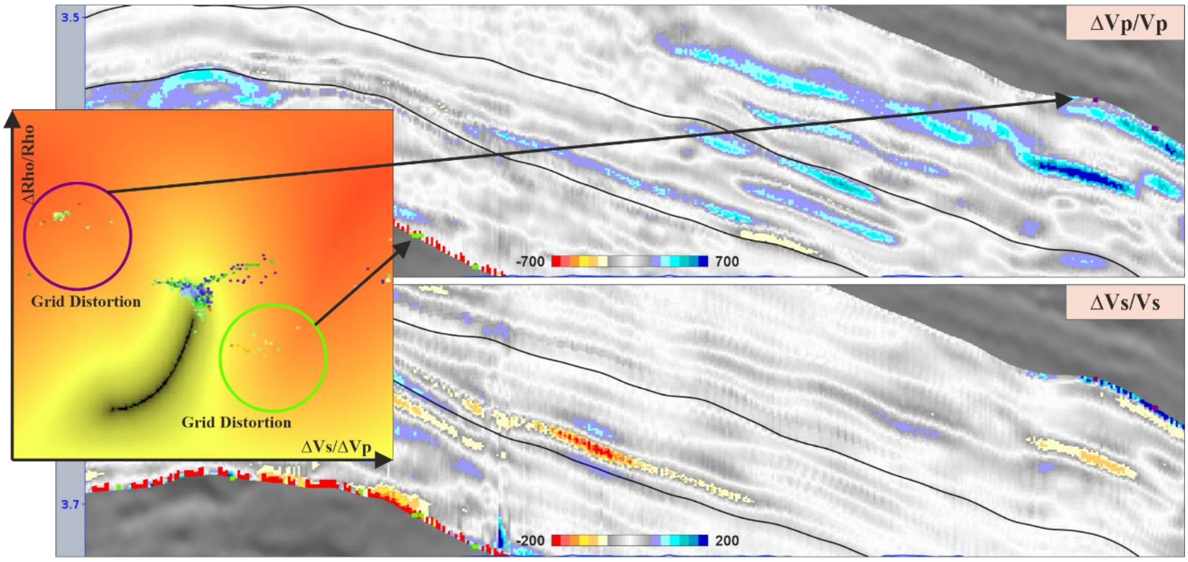

Figure 4.31 - 4D PEM constraint map highlighting the cluster of inverted points 2 and respective locations in the 4D elastic models. Representing the distortion at the top and base of the seismic inversion grid.

4.5. Comparison Between Workflows

So far, the different workflows have been presented and discussed individually. This section serves to provide a systematic and broader overview of the different 4D inversion techniques by comparing the elastic models obtained via different workflows in way to discern the similarities and dissimilarities between each of the different approaches.

As previously described several clusters of points can be discerned when each of the 4D inversion results are plotted in a 4D PEM map. Nonetheless, under the scope of this study the most important cluster is the one highlighted in the following ensembles of sections (Figure 4.32 to 4.34) with a dashed circle, this clusters of points represent inverted points with a positive change in P-wave velocity and a negative change in S-wave velocity that is coherent with the reservoir production mechanisms in place (water sweeping oil signature on elastic parameters).

Figure 4.34 display the same inline section drawn across the change in P-wave velocity models obtained from each time-lapse inversion technique (workflow 1, 2 & 3), accompanied by the correspondent 4D PEM constraint map projection (on the left). The green points plotted on each of the sections correspond to the inverted points underlined by the dashed circle, respectively, providing a direct visual correlation between the points in the map projection and the anomalies in the time-lapse elastic models.

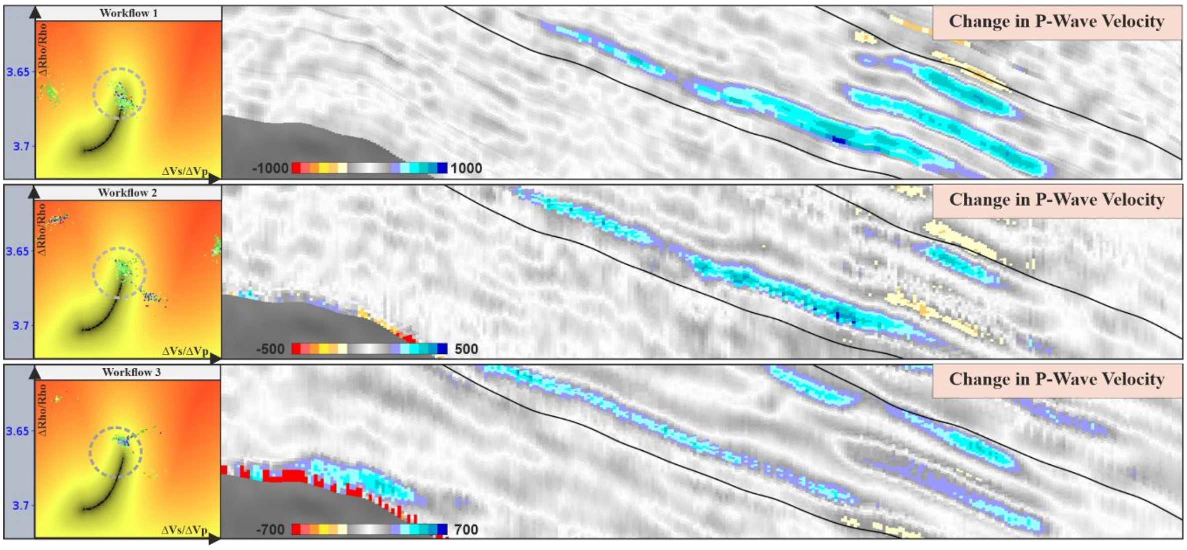

Figure 4.32 - Visual overview comparison for the relative change in P-wave velocity obtained through the different assessed workflows highlighting the respective similarities and dissimilarities.

The P-wave model obtained with workflow 1 (top sections) are very similar to the model obtained with workflow 3 (bottom section) although these workflows are inherently different. Regarding the number of anomalies, both workflows 1 and 3 can resolve three main anomalies with relatively similar shapes however workflow 2 (middle section) is only able to detect two of these anomalies. All workflows resolve negative changes in P-wave velocity which are not compliant with the imposed PEM and therefore should be independently interpreted, possibly representing artifacts.

One important characteristic that is emphasized here is that different 4D inversion techniques generally result in different amplitude scales in P-wave velocity, even though both 4D and 3D PEM constraint introduced only “force” the elastic parameters to be PEM compliant by providing amplitude ratios between parameters and not the absolute amplitudes. Therefore, these elastic amplitude differences should not be related with the implemented PEM constraints.

A feasible explanation for these amplitude differences can be derived for workflow 1 since it is based on the inversion of the seismic amplitude differences between vintages as opposed to workflow 2 and 3 which are based on the inversion of true seismic amplitudes of each vintage, which reasonably makes workflow 1 more sensitive to time-lapse changes in the reservoir, consistently capturing the production induced effects. However, the differences in the change in elastic amplitudes between workflow 2 and 3 cannot be justified in same way, and in this case, the differences are relatively smaller and very likely caused because for all the independent inversion, except for the baseline inversion in workflow 3, the initial models are set to a constant value (i.e., one assumes that the LFM is the same for the two surveys in those cases).

Figure 4.33 display the same inline section drawn across the change in S-wave velocity volume obtained from each 4D inversion technique (workflow 1, 2 & 3), accompanied by the correspondent 4D PEM constraint map projection (on the left).

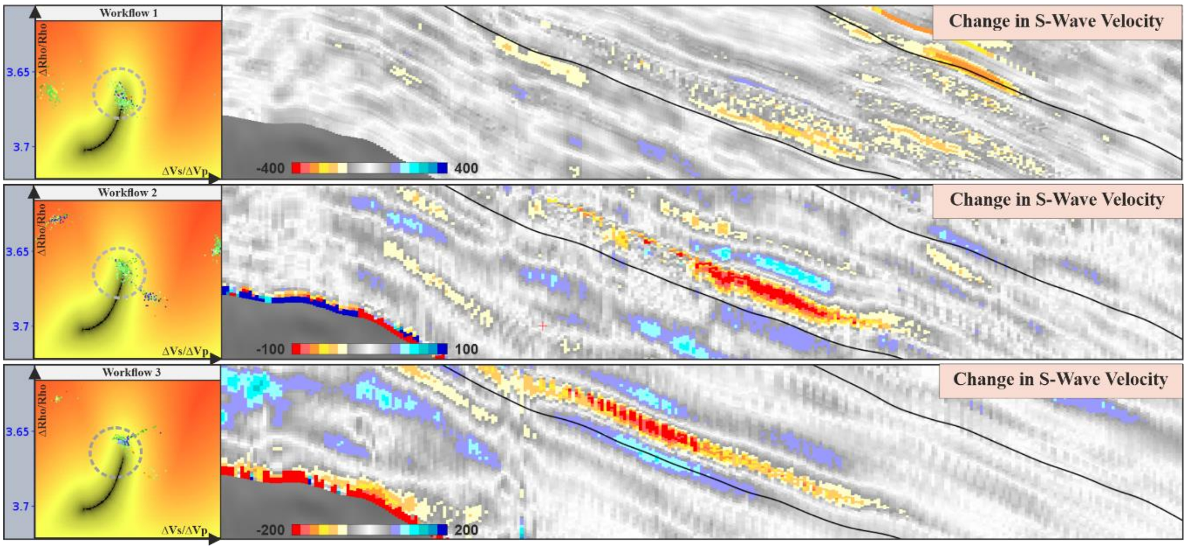

Figure 4.33 - Visual overview comparison for the relative change in S-wave velocity obtained through the different assessed workflows highlighting the respective similarities and dissimilarities.

Likewise, the S-wave model obtained with workflow 1 (top section) are very similar to the model obtained with workflow 3 (bottom section) although these workflows are inherently different. Workflow 1 and 3 can resolve three main negative S-wave velocity anomalies (underlined mostly by the green points locations) that are consistent with the change in P-wave velocity, meanwhile workflow 2 (middle section), although consistently, can only clearly resolve two of the main anomalies. Regarding the positive changes in S-wave velocity that are obtained through workflow 2 and 3, these are considered artifacts which are not consistent with the expected time-lapse response.

To conclude Figure 4.34 displays the change in density model obtained from each 4D inversion technique (workflow 1, 2 & 3), accompanied by the correspondent 4D PEM constraint map projection (on the left).

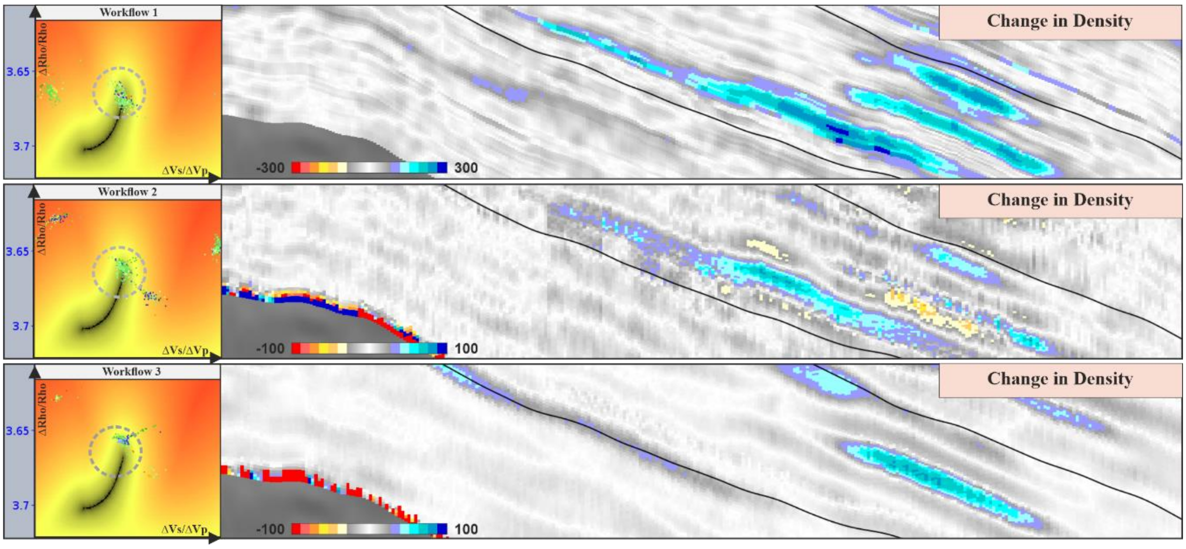

Figure 4.34 - Visual overview comparison for the relative change in density obtained through the different assessed workflows highlighting the respective similarities and dissimilarities.

From all the changes in elastic properties observed, the density is the elastic property that changes the less, therefore, the issues with the different amplitude scales for the 4D elastic properties described previously becomes unclear in these models. Furthermore, regarding this elastic property the models obtained with each workflow vary significantly (although workflow 1 and 3 continue to have similarities). Workflow 1 (top section) explicitly resolve three main positive anomalies. Workflow 2 (middle section) resolves two of the positive anomalies however also contemplates negative changes in density which do not follow the expected elastic response and should be considered artifacts without geological meaning. Whilst workflow 3 (bottom section) also resolve clearly two of the positive anomalies though this 4D inversion technique do not resolve the more continuous anomaly at the bottom of the reservoir that is highlighted by the green points without a positive change in density underneath.

Overall, the results obtained with workflow 1 are more systematically compliant with the modelled 4D response. Workflow 2 provides poor results with significant inconsistencies in the relationships between the change in elastic properties and creates anomalies inside the reservoir interval where no changes are expected. The comparison between the workflow 2 and 3 elastic models highlights that by coupling both inversions the spatial correlation between elastic properties improves, which ultimately results in more consistent 4D elastic models. Workflow 3 creates fewer inconsistencies (compared with workflow 2) and provides models that are comparable with the model obtained through workflow 1. Nonetheless, workflow 1 is easier to perform and requires less parameters compared with workflow 3.

5. Final Remarks and Future Work

Elastic 4D inversion is valuable because it provides new parameters (i.e., $\Delta\rho/\rho$ and $\Delta Vs/Vs$) compare to post-stack (acoustic) inversion which can be used to discriminate between different reservoir dynamic properties, such as fluid saturation and pressure, accordingly it is important that reliable 4D elastic models are provided for this process.

The present study has successfully generated a set of time-lapse elastic models compliant with prior geological information through the implementation of PEM constraints on different 4D elastic inversion workflows. Different workflows provide different results, through systematic assessment it is possible to identify the crucial point in which each workflow relies the most, in order to mitigate in a sense, the impact of inherent non-uniqueness in seismic inversion.

Workflow 1 requires consistent time-shifts between various angle stacks, which is not the case in this dataset where time-shifts estimated for each angle stack vary significantly, it is strongly dependent on the pre-progressing angle stack alignment (warping step) consistency since each angle stack is aligned individually. An effort should be made to improve as much as possible the data preparation.

Workflow 2 relies mostly on the consistency between both repeated datasets and time-shift alignment and generally result in misleading 4D elastic models. Workflow 3 in a way presents an improved version of the previous workflow, these improvements suggests that by introducing a way to couple both inversions augments the overall results coherency and reliability, reducing artifacts and improving interpretation quality, when properly parameterized and constrained.

The comparison between workflow demonstrates that for this study the most reliable 4D elastic models are obtained through workflow 1, even so workflow 3 performs well and the results shown are very encouraging. Consequently, the coupled inversion workflow is still under development and the integration in the future of a 4D PEM constraint linking both inversions will likely highly increase the trustworthiness of the resulting 4D elastic models.

This study was performed on a single dynamic mechanism (water sweeping), in the future it needs to be validated on a whole reservoir to assess how the constraints imposed behave when different mechanics are superimposed.

6. References

Almeida, A. S., & Journel, A. G. (1994). Joint simulation of multiple variables with a Markov-type coregionalization model. Mathematical Geology, 26(5), 565-588.

Alvarez, E., & MacBeth, C. (2013). An insightful parametrization for the flatlander's interpretation of time-lapsed seismic data. Geophysical Prospecting, 62(1), 75-96.

Avseth, P., Mukerji, T., & Mavko, G. (2010). Quantitative seismic interpretation: Applying rock physics tools to reduce interpretation risk. Cambridge university press.

Avseth, P., Mukerji, T., Mavko, G., & Dvorkin, J. (2010). Rock-physics diagnostics of depositional texture, diagenetic alterations, and reservoir heterogeneity in high-porosity siliciclastic sediments and rocks—A review of selected models and suggested workflows. Geophysics, 75(5), 75A31-75A47.

Azevedo, L., & Soares, A. (2017). Geostatistical methods for reservoir geophysics. Springer.

Azevedo, L., Nunes, R., Correia, P., Soares, A., Guerreiro, L., & Neto, G. S. (2014). Multidimensional scaling for the evaluation of a geostatistical seismic elastic inversion methodology. Geophysics, 79(1), M1-M10.

Bacon, M., Simm, R., & Redshaw, T. (2007). 3-D seismic interpretation. Cambridge University Press.

Barclay, F., Bruun, A., Rasmussen, K. B., Alfaro, J. C., Cooke, A., Cooke, D., ... & Ozdemir, H. (2008). Seismic inversion: Reading between the lines. Oilfield Review, 20(1), 42-63.

Batzle, M., & Wang, Z. (1992). Seismic properties of pore fluids. Geophysics, 57(11), 1396-1408.

Bernal, J. D., & Mason, J. (1960). Packing of spheres: co-ordination of randomly packed spheres. Nature, 188(4754), 910-911.

Bortoli, L. J., Alabert, F., Haas, A., & Journel, A. (1993). Constraining stochastic images to seismic data. In Geostatistics Tróia'92 (pp. 325-337). Springer, Dordrecht.

Bosch, M., Mukerji, T., & Gonzalez, E. F. (2010). Seismic inversion for reservoir properties combining statistical rock physics and geostatistics: A review. Geophysics, 75(5), 75A165-75A176.

Briceno Yanez, A. E. (2017). *Calibration and use of the petroelastic model for 4D seismic interpretation* (Doctoral dissertation, Heriot-Watt University).

Castagna, J. P., Batzle, M. L., & Eastwood, R. L. (1985). Relationships between compressional-wave and shear-wave velocities in clastic silicate rocks. geophysics, 50(4), 571-581.

Chu, D., Burger, J., & Medema, G. (2011). Using time strain volume for improved 4D interpretation: Methods and case studies. In SEG Technical Program Expanded Abstracts 2011 (pp. 4140-4143). Society of Exploration Geophysicists.

Domenico, S. (1974). Effect of water saturation on seismic reflectivity of sand reservoirs encased in shale. Geophysics, 39(6), 759-769.

Doyen, P. (2007). Seismic reservoir characterization: An earth modelling perspective (Vol. 2, p. 255). Houten: EAGE publications.

Dvorkin, J., & Nur, A. (1998). Acoustic signatures of patchy saturation. International Journal of Solids and Structures, 35(34-35), 4803-4810.

Filippova, K., Kozhenkov, A., & Alabushin, A. (2011). Seismic inversion techniques: choice and benefits. First Break, 29(5), 103-114.

Floricich, M., Jenkins, G., & McCormick, D. (2012, June). Probabilistic Inversion of Multiple 4D Seismic as Applied on Schiehallion Field. In 74th EAGE Conference and Exhibition incorporating EUROPEC 2012 (pp. cp-293). European Association of Geoscientists & Engineers.

Francis, A. M. (2006). Understanding stochastic inversion: Part 1. First Break, 24(11), 69-77.

Gardner, G. H. F., Gardner, L. W., & Gregory, A. R. (1974). Formation velocity and density—The diagnostic basics for stratigraphic traps. Geophysics, 39(6), 770-780.

Gassmann, F. (1951). Elasticity of porous media: Uber die elastizitat poroser medien: Vierteljahrsschrift der Naturforschenden Gesselschaft in Zurich.

Gavotti, P. E. (2014). Model-based inversion of broadband seismic data (Master's thesis, Graduate Studies).

Haas, A., & Dubrule, O. (1994). Geostatistical inversion-a sequential method of stochastic reservoir modelling constrained by seismic data. First break, 12(11), 561-569.

Hampson-Russell., 2009, Hampson-Russell Assistant. Hampson-Russell Software Documentation. Hampson-Russell Software, A CGGVERTIAS Company.

Hashin, Z., & Shtrikman, S. (1963). A variational approach to the theory of the elastic behaviour of multiphase materials. Journal of the Mechanics and Physics of Solids, 11(2), 127-140.

Hatchell, P. J., Kelly, S., Muerz, M., Jones, T. C., Engbers, P., Van Der Veeken, J., & Staples, R. (2002, May). Comparing time-lapse seismic and reservoir model predictions in producing oil and gas fields. In 64th EAGE Conference & Exhibition (pp. cp-5). European Association of Geoscientists & Engineers.

Hawkins, K., Howe, S., Hollingworth, S., Conroy, G., Ben-Brahim, L., Tindle, C., ... & Onaisi, A. (2007). Production-induced stresses from time-lapse time shifts: A geomechanics case study from Franklin and Elgin fields. The Leading Edge, 26(5), 655-662.

Hill, R. (1952). The elastic behaviour of a crystalline aggregate. Proceedings of the Physical Society. Section A, 65(5), 349.

Hodgson, N. (2009). Inversion for reservoir pressure change using overburden strain measurements determined from 4D seismic (Doctoral dissertation, Heriot-Watt University).

Johnston, D. H. (2013). Practical applications of time-lapse seismic data. Society of Exploration Geophysicists.

Kenter, C. J., Van den Beukel, A. C., Hatchell, A. C., Maron, P. J., Molenaar, K. P., Molenaar, M. M., & Stammeijer, J. G. F. (2004). Geomechanics and 4D: Evaluation of reservoir characteristics from timeshifts in the overburden. In Gulf Rocks 2004, the 6th North America Rock Mechanics Symposium (NARMS). American Rock Mechanics Association.

Kragh, E. D., & Christie, P. (2002). Seismic repeatability, normalized rms, and predictability. The Leading Edge, 21(7), 640-647.

Kuster, G. T., & Toksöz, M. N. (1974). Velocity and attenuation of seismic waves in two-phase media: Part I. Theoretical formulations. Geophysics, 39(5), 587-606.

Landrø, M. (2001). Discrimination between pressure and fluid saturation changes from time-lapse seismic data. Geophysics, 66(3), 836-844.

Landro, M., & Janssen, R. (2002). Estimating compaction and velocity changes from time-lapse near and far offset stacks. In 64th EAGE Conference & Exhibition (pp. cp-5). European Association of Geoscientists & Engineers.

Landrø, M., & Stammeijer, J. (2004). Quantitative estimation of compaction and velocity changes using 4D impedance and traveltime changes. Geophysics, 69(4), 949-957.

Leguijt, J. (2009). Seismically constrained probabilistic reservoir modeling. The Leading Edge, 28(12), 1478-1484.

Lindseth, R. O. (1979). Synthetic sonic logs—A process for stratigraphic interpretation. Geophysics, 44(1), 3-26.

Mavko, G., Mukerji, T., & Dvorkin, J. (2009). The rock physics handbook. Cambridge university press.

Mindlin, R. D. (1949). Compliance of elastic bodies in contact. J. Appl. Mech., ASME, 16, 259-268.

Nasser, M., Maguire, D., Hansen, H. J., & Schiott, C. (2016). Prestack 3D and 4D seismic inversion for reservoir static and dynamic properties. The Leading Edge, 35(5), 415-422.

Nur, A. M., Mavko, G., Dvorkin, J., & Gal, D. (1995). Critical porosity: The key to relating physical properties to porosity in rocks. In SEG Technical Program Expanded Abstracts 1995 (pp. 878-881). Society of Exploration Geophysicists.

Omofoma, V. E., & MacBeth, C. (2016). Quantification of reservoir pressure-sensitivity using multiple monitor 4D seismic data. In 78th EAGE Conference and Exhibition 2016 (Vol. 2016, No. 1, pp. 1-5). European Association of Geoscientists & Engineers.

Pannett, S., Slager, S., Stone, G., & Dekker, S. (2004). Constraining a complex gas-water dynamic model using 4D seismic. In SPE Annual Technical Conference and Exhibition. Society of Petroleum Engineers.

Raymer, L. L., Hunt, E. R., & Gardner, J. S. (1980,). An improved sonic transit time-to-porosity transform. In SPWLA 21st annual logging symposium. Society of Petrophysicists and Well-Log Analysts.

Reuss, A. (1929). Berechnung der fließgrenze von mischkristallen auf grund der plastizitätsbedingung für einkristalle. ZAMM-Journal of Applied Mathematics and Mechanics/Zeitschrift für Angewandte Mathematik und Mechanik, 9(1), 49-58.

Rickett, J., Duranti, L., Hudson, T., Regel, B., & Hodgson, N. (2007). 4D time strain and the seismic signature of geomechanical compaction at Genesis. The Leading Edge, 26(5), 644-647.

Røste, T., Dybvik, O. P., & Søreide, O. K. (2015). Overburden 4D time shifts induced by reservoir compaction at Snorre field. The Leading Edge, 34(11), 1366-1374.

Russell, B. H. (1988). Introduction to seismic inversion methods. Society of Exploration Geophysicists.

Sarkar, S., Gouveia, W. P., & Johnston, D. H. (2003). On the inversion of time-lapse seismic data. In SEG Technical Program Expanded Abstracts 2003 (pp. 1489-1492). Society of Exploration Geophysicists.

Simm, R., Bacon, M., & Bacon, M. (2014). Seismic Amplitude: An interpreter's handbook. Cambridge University Press.

Smith, W. O., Foote, P. D., & Busang, P. F. (1929). Packing of homogeneous spheres. Physical Review, 34(9), 1271.

Soares, A. (2001). Direct sequential simulation and cosimulation. Mathematical Geology, 33(8), 911-926.

Soares, A., Diet, J. D., & Guerreiro, L. (2007, September). Stochastic inversion with a global perturbation method. In EAGE Conference on Petroleum Geostatistics (pp. cp-32). European Association of Geoscientists & Engineers.

Tarantola, A. (2005). Inverse problem theory and methods for model parameter estimation (Vol. 89). siam.

Thore, P., & Blanchard, T. D. (2015). 4D propagated layer-based inversion. Geophysics, 80(1), R15-R29.

Tian, S. S. (2014). Closing the loop by engineering consistent 4D seismic to simulator inversion (Doctoral dissertation, Heriot-Watt University).

Vedanti, N., Pathak, A., Srivastava, R. P., & Dimri, V. P. (2009). Time lapse (4D) seismic: Some case studies. Earth Science India, 2.

Voigt, W. (1907). Bestimmung der Elastizitätskonstanten von Eisenglanz. Annalen der Physik, 327(1), 129-140.

Williamson, P. R., Cherrett, A. J., & Sexton, P. A. (2007). A new approach to warping for quantitative time–lapse characterisation. In 69th EAGE Conference and Exhibition incorporating SPE EUROPEC 2007 (pp. cp-27). European Association of Geoscientists & Engineers.

7. Annex

Introduction

During recent years, time-lapse studies have proven that seismic monitoring is a crucial reservoir management tool. The information obtained through time-lapse seismic data, when properly combined with geology, petrophysics, and engineering disciplines, have a paramount contribution to field development. Different production mechanisms induce different changes in elastic parameters and therefore there is a need to perform 4D elastic inversion which can discriminate between them and not to limit 4D inversions to providing a single parameter as it is classically done.

The present work intends to experiment different general workflows to conduct elastic 4D seismic inversion as well as introducing geological information as an elegant constraint in the inversion. The study assesses three different workflows: a classical inversion of the realigned differences (workflow 1), the independent elastic inversion and subsequent differentiation of baseline and monitor elastic parameters (workflow 2) and the inversion of the monitor dataset to provide the initial model for the inversion of the base, the resulting models are subtracted to obtain the respective 4D elastic models (workflow 3).

Background and preprocessing

The seismic data used for this study consists of four time-migrated angle stacks ([4°-12°], [12°-20°], [20°-28°] and [28°-37°]) and a set of fullstack volumes [0°-35°] acquired in 1998 (baseline survey), before starting production, and in 2015 (monitor survey), after 6 years of reservoir production. The wavelets used were obtained by subjecting each partial stack and the full-stack volumes to a multiwell-multi-angle based wavelets estimation workflow, from which a set of representative wavelets for each angle stack is obtained improving the convergence of all applied methods. As expected, with the 4D processing applied to base and monitor, vintage-to-vintage wavelets shape and amplitude content are very similar and the wavelets estimated for the baseline survey were used for each specific angle stack.

Due to reservoir production, changes in the subsurface elastic properties induce changes in two-way traveltime between repeated datasets which correspond to small time-shifts in the data. These time shifts cause the repeated seismic vintages to be time misaligned. In order to measure and correct these time shift, we use the warping method proposed by Williamson et al. (2007) that aims at estimating the time-strains between vintages and at aligning the monitor survey to the baseline reference survey by iteratively matching both the measured time-shifts and amplitude changes between the two datasets.

Pre-stack inversion workflows

Time-lapse inversion can be conducted in several different ways. In this paper we present three feasible 4D inversion workflows (figure 1) and their corresponding results (figures 2 to 4) obtained on a real seismic data example of a turbidites field.

1. Workflow 1 uses the 4D differences between surveys for each angle stack to invert for the relative change in elastic properties. It is strongly dependent on the pre-processing angle stack alignment consistency since each angle stack is aligned individually.
2. Workflow 2 encompasses the individual and independent inversion of base and monitor datasets to obtain the correspondent elastic properties models that are further subtracted to obtain the relative change in elastic properties, therefore considerably relying on the consistency of both inversion and monitor time-alignment.
3. Workflow 3 comprises initially the inversion of the monitor dataset to obtain the correspondent elastic properties volumes, which are later used as the prior model for the baseline dataset inversion. The elastic properties models are then subtracted to obtain the respective change in elastic properties. This workflow is similar to the previous one but it couples the inversion of the base to the inversion of the monitor.

The pre-stack inversion is taken a step further by including a petroelastic model (PEM) constraint that is derived from the available rock-physics models, static well-log data and production related information. Thore and Blanchard (2015) developed this constraint based on rock physics and reservoir production related information to guide the inversion results to more realistic combinations of elastic parameters, providing only the amplitude ratios between parameters and not the absolute amplitudes, highly improving the compatibility with the prior geological knowledge. The constraint corresponds to a 4D constraint (replacing oil by water) in workflow 1 and to a 3D constraint (some relationship between Vp, Vs and density) for workflows 2 and workflow 3.

For all the inversions, except for the baseline inversion in workflow 3, the initial models are set to a constant value (i.e. we assume that the LFM is the same for the two surveys). In the inversion of the differences workflow, the time-shift correction is made before the inversion and before dataset subtraction. In the workflows 2 & 3 the time alignment is applied on the inversion results of monitor and before subtraction of elastic parameters using the time-shift model computed on the full-stack.

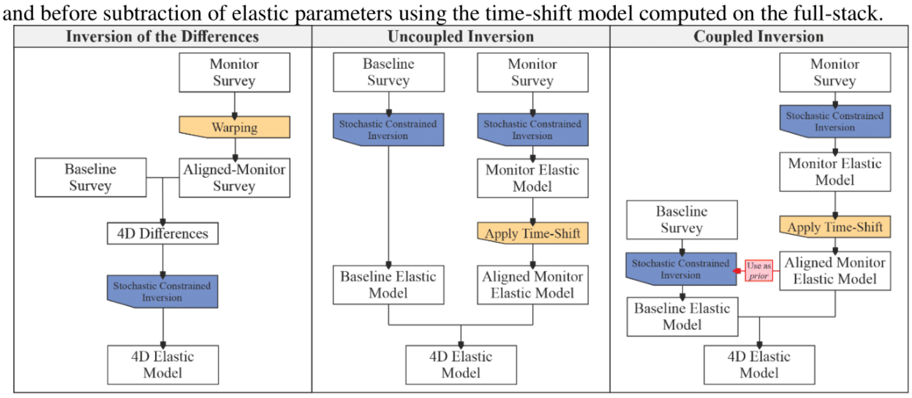

Figure 1 *Schematic representation of the three 4D inversion workflows assessed.*

Elastic inversion results

Workflow 1 – Inversion of the differences

The variation of elastic parameters is shown in figure 2 across an inline section which correspond to water flooding from an injection well to a production well. Corresponding to this dynamic mechanism, we expect to see a positive variation of Vp and density and a negative anomaly for Vs (due to the increase of density). Three 4D anomalies are been present and show a good coherent correlation between the estimated elastic parameters: the regions with positive changes in p-wave velocity match the regions with a negative change in s-wave velocity and the regions with positive change in density.

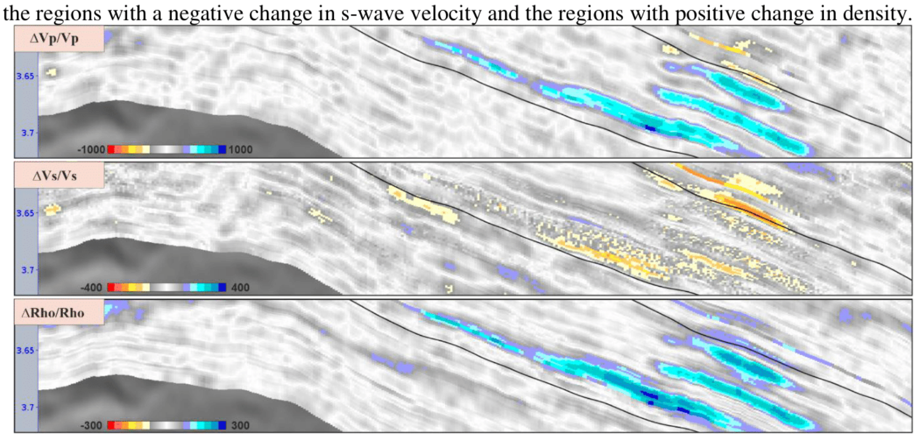

Figure 2 *Seismic sections showing the change in elastic properties following workflow 1. Change in P-wave velocity (top section), S-wave velocity (middle section) and density (bottom section).*

Workflow 2 – Uncoupled inversion

The first step on this workflow comprises the independent inversion of each seismic vintage, each inversion includes a 3D PEM constraint. Afterward, the elastic properties estimated from the inversion of the monitor survey are time-aligned to the baseline reference survey. After time-shifts correction we obtain the relative changes in elastic properties shown in figure 3 by subtracting the baseline and the monitor inverted elastic parameters.

The estimated time-lapse elastic properties obtained with this technique resolve fewer 4D anomalies relatively to the previous workflow. Furthermore, even though both the inversions are constrained to a PEM the elastic models present inconsistencies such as notorious positive change in s-wave velocity and negative changes in density that are not expected within this reservoir production context.

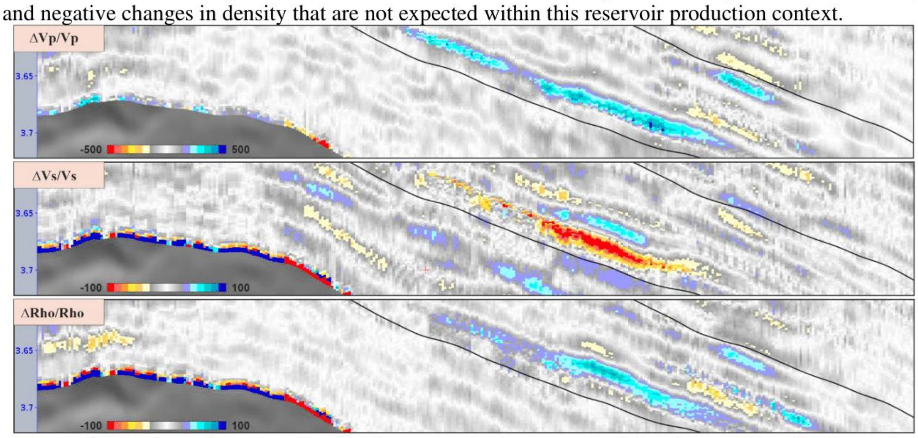

***Figure 3** Seismic sections showing the change in elastic properties following workflow 2. Change in P-wave velocity (top section), S-wave velocity (middle section) and density (bottom section).*

Workflow 3 – Coupled inversion

This workflow capitalizes on the workflow described previously to improve the overall result, following a sequential arrangement, where the baseline inversion becomes dependent on the monitor inversion. The key constraint in this inversion techniques is the constraint imposed in the baseline inversion which prevents the inverted elastic parameters from escaping from the initial model, being the model the results obtained from the monitor inversion, coupling both inversion. The changes in elastic properties (figure 4) are obtained by subtracting the baseline models from the aligned monitor elastic models.

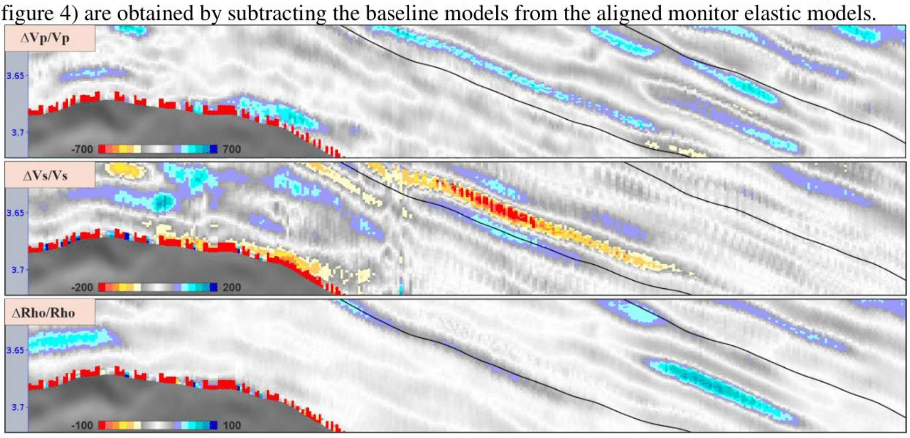

***Figure 4** Seismic sections showing the change in elastic properties following workflow 3. Change in P-wave velocity (top section), S-wave velocity (middle section) and density (bottom section).*

The results obtained using this technique are smoother and show higher consistent lateral continuity in comparison with the uncoupled inversion. This workflow can resolve three main 4D anomalies, particularly noticeable in the relative change in p-wave velocity sections. Regarding the relation between elastic properties, there are overall fewer inconsistencies, emphasizing a high inverse correlation between p- and s- wave velocities with one of the anomalies and low inverse correlation with the remaining two. This workflow is still under development and strong improvements are expected when all impacting parameters effects will be analysed and managed. In particular, we plan to introduce the 4D constraint in the base inversion to condition it to the monitor inversion result.

4D PEM Cost Maps

To evaluate the quality of the inversions concerning the petroelastic model imposed, each of the inversion results can be plotted in a 4D PEM map, as shown in figure 5. These maps represent the cost associated with the inversion results (the black dots corresponding to the predicted values by the PEM). The inverted elastic parameters for each workflow, transformed to the constrained space, are plotted as a set of scatter points and coloured with the two-way travel time.

Despite the fact that workflows 2 and 3 rely on 3D PEM constraints and not on the 4D PEM constraint their results globally agree with the 4D PEM modelled response. Visually we are able to discern several clusters of point, the most important one is the one highlighted with a dashed circles, this cluster represents inverted points with a positive change in p-wave and a negative change in s-wave that is coherent with the reservoir production mechanisms (water sweeping oil signature on elastic parameters). Workflow 1 exhibits a higher compatibility with the prior geological knowledge which is translated by an overall lower cost in comparison with the other workflows.

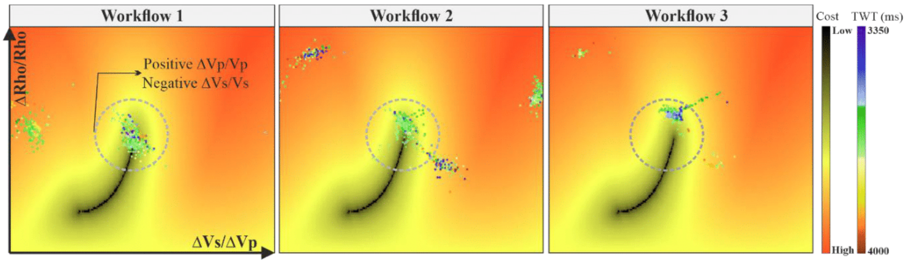

Figure 5 Modelled 4D petroelastic constraint emphasizing the different workflows time-lapse inversion results compatibility with the prior geological knowledge.

Conclusions

Elastic 4D inversion is valuable because it provides new parameters (i.e. ΔRho/Rho and ΔVs/Vs) compare to post-stack (acoustic) inversion which can be used to discriminate between different flow mechanisms. It is also much more difficult to perform and strongly depends on the quality of the pre-processing. In particular time shift consistency between various angle stack is a pre-requisite.

We have performed and analysed 3 different workflows in our case study. The last one still being under development. Workflow 1 requires a good aligned between near and far angle stacks, if this prerequisite is achieved the inversion provides good results. Workflow 3 shows enhancements when compared with the workflow 2, these improvements suggests that by introducing a way to couple both inversions augments the overall results coherency and reliability, reducing artifacts and improving interpretation quality, when properly parameterized and constrained. The variation amplitude of the several elastic parameters is different across workflows, this effect is an intrinsic property of each inversion technique, being workflows 1 more sensitive to smaller changes in the reservoir, resulting in a wider amplitude variation compared with workflows 2 and 3 that are significantly less sensitive to smaller changes.

References

Thore, P., & Blanchard, T. D. (2015). 4D propagated layer-based inversion. Geophysics, 80(1), R15-R29.

Williamson, P., A. Cherrett, and P. Sexton, (2007). A new approach to warping for quantitative time-lapse characterisation: 69th Annual International Conference and Exhibition, EAGE, Extended Abstracts, P064.